

A Novel Technique for Guiding Ablative Therapy of Cardiac Arrhythmias

by

Antonis A Armoundas

Bachelor of Science, Electrical Engineering
National Technical University of Athens, 1991

Master of Science, Biomedical Engineering
Boston University, 1994

Submitted to the
Nuclear Engineering

in partial fulfillment of the requirements for the degree of

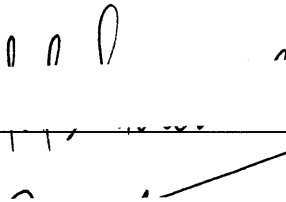
Doctor of Philosophy in Medical Imaging

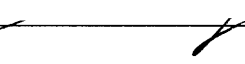
at the

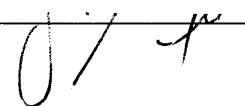
MASSACHUSETTS INSTITUTE OF TECHNOLOGY

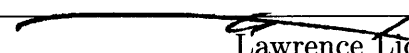
June 1999

© Massachusetts Institute of Technology 1999. All rights reserved.

Author:  _____
Nuclear Engineering
May 18, 1999

Certified by:  _____
Richard J. Cohen, M.D., Ph.D.
Whitaker Professor of Biomedical Engineering
Thesis Supervisor

Accepted by:  _____
Jacquelyn C Yanch, PhD
Associate Professor of Nuclear Engineering
and Whitaker College of Health Sciences and Technology
Reader

Accepted by:  _____
Lawrence Lidsky, PhD
Professor of Nuclear Engineering
Chairman, Department Committee on Graduate Students

science

A Novel Technique for Guiding Ablative Therapy of Cardiac Arrhythmias

by

Antonis A Armoundas

Submitted to the Nuclear Engineering
on May 18, 1999, in partial fulfillment of the
requirements for the degree of
Doctor of Philosophy in Medical Imaging

Abstract

Catheter ablation, a technique to prevent cardiac arrhythmias from recurring involves the use of a catheter to deliver radio-frequency energy to the site of origin of these arrhythmias. The guidance of the ablation catheter to the site of origin of these arrhythmias is mainly based on the experience of the cardiac electrophysiologist and as a result the procedure may require many hours during much of which the arrhythmia is ongoing. Thus, patients that cannot tolerate this procedure are necessarily excluded. We have explored the development and evaluation of a new methodology that would allow the use of body surface electrocardiographic (ECG) signals to both identify the site of origin of the arrhythmia in the heart, and guide the ablation catheter to the same site.

The three-dimensional distribution of electrical sources in the heart in general cannot be determined from analysis of the potentials recorded on the body surface. However, when the electrical activity is localized (i.e. before the depolarization wave-front spreads from the site of the origin of an arrhythmia) it can be represented with a single equivalent moving dipole (SEMD) whose location and moments can be estimated. We developed an inverse algorithm to estimate the SEMD parameters from body surface ECG signals. If one delivers bipolar current pulses to the tip of the ablation catheter while recording the resulting body surface signals, and uses the same inverse algorithm one would also be able to localize the tip of the catheter. Using this information one could guide the tip of the catheter to the site of origin of the arrhythmia.

We have shown that for realistic measurement noise magnitudes, we can identify cardiac electrical sources with the resolution required (millimeter) for clinical applications such as radio-frequency catheter ablation procedures.

Thesis Supervisor: Richard J. Cohen, M.D., Ph.D.

Title: Whitaker Professor of Biomedical Engineering

To *αριστείδης* that insisted *to keep myself always alert*

To *ευτυχία* that insisted *never to give – up*

To *φάνια* for her *spiritual and mental nourishment* for ten years

Acknowledgments

This thesis has been the result of the compilation of dreams and efforts of many people for many years. People that inspired in me the desire to explore the new and the unknown, people that believed and encouraged my “ideas” and efforts, people that guided me in every step I made, and finally, but not lastly, people that may have patiently endured my choices and decisions. To all my family and friends and colleagues I OWE a big-big THANK YOU.

Early on in my life I realized that people grow through their efforts to define their life, through the opportunities they are given and finally through their ability to comprehend the world they live in. I would like to thank my advisor Professor Richard J Cohen for the opportunity he gave me for eight years to work in his lab, and educate myself about life and science.

I would also like to thank Professor Jacquelyn Yanch for her significant and very much appreciated guidance, support and encouragement throughout my tenure at MIT.

Also, I would like to thank Professor Bruce Rosen and Professor Anders Dale for their committment to providing very positive and insightful contribution in this Thesis.

Thank you very much Professor Cory for being part of my PhD Thesis Defense Committee and making the Thesis Defense a stimulating and challenging experience for me.

Andy Feldman, PhD. - Andy has been *my hero* for the last two years and his mentorship shaped and defined the mental challenges of this research project. He devoted his heart and his mind to my efforts and demonstrated how discipline and focus lead to success. Thank you from my heart Andy, I am grateful.

Derin Sherman, PhD. - Derin has been a tremendous source of knowledge easily and happily available to those that would like to share it. Thanks a lot Derin for generously providing your time and help for the last eight years.

Rama Mukkamala, MS. - Rama became a fan of the scientific challenges of my thesis and enjoyed providing valuable consultation from his expertise. I enjoyed the stimulating, even high-temper discussions with him that would start from arguing on NBA matters (and “secondary” college basket-ball) and end in intriguing estimation theory problems. Thank you for being there Rama.

Yuri Chernyak, PhD.- Yuri’s mentorship and guidance through equations was

challenging and demanding. His highly intense and vigorous scientific approaches were a valuable experience to me. Thank you Yuri.

Tom Mullen, PhD. - Tom sets an unmatched example of unselfish interest and contribution to everyone's problems and difficulties. He has been of great help and inspiration for everyone. I am grateful, Tom.

Ki Chon, PhD - Ki's presence in the lab was very stimulating and his contribution to my scientific education was equally significant. I have been graciously receiving his mentorship and advising until today. Thank you Ki.

Hans Esperer, MD. - Hans has been a stimulating and fresh blow of wind in our lab. I enjoyed talking with him about politics, theology and culture.

Bin He, PhD. - Bin has patiently and methodically introduced me to the concepts of body surface potential mapping. I learned a lot of experimental skills from him and became friendly and intrigued by the idea of pursuing a PhD in his field of expertise. His modesty and humility made it great pleasure working with him. Thank you Bin.

Nenad Bursac. - Nenad's scientific discussions have been intriguing and stimulating.

Nikhil Iyengar, MS. - It has been great pleasure working close to Nik for about a year and be part of his efforts in pursuing his MS research project.

Paul Belk, PhD. - Paul has been one of the instrumental minds of the animal experiments. He provided his time and thoughtful intellect in making them successful.

Ray Lee, MS. - Thank you Ray for helping me to put together the data base obtained from many and lengthy experiments.

Dean William Taft, PhD. - Dean Taft's continuous support throughout my graduate school (even when he was retired) has been a steady stream of encouragement to me. Thank you.

I would also like to thank the other members of the laboratory, Nikolai Aljuri, Nastos Dousis, Thomas Ferl, Matthew Hollingworth, Ming Maa, Toshihiko Nanke, Craig Ramsdell, Shinji Shatoh, Karin Toska for creating a nice and friendly environment in the lab.

Serene Yeam. - Serene provided generously and happily her assistance every time there was a need. Thanks a lot Serene.

Finally, I would like to express my appreciation to the agencies that provided financial support for this thesis research. This study was partially funded by NASA Grant NAGW-4989 and NIH HL-09570. I am also grateful to the George Vostanis

Foundation and the Hellenic Medical Society of New York for their Fellowship support they provided.

Contents

1	Introduction	21
1.1	Thesis Objectives	21
1.2	Thesis Description	22
2	Background and Significance	29
2.1	The Problem	29
2.2	Technical Considerations on Catheter Ablation	31
2.3	Clinical Considerations of Catheter Ablation	32
2.4	Mapping Techniques and Successful Ablation	34
2.4.1	Fluoroscopic Guidance	35
2.4.2	Electro-anatomical Mapping	35
2.4.3	Basket Catheter	36
2.5	Classic Electrocardiography	36
2.6	Body Surface Potential Mapping	37
2.7	Inverse Solutions in Terms of Epicardial Potentials	38
2.8	On the Equivalent Dipole Model	39
2.9	Utility of the Equivalent Cardiac Generator	42
2.10	Could the Single Equivalent Moving Dipole Model Serve as a Tool in Guiding the Ablation Catheter to the Ablation Site?	43

3	Development of Optimization Methods and Results	47
3.1	Motivation	47
3.2	The optimization methods	48
3.3	Conjugate Gradient Method	49
3.4	Variable Metric Method	54
3.5	Simplex Method	56
3.6	Techniques for Evaluation of Optimization Methods	59
3.6.1	The Models	59
3.6.2	The Objective Function	60
3.6.3	Calculation of the Derivatives of the Objective Function with Regard to the Dipole Parameters	61
3.6.4	The 3 plus 3 Parameter Optimization Method	62
3.7	An Optimization Algorithm for the Estimation of the Single Equivalent Moving Dipole Parameters	63
3.8	Numerical Studies and Results	65
3.8.1	Application of the Inverse Algorithm in Evaluating the Spatial Uncertainty of the Dipole Identification Using All Optimization Methods	65
3.8.2	Selection of the Objective Function	68
3.8.3	Effect of the Measurement Noise on the Uncertainty of the Spa- tial Dipole Parameter Estimation	71
3.8.4	Effect of Dipole Orientation on the Uncertainty of the Spatial Dipole Parameter Estimation	72
3.9	Parameter Confidence Interval Estimation from the Prediction Error Theory	74
3.10	An Estimate of the Dipole Spatial Uncertainty Using Characteristics of the χ^2/dof	77

3.11	The Accuracy of the Optimization Algorithm in Computer Simulations	79
3.12	Discussion	80
4	Computer Simulations on A Distributed Source Model	85
4.1	Motivation	85
4.2	Model description	86
4.3	Results	87
4.4	Discussion and Conclusions	93
5	Evaluation of the Algorithm to Identify the SEMD in Real ECG Signals	97
5.1	Motivation	97
5.2	Experimental Protocol	98
5.3	Data Acquisition and Processing	99
5.4	The ECG Analysis Process	101
5.5	On the Resolution of the Inverse Algorithm	103
5.6	Temporal Evolution of the SEMD Parameter Estimates During the Cardiac Cycle	104
5.7	Prediction of the ECG Signals From the SEMD Parameter Estimates	105
5.8	Early Activation Analysis in the ECG Signal	106
5.9	Estimation of the SEMD Spatial Uncertainty Using Characteristics of the χ^2/dof	106
5.10	Measurement Noise Dependent Statistical Properties of the SEMD Parameter Estimates	107
5.11	Beat-to-beat Variation of the SEMD Parameter Estimates	110
5.12	Resolvability of two Epicardial Pacing Sites	111
5.13	Ventricular Activation-Recovery	113
5.14	Pacing Spike Identification	114

5.15	The Effects of Thoracotomy	116
5.16	On the Unipolar Electrocardiogram	116
5.17	On the Single Equivalent Moving Dipole Assumption	118
5.18	On the Significance of the RNMSE in ECG Signals in the Limit of Small Measurement Noise	121
5.19	Discussion	123
6	Summary of Results and Conclusions	145
6.1	Goals Achieved With this Thesis	145
6.2	Detailed Summary of Results	145
6.3	Final Conclusions on the Accuracy of the SEMD Optimization Algorithm	149
7	Impact and Future Direction	153
7.1	Significance and Relevance of the Research	153
7.2	Advantages and Disadvantages of our System Compared with Com- mercial Systems	154
7.2.1	Impact on Quality of Life and the Economics	155
7.2.2	Impact on the Use of the Cardioverter-defibrillator and Anti- arrhythmic Drugs	156
7.2.3	Impact on the Treatment of Multiple VT Morphologies	156
7.2.4	Impact on Reducing Exposure to Radiation	157
7.3	Other Arrhythmias That Can be Treated With Radio-frequency Ablation	157
7.3.1	Paroxysmal Supraventricular Tachycardia	157
7.3.2	The Wolff-Parkinson-White Syndrome	158
7.3.3	Atrial Flutter	158
7.3.4	Atrial Fibrillation	159
7.3.5	Idiopathic Ventricular Tachycardia	159
7.4	Proposed Studies	160

7.4.1	Saline Tank Studies	160
7.4.2	Realistic Anatomic Geomertry Computer Simulations	160
7.4.3	Clinical Studies	161
7.4.4	Guiding the Catheter to the Ablation Site	162
7.4.5	Spatial Information About the Heart and the Electrodes	165
7.4.6	Impact on Differentiating Between Focal Versus Reentrant Ar- rhythmias	166
7.4.7	Ethical Aspects of the Proposed Research	166
7.4.8	Experimental Problems of Clinical Study	167
7.4.9	Problems in Defining an Absolute Reference Point for Activa- tion Data Recorded During Ventricular Tachycardia	167
7.4.10	Other Study Issues	168

A Special Case	171
-----------------------	------------

List of Figures

2-1	The catheter ablation set-up	31
2-2	Potential field of a single cell in an infinite volume conductor [62]. . .	40
2-3	Solid angle geometry	41
2-4	Dipole moment of a piece of partially depolarized tissue.	42
2-5	Evolution of the activation wavefront around scar tissue. Configuration of three different reentrant circuits are shown. In each panel the gray regions are regions of conduction block, which could be due to fibrous scar or collision of excitation fronts. Black arrows indicate the circulating wavefronts. Smaller gray arrows indicate wavefronts propagating in “bystander” regions of the scar that are not in the reentry circuit. A. The circulating reentry wavefront propagates along the border of the infarct region. B. The reentry circuit is contained in the infarct region. C. Portion of the reentry circuit is contained within the infarct region, but following exit from the infarct region, two wavefronts travel along the border of the infarct to reach the proximal “entrance” to the reentry circuit path through the infarct, forming a double loop reentry circuit [79]	45
3-1	The potential field in an infinite homogeneous medium; \mathbf{r} is the vector from the origin to the field point and \mathbf{r}' is the vector from origin to the point dipole.	59

3-2	The algorithm used in the dipole parameter estimation.	64
3-3	Effect of the measurement noise estimate on the dipole spatial parameter estimation. The median distance (“<” indicates the unbounded and “>” indicates the bounded case) and standard deviation between the true and the estimated location of a dipole are shown. The convergence rate for each of the two cases (unbounded and bounded) is also shown.	72
3-4	Effect of the dipole orientation (for random solid angle Ω) on the uncertainty of the dipole spatial parameter estimation. The median distance (“<” indicates the unbounded and “>” indicates the bounded case) and standard deviation between the true and the estimated location of a dipole are shown. The convergence rate for each of the two cases (unbounded and bounded) is also shown.	73
3-5	Distribution of χ^2/dof values along each of the major orthogonal axes (i.e $-x \rightarrow +x$) and around the optimal solution.	78
4-1	Representation of the distributed source model.	87
4-2	The error and Root Mean Normalized Square Error (RNMSE) as a function of z_{belt}/r_{sph}	89
4-3	The Root Mean Normalized Square Error (RNMSE), Error, χ^2/dof , $\delta P/P_{eq}$, δr as a function of the angle that the wavefront forms with the z-axis.	90
4-4	The $\delta r/r_{sph}$ is plotted as a function of z/r_{sph} for different r_{belt}/r_{sph} and for electrodes placed all over the sphere (upper panel) and the upper hemisphere (lower panel).	92
5-1	Diagram of electrode position on the sock.	99
5-2	Configuration of the body surface electrodes [33].	100

5-3	A typical representation of the median beat of 60 channel ECG recording.	127
5-4	The process of data collection and analysis.	128
5-5	ECG beat alignment according to the peak of the QRS	129
5-6	The algorithm used in the identification of the equivalent cardiac generator.	130
5-7	The principles of activation mapping for a theoretical reentry circuit [79].	131
5-8	Dipole moment of a piece of partially depolarized tissue.	132
5-9	Variation of the single equivalent moving dipole parameter estimates across the cardiac cycle (shown in the lower panel).	133
5-10	Measured (in red), predicted (in blue) ECG signals (median beat) and predicted from continuous data (in green) from nine body surface sites. The correlation coefficient (r) between the measured and predicted signals for each channel is also shown.	134
5-11	Distribution of χ^2/dof values along each of the major orthogonal axes (i.e $-x \rightarrow +x$) and around the optimal solution.	135
5-12	The measurement-noise dependent statistical nature of the SEMD parameter estimates.	136
5-13	Confidence interval of the spatial SEMD parameter estimates obtained from different noise realizations and the prediction error theory. . . .	137
5-14	Confidence interval of the spatial SEMD parameter estimates obtained from different noise realizations and spatial variation in χ^2	138
5-15	The beat-to-beat statistical nature of the single equivalent moving dipole parameter estimates.	139
5-16	Resolution of two epicardial pacing sites based on beat-to-beat analysis.	140
5-17	Resolution of two epicardial pacing sites based on median beat analysis and different noise realizations.	141

5-18 Potentials and currents associated with epicardial pacing ([58]); the diagram illustrates potential and current patterns associated with a single with a single pacing spike (★). The region of negativity is elliptical, with the major axis oriented along the fibers.	142
--	-----

List of Tables

3.1	Comparison of the <i>median</i> \pm <i>uncertainty</i> of the true minus the estimated solution using the 3 <i>plus</i> 3 parameter and the 6 <i>parameter</i> approaches, for each of the Davison-Fletcher-Powell (DFP), Fletcher-Reeves-Polak-Ribiere (FRPR) and Simplex methods for different noise realizations, σ_n (in parenthesis is the percent of runs which yielded convergent results). NC: Non-convergent	67
3.2	Comparison of the objective function criteria using the inverse algorithm in identifying the spatial dipole parameters.	69
3.3	The dipole spatial uncertainty for measurement noise magnitude of $\sigma_n = 0.01$ <i>mV</i> in a computer simulation unbounded model (upper table) and in a bounded spherical model (lower table).	80
3.4	The uncertainty due to noise realizations (upper table) and random dipole orientation as well as noise realizations (lower table).	82
5.1	The spatial uncertainty at the point of earliest activation.	125
6.1	Uncertainty in the spatial SEMD parameter estimates.	151

Chapter 1

Introduction

1.1 Thesis Objectives

Cardiac death constitutes the number one cause of death in the western industrialized world. About half of these deaths are believed to be due to arrhythmias such as ventricular tachycardia and ventricular fibrillation. A technique namely, *catheter ablation* which involves the delivery of radio-frequency energy from the tip of a catheter to the site of origin of these arrhythmias in the heart, is a very promising approach to the prevention of these arrhythmias.

In order for catheter ablation to be successful, the site of origin of the arrhythmia has to be accurately identified and the catheter through which radio-frequency energy is delivered brought to the same site. Currently this is done through a painstaking procedure that is based on a “trial and error” approach, the success of which greatly depends on the experience and the skill of the cardiac electrophysiologist in charge of the procedure.

This thesis explores the development and evaluation of a new methodology that would allow the cardiac electrophysiologist to use body surface electrocardiographic (ECG) signals to both identify the site of origin of the arrhythmia in the heart, and

guide the ablation catheter to the same site.

1.2 Thesis Description

Chapter 2

Life-threatening cardiac arrhythmias are a major health issue and yet the approaches taken to treat these arrhythmias have limited effectiveness. Radio-frequency catheter ablation, a promising new procedure for curing these arrhythmias, is an option available for only a limited number of patients because with current technology, it may take many hours for the cardiac electrophysiologist to identify the site of origin of the arrhythmia, and to guide the ablation catheter to that site. The patient must remain hemodynamically stable during the procedure, much of which may be spent with the arrhythmia ongoing because the arrhythmia must be induced in order to identify the location of its site of origin.

As part of this chapter, the currently available therapies and technologies used in treating cardiac arrhythmias are presented and the inadequacies and limitations that each approach entails are discussed. Yet, the need for a new methodology to guide the ablative therapy of cardiac arrhythmias is apparent.

However, the technique of radio-frequency ablation of the site of origin of an arrhythmia would be greatly facilitated if it were possible to localize this site from body surface potential measurements. A fundamental limitation on this approach is the fact that in general *the inverse problem in electrocardiography* has no unique solution. It is generally not possible to construct the three-dimensional distribution of cardiac electrical sources from the two-dimensional distribution of ECG signals obtained on the body surface.

However, if one knows that the source is localized then one can approximate the source with a single equivalent moving dipole (SEMD), for which one can in prin-

ciple compute its location and moments from body surface potential measurements. Generally, the source is not well localized, but may be localized for a portion of the cardiac cycle, for example for the period when the depolarization wavefront during ventricular tachycardia (VT) is emerging from the site of origin of the arrhythmia. If one can localize the site of origin of the arrhythmia during one point in the cardiac cycle then one can ablate it. Fitting the dipole parameters to body surface ECG signals provides a solution for the dipole location (as well as its strength and orientation). The location of the dipole at the point when the electrical activity is confined at the site of origin (point of earliest activation) should coincide with the site of origin of the arrhythmia. The location of the site of origin of the arrhythmia can be identified from only a few beats of the arrhythmia. On the other hand, if one delivers bipolar current pulses to the tip of the ablation catheter, records the resulting body surface signals, and uses the same inverse algorithm then one will be able to localize the tip of the catheter. Using this information one can in principle guide the tip of the catheter to the site of origin of the arrhythmia.

One of the major issues of this thesis is the ability to identify when two electrical sources are coincident: this will allow one to position the tip of the catheter on the site of origin of the arrhythmia using purely non-invasive means. However, the confounding factors of the proposed method involve the fact that the SEMD method as proposed here ignores boundary conditions and inhomogeneities in tissue conductivity. Thus the inverse solution obtained is distorted (not the true one). However, as long as the site of origin of the arrhythmia and the tip of the catheter are identified using the same algorithm, then when the two are brought together, both their positions will be distorted by the same amount. Thus the distortion due to the above factors should not significantly affect the accuracy to which one can make the tip of the ablation catheter and site of origin of the arrhythmia coincide.

The limitation in the ability to superpose the catheter tip and the arrhythmia

source thus depends on the random (as opposed to systematic) error in the localization of the dipole.

Chapter 3

We have developed an optimization algorithm to identify the SEMD parameters. We applied this algorithm to potential data obtained from computer simulations (presented in chapters 3 and 5) as well in ECG signals obtained from animal studies (presented in chapter 5), to investigate its accuracy in identifying the SEMD parameters.

In this chapter we present the optimization (fitting) methods considered to obtain the dipole parameters and we employ computer simulations to evaluate them. Three optimization algorithms were used: (i) the Fletcher-Reeves-Polak-Ribiere, (ii) the Davison-Fletcher-Powell and (iii) the Simplex. Six parameters, 3 for the dipole moments and 3 for the dipole location fully represent a dipole. For each algorithm both a 6 (searched for all 6 parameters) 3 *plus* 3 (solved exactly for the dipole moments and searched for the dipole location) approach, were implemented and evaluated for their (i) ability to converge, and (ii) accuracy.

We also evaluated potential objective functions (the minimization of which provides the SEMD parameter estimates) that would be appropriate for this problem.

We finally evaluated the effect of (i) measurement noise, and (ii) systematic error on the inverse solution obtained using a variety of objective functions.

An important issue raised in this thesis is identifying when two dipole sources are coincident. Consider a case where the two dipoles are coincident but differ in orientation; does this have a significant effect on our inverse algorithm's ability to identify them as coincidental?

Given the unknown orientation of the tip of the catheter relative to the SEMD position, one would like to know what is the uncertainty in the distance between the

SEMD position and the tip of the catheter when they are coincident but oriented in different directions.

In this chapter we introduced our newly developed inverse algorithm to identify the parameters of the SEMD. This algorithm is evaluated for its sensitivity to (i) measurement noise, (ii) dipole orientation.

Chapter 4

Cardiac electrical activity is highly distributed during most of the cardiac cycle.

In this chapter we use a computer simulation model to investigate the intrinsic limitations associated with representing cardiac electrical with a SEMD throughout the cardiac cycle.

We probe the temporal and spatial course of the applicability of the SEMD model by understanding when and where cardiac activation is highly localized.

Chapter 5

In this chapter we evaluated our inverse algorithm using ECG signals obtained from a series of animal experiments.

The experimental protocol and the data analysis scheme are also presented. The optimization algorithms and objective functions investigated in chapter 3 are evaluated on real data.

We evaluate the ability of our inverse algorithm to correctly predict the ECG signals. We form the median beat for each recording site from the first half of the ECG signals and use it to identify the SEMD dipole parameters. Then we use these parameters to reconstruct the ECG values (median beat) at the same sites and compare them against the median beat estimated from the second half of the ECG signals.

The dependence of the spatial SEMD parameter estimates to measurement noise as well as the beat-to-beat SEMD parameter estimates are evaluated.

The ability of our inverse algorithm to resolve the physical (actual) distance of two epicardial sites was evaluated, by observing the distance of the SEMD locations obtained from ECG signals recorded during pacing from two epicardial sites.

Chapter 6

In this chapter we summarize our results in terms of the uncertainty in the estimation of the spatial SEMD parameters under realistic conditions. We also present the final conclusions.

Chapter 7

In the final chapter of this thesis the impact which successful application of our algorithm may have in cardiac electrophysiology and society is discussed.

Also, suggestions and recommendations for future experiments are presented.



Lesvos Island - Mytilini, The island's capital (Edition: A&E Moliviatis)

Chapter 2

Background and Significance

2.1 The Problem

Cardiac arrhythmias, such as ventricular tachycardia (VT) and fibrillation, are the most prominent cause of morbidity and mortality in the industrialized world. After surviving the acute phase of myocardial infarction (heart attack caused by the obstruction of blood flow in a coronary artery), approximately 100,000 patients annually subsequently develop VT due to reentry in the infarct region (the region of the heart damaged by the loss of perfusion). These patients are subject to recurrent episodes, and anti-arrhythmic drug therapy fails to prevent episodes in about 40% of patients [19].

The standard regiments for VT prevention and treatment are, (i) anti-arrhythmic drug therapy (which prevents the onset of the arrhythmia via modification of the heart's electrical substrate), (ii) the implantable cardioverter defibrillator (which interrupts the arrhythmia through electric shocks), (iii) surgical ablation (which surgically modifies and interrupts the electrical pathways), and (iv) the latest technique, radiofrequency catheter ablation (RFA), which has similar objectives to surgical ablation except but is much less invasive.

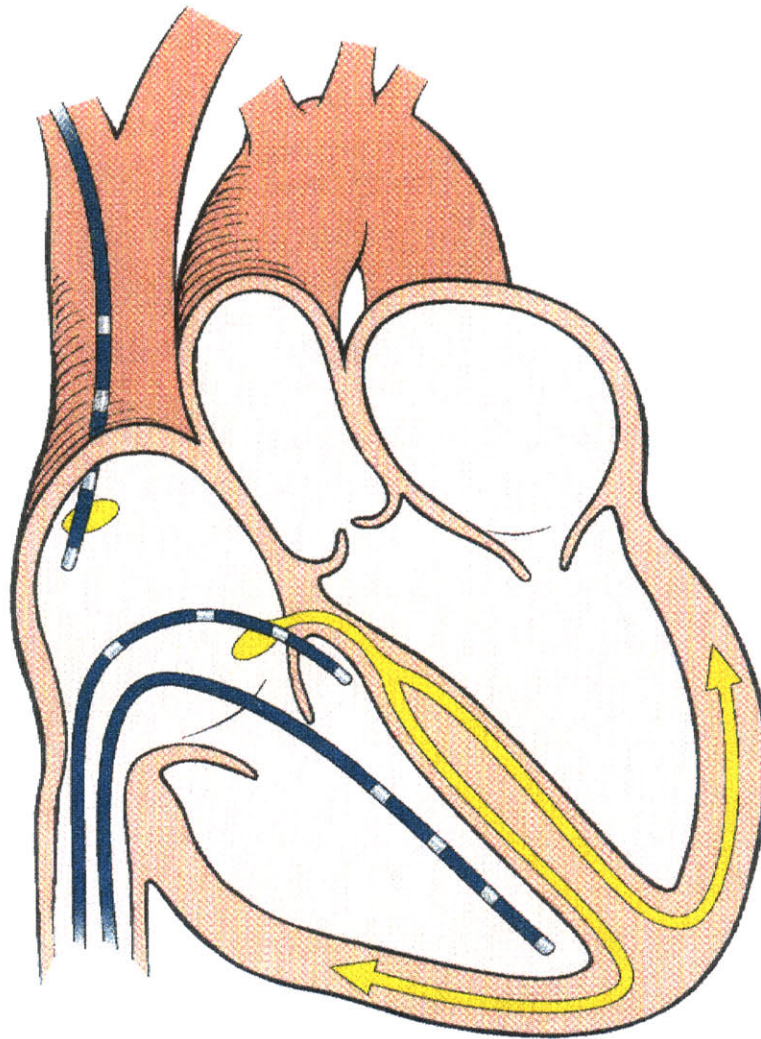
Since, the CAST study [11], anti-arrhythmic drug therapy has been shown to provide ineffective treatment for patients with life threatening ventricular tachyarrhythmias. Implantable cardioverter-defibrillators terminate the arrhythmia either by anti-tachycardia pacing or large individual shocks and, although they are life saving, their role is to restore the normal heart rhythm after it becomes abnormal rather than to prevent its onset. Ablation prevents the onset of VT by permanently modifying the reentry circuit responsible for the arrhythmia initiation and maintenance. Although, surgical ablation has been effective for selected patients, it requires a thoracotomy and has been associated with an operative mortality rate of 9% to 20% [12,80]. This technique has been replaced by RFA, in which a catheter placed inside the heart, is used to determine the site of the reentry circuit and deliver radio-frequency energy at the selected site [85,86] (Figure 2-1).

While RFA is more desirable from a cost and patient safety point of view the current approach entails detailed mapping of the arrhythmia and identification of its origin by sequentially positioning the catheter. This procedure may be time consuming and not well tolerated by the patient. Moreover, the mapping can be performed only when the VT is maintained under conditions that guarantee the well-being of the patient. Thus, only slow VTs can be successfully mapped.

Therefore, development of methodologies and therapies that would enable the reliable, safe and low-cost treatment of these patients, would expand the clinically available options.

The specific aim of this project is to develop a new technique that rapidly, reliably and safely identifies the site of origin of the arrhythmia so as to overcome the hurdles imposed by the current technology. In this chapter, we will first examine the conventional approach for guiding the RFA procedure. Secondly, we will consider innovative ideas for using non-invasive (body surface) electrocardiographic (ECG) signals as means of guiding the RFA procedure.

Figure 2-1 The catheter ablation set-up



2.2 Technical Considerations on Catheter Ablation

Catheter ablation procedures are performed in the cardiac electrophysiology laboratory. Three or four electrode catheters are inserted percutaneously into the femoral, internal jugular or subclavian vein and positioned within the heart to allow pacing

and recording at key sites (Figure 2-1).

Typical radio-frequency ablation catheters, which are 2.2 mm in diameter (7 French) and have a distal electrode 4 mm long, create lesions approximately 5 to 6 mm in diameter and 2 to 3 mm deep [73]. Radio-frequency current is alternating current that is delivered at cycle lengths of 300 to 750 kHz when used for catheter ablation. It causes resistive heating of the tissue in contact with the electrode. Irreversible tissue destruction requires a tissue temperature of approximately 50°C , while in most ablation procedures, the power output of the radio-frequency generator is adjusted to achieve a temperature of $60\text{--}75^{\circ}\text{C}$ at the tissue-electrode interface [10].

2.3 Clinical Considerations of Catheter Ablation

Sustained ventricular tachycardia is often a difficult arrhythmia to manage. One of the most common indications for radio-frequency catheter ablation of ventricular tachycardia is arrhythmia refractory to drug therapy that results in frequent discharges from an implantable cardioverter-defibrillator. RFA is also indicated when the VT is too slow to be detected by the implantable cardioverter-defibrillator or is incessant [87].

Selection of the appropriate target sites for ablation is usually based on a combination of anatomical and electrical criteria. The principal limitation of the RFA technique is the determination of the correct site for delivery of the radio-frequency energy. Conventionally, this determination is achieved by painstaking mapping of the electrical activity on the inner surface of the heart from electrodes on the catheter. Often, this recording must be done while the arrhythmia is ongoing.

The acute lesion created by radio-frequency current consists of a central zone of coagulation necrosis surrounded by a zone of hemorrhage and inflammation. Arrhythmias may recur if the target tissue is in the border zone of a lesion instead of the

central area of necrosis and if the inflammation resolves without residual necrosis, arrhythmias may recur several days to several weeks after an apparently successful ablation [42]. Conversely, the arrhythmia site of origin that was not initially successfully ablated, may later become permanently non-functional if it lies within the border zone of a lesion and if microvascular injury and inflammation within this zone result in progressive necrosis [56]. Thus, the efficacy and long-term outcome of catheter ablation depends on the site of origin of the arrhythmia.

Catheter ablation of sustained monomorphic ventricular tachycardia (VT) late after myocardial infarction has been challenging. These arrhythmias arise from reentry circuits that can be large and complex, with broad paths and narrow isthmuses, and that may traverse subendocardial, intramural, and epicardial regions of the myocardium [14, 38].

Mapping and ablation are further complicated by the frequent presence of multiple reentry circuits, giving rise to several morphologically different VTs [92, 93]. In some cases, different reentry circuits form in the same abnormal region. In other cases, reentry circuits form at disparate sites in the infarct area. The presence of multiple morphologies of inducible or spontaneous VT has been associated with antiarrhythmic drug inefficacy [50] and failure of surgical ablation [47].

Several investigators have reported series of studies of patients selected for having one predominant morphology of VT (“clinical VT”) and who were treated with radio-frequency catheter ablation [39, 51]. It is likely that this group of patients represents less than 10% of the total population of patients with VT [39]. The patient must remain hemodynamically stable while the arrhythmia is induced and maintained during mapping. The mapping procedure may take many hours during which the arrhythmia is maintained. Thus, currently radio-frequency catheter ablation is generally limited to “slow” ventricular tachycardia ($\cong 130$ bpm) which is most likely to be hemodynamically stable.

Ablation directed towards the “clinical tachycardia” that did not target other inducible VTs, successfully abolished the “clinical VT” in 71% to 76% cases. However, during follow-up up to 31% of those patients with successful ablation of the “clinical VT” had arrhythmic recurrences, some of which were due to different VT morphologies from that initially targeted for ablation.

Yet, there are several difficulties selecting a dominant, “clinical VT” for ablation. Often it is not possible to determine which VT is in fact the one that has occurred spontaneously. In most cases, only a limited recording of one or a few ECG leads may be available. In patients with implantable defibrillators VT is typically terminated by the device before an ECG is obtained. Even if one VT is identified as predominant, other VTs that are inducible may subsequently occur spontaneously. An alternative approach is not to consider the number of VT morphologies in determining eligibility for catheter ablation but rather to attempt ablation of all inducible VTs that are sufficiently tolerated to allow mapping [82, 83]. However, this approach requires that the patient be hemodynamically stable during the VT mapping procedure.

2.4 Mapping Techniques and Successful Ablation

Radio-frequency catheter ablation procedures have evolved in recent years to become an established treatment for patients with a variety of supraventricular [43, 44] and ventricular arrhythmias [81, 82]. However, in contrast to supraventricular tachycardia ablation that is highly successful because the atrio-ventricular node anatomy is known, ventricular tachycardia ablation remains difficult because the infarct could be anywhere in the ventricles.

Selection of the appropriate target sites for ablation is usually based on a combination of anatomical and electrical criteria. The ability of the physician to deliver radio-frequency energy through a catheter at the reentry site depends on the lim-

itations of the current technology to allow him/her to guide the catheter to the appropriate ablation site.

2.4.1 Fluoroscopic Guidance

Common to all clinical catheter ablation strategies is the use of fluoroscopy (digital bi-plane x-ray) for the guidance of the ablation catheter for the delivery of the curative radio-frequency energy. However, the use of fluoroscopy for these purposes may be problematic for the following reasons: (i) the inability to accurately associate intracardiac electrograms with their precise location within the heart, (ii) the endocardial surface is not visible using fluoroscopy and the target sites can only be approximated by their relationship with nearby structures such as ribs, blood vessels as well as the position of other catheters, (iii) due to the limitations of two dimensional fluoroscopy, navigation is frequently inexact, time consuming and requires multiple views to estimate the three-dimensional location of the catheter; (iv) the inability to accurately return the catheter precisely to a previously mapped site; (v) exposure of the patient and medical personnel to radiation.

2.4.2 Electro-anatomical Mapping

The *CARTOTM* (Biosense, Tirat Hacarmel, Israel) system provides an electro anatomical map of the heart. This method of non-fluoroscopic catheter mapping is based on an activation sequence to track and localize the tip of the mapping catheter by magnetic localization in conjunction with electrical activity recorded by the catheter. This approach has been used in ventricular tachyarrhythmia [53, 81], atrial flutter [28, 71] and atrial tachycardia ablation [41, 55]. The ability to localize in space the tip of the catheter while simultaneously measuring the electrical activity, may facilitate the mapping process. However, this technique fundamentally has the limitation that it involves sequentially sampling endocardial sites. The mapping process is prolonged

while the patients must be maintained in VT.

2.4.3 Basket Catheter

This approach employs a non-contact 64-electrode basket catheter (Endocardial Solutions Inc., St. Paul, MN, USA) placed inside the heart to electrically map the heart. In the first part of this procedure high frequency current pulses are applied to a standard catheter used in an ablation procedure. The tip of this catheter is dragged over the endocardial surface and a basket catheter is used to locate the tip of the ablation catheter and thus to trace and reconstruct the endocardial surface of the ventricular chamber. Then the chamber geometry, the known locations of the basket catheter and the non-contact potential at each electrode on the basket catheter are combined in solving Laplace's equation, and electrograms on the endocardial surface are computed. It has been used in mapping atrial and ventricular arrhythmias. [24, 70]. One of the drawbacks of this methodology is that the ventricular geometry is not fixed but varies during the cardiac cycle. In addition, the relative movement between the constantly contracting heart and the electrodes affect the mapping. While the inter-electrode distances on each sidearm of the basket catheter are fixed, the distances between the actual recording sites on the endocardium decrease during systole. This leads to relative movement between the recording electrode and the tissue, significantly limiting the accuracy of the mapping method.

2.5 Classic Electrocardiography

The ability to understand and characterize cardiac electrical activity as well as to discriminate normal from abnormal impulse formation, is a goal of great interest for both physicians and researchers. For that purpose the classic ECG signal offers a safe, inexpensive, non-invasive way of measuring this activity and is the basis of

many diagnostic techniques.

However, one cannot reconstruct the three-dimensional distribution of electrical activity in the heart from the potential distribution on the body surface (*the inverse problem*). Furthermore, the classic ECG electrodes significantly under-sample the distribution of electrical potentials on the torso surface. Also, one does not know the precise geometry of the chest and the spatial distribution of conductivities within the chest. Additionally, information about cardiac electrical activity is blurred and attenuated in the torso volume conductor, the medium between the heart and the body surface. As a result the standard ECG permits only a relatively coarse description of the spatial complexity of cardiac electrical activity thus its interpretation cannot be based on a rigorous biophysical model, but rather must depend on a heuristic match between waveforms and disease state.

Electrode arrays have been used to achieve denser spatial sampling along with geometrical models of the thorax, to better establish the relationship between cardiac electrical activity and torso surface potentials that led to the development of a technique called *body surface potential mapping*.

2.6 Body Surface Potential Mapping

Body surface potential mapping (BSPM) was, historically, the first detailed method used in human electrocardiography [91]. Unlike the standard 12-lead electrocardiography (ECG) which records electrical signals from nine selected sites, body surface potential mapping depicts the electrical activity of the heart as reflected on the entire surface of the torso. As a consequence, body surface maps (BSPMs) may contain important information of where in the heart a particular event may be located. During the last four decades, hundreds of studies have demonstrated that BSPMs contain important clinical diagnostic information for a wide range of cardiac abnormalities in-

cluding ischemia, infarction and cardiac rhythm disturbances. However, while BSPM can reliably identify major single cardiac electrical events [3, 18, 59, 74], it is quite limited in its ability to identify and resolve multiple simultaneous electrical events in the heart [1, 68]. A common problem that BSPM faces is the difficulty in relating body surface electrical features to specific intracardiac events because the potential at every point on the body surface is a weighted sum of electrical contributions coming from the entire heart. In addition, the volume conductor between the heart and the body smoothes and distorts the potential distribution [68, 77]. Thus, BSPMs are an attenuated, distorted, and smoothed reflection of the electrical activity of the heart. As a result, many regional events that occur on the cardiac surface do not produce clear-cut, recognizable events on the body surface.

2.7 Inverse Solutions in Terms of Epicardial Potentials

Because body surface potential mapping has limited ability to resolve the distributed nature of cardiac electrical activity invasive epicardial and endocardial mapping, have been utilized to characterize cardiac electrical processes. Yet, today's technological and engineering advancements make non- or minimally-invasive medical technologies very appealing to patients and physicians. One such methodology is known as inverse solutions.

A fundamental limitation of the inverse problem is that it is not possible to reconstruct from body surface measurements the three dimensional distribution of electrical sources in the heart. The solution is not unique. However, it is theoretically possible to reconstruct the potential distribution on the epicardial surface from a knowledge of the potential on the body surface, because there are no cardiac electrical sources between the epicardium and the body surface. In this case, one must know the de-

tailed geometry of the body and epicardial surfaces as well as the tissue conductivities in the body. However, one cannot in principle identify intracardiac sources with this approach [25, 46, 67].

Reconstruction of the epicardial potential distribution from body surface potentials is an ill conditioned problem from a mathematical point of view [27, 66], meaning that small perturbations in the measured data (due to noise, errors in the forward model, discretization effects, etc) can result in unbounded errors in the inverse solution. The ill conditioning is a mathematical reflection of physical phenomena that include the attenuation and smoothing effects of the volume conductor. Sharp spatial variations in the epicardial potentials are blurred or smoothed in the body surface potentials. Thus, a small amount of noise in the body surface potential will tend to be magnified in epicardial potentials estimated through an inverse procedure. Inverse solutions need to be stabilized by the incorporation of additional physiological information. The best known approach to this type of ill-conditioned inverse problem is known as regularization. Regularization seeks a compromise between a solution that matches the data but may be unrealistic and unstable, on the one hand, and fidelity to a constraint based on *a priori* knowledge (or assumptions) about a realistic, stable solution, on the other. The main features of epicardial potential distributions can often be roughly reconstructed by regularization approaches. However, due to the complex nature of epicardial potentials, the imposition of any single constraint fails to produce globally satisfactory solutions [46].

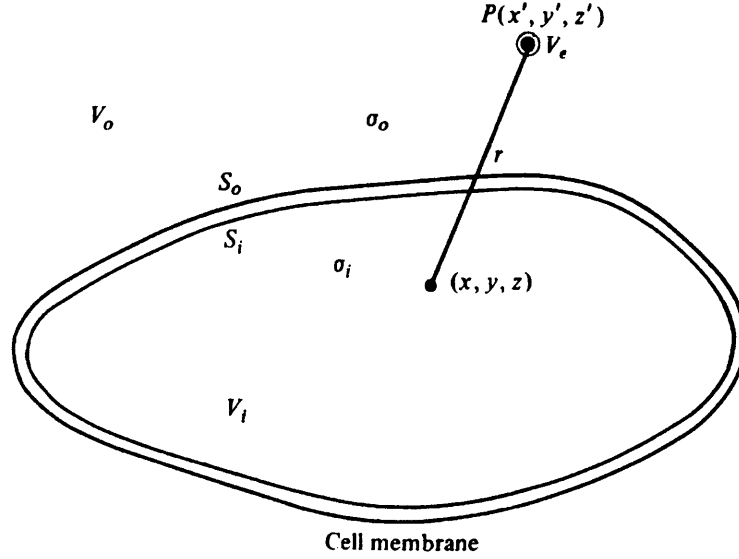
2.8 On the Equivalent Dipole Model

Let us consider the external potential field generated by a single cell immersed in a uniform conducting medium.

Figure 2-2 illustrates a single cell of external membrane surface S_o and internal

membrane surface S_i lying in an infinite volume conductor (V_o/V_i is the volume

Figure 2-2 Potential field of a single cell in an infinite volume conductor [62].



outside/inside the membrane surface). Then the potential at P is given by [62],

$$\phi(P) = \frac{1}{4\pi} \int_S \left(\frac{\sigma_i}{\sigma_o} \phi_i - \phi_o - \frac{m_d J_m}{\sigma_o} \right) d\Omega \quad (2.1)$$

where, $d\Omega$ is the solid angle subtended at P by a surface element dS and \mathbf{a}_r is the unit vector from the field to the source point, m_d is the cell membrane thickness, J_m is the outward membrane current density, ϕ_i/ϕ_o are the intracellular/extracellular potentials and σ_i/σ_o are the intracellular/extracellular conductivities respectively (Figure 2-3).

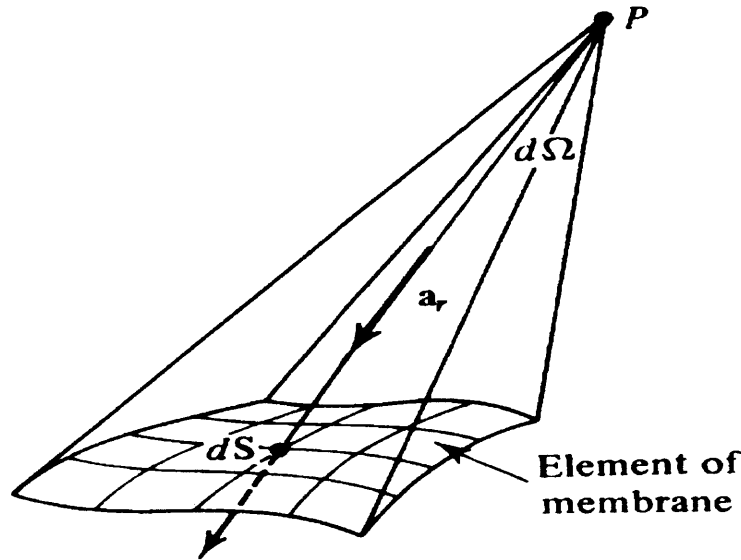
For a field point whose distance to the membrane is large compared with the membrane thickness ($\cong 100\text{\AA}$), the third term in the integral above is ordinarily negligible. Then by the definition of the solid angle

$$-\nabla\left(\frac{1}{r}\right) \cdot d\mathbf{S} = \frac{\mathbf{a}_r \cdot d\mathbf{S}}{r^2} = d\Omega \quad (2.2)$$

we obtain

$$\phi(P) = \frac{1}{4\pi\sigma_o} \int_S (\sigma_i \phi_i - \sigma_o \phi_o) d\mathbf{S} \cdot \nabla\left(\frac{1}{r}\right) \quad (2.3)$$

Figure 2-3 Solid angle geometry



But the potential field of a dipole source of strength \mathbf{p} is given by [62],

$$\phi(P) = \frac{1}{4\pi\sigma_o} \mathbf{p} \cdot \nabla\left(\frac{1}{r}\right) \quad (2.4)$$

so, $(\sigma_i\phi_i - \sigma_o\phi_o)d\mathbf{S}$ behaves like a dipole of magnitude $(\sigma_i\phi_i - \sigma_o\phi_o)d\mathbf{S}$ having the direction of the outward surface normal. The quantity $(\sigma_i\phi_i - \sigma_o\phi_o)$ can be interpreted, therefore, as a dipole moment per unit area or *double layer* in a medium with conductivity σ_o . We note that the local direction of the double layer is the local outward surface normal.

For the case of a medium of many active cells, equation 2.3 applies to every cell, where each cell is approximated by a single dipole. Thus, if the density is high, one may combine vectors associated with small groups of cells defining a local source dipole moment per unit volume (\mathbf{J}_i). This definition is a reasonable one because of the large number of cells, each of “infinitesimal” extent, compared to source field distances. We note that \mathbf{J}_i is an effective dipole moment per unit volume, and the representation is an equivalent one. Also, the accuracy of the computed field outside the source region depends on the accuracy with which \mathbf{J}_i represents the source density.

Then, we may write equation 2.3 in the form

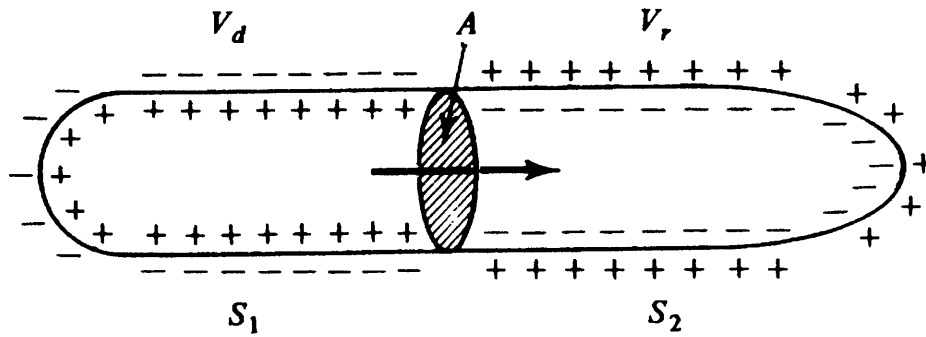
$$d\phi = \frac{1}{4\pi\sigma_o} \frac{\mathbf{a}_r}{r^2} \mathbf{J}_i dV \quad (2.5)$$

and finally by superposition the potential at P will be given by

$$\phi(P) = \frac{1}{4\pi\sigma_o} \int_V \frac{\mathbf{J}_i \cdot \mathbf{a}_r}{r^2} dV \quad (2.6)$$

Equation 2.3 also indicates that the potential due to the dipole moment (double

Figure 2-4 Dipole moment of a piece of partially depolarized tissue.



layer) is proportional to the area of the depolarized and non-depolarized interface (Figure 2-4).

2.9 Utility of the Equivalent Cardiac Generator

The concept of considering the heart as a single dipole generator originated by Einthoven [16] and its mathematical basis was concluded by Gabor and Nelson [21].

Several investigators [26, 49, 90] have studied the cardiac dipole in clinical practice and tried to determine the dipolar nature of the ECG. The advantages of the use of the equivalent cardiac dipole are (i) that it permits quantification of source strength in biophysical terms which are independent of volume conductor size (classic electrocardiography), (ii) the active equivalent source can be localized and assigned a location, something that cannot be done by the classical electrocardiography.

2.10 Could the Single Equivalent Moving Dipole Model Serve as a Tool in Guiding the Ablation Catheter to the Ablation Site?

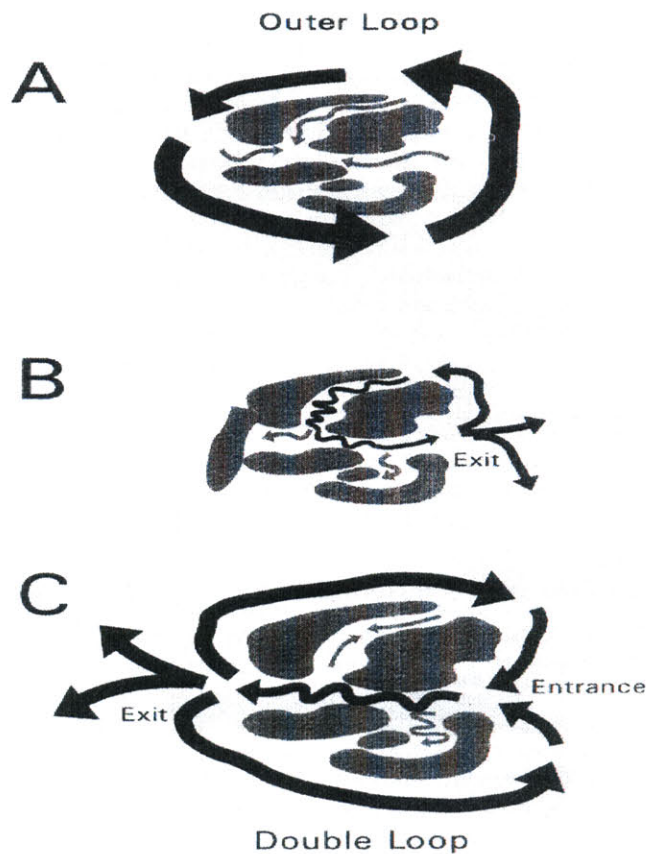
For many arrhythmias, the electrical activity within the heart is highly localized for a portion of the cardiac cycle (Figure 2-5, panel A). During the remainder of the cardiac cycle the electrical activity may become more diffuse as the waves of electrical activity spread (Figure 2-5, panels B and C).

Although, it is not possible to construct the three-dimensional distribution of cardiac electrical sources from a two-dimensional distribution of ECG signals obtained on the body surface, if it is known that the source is localized, then this localized area, at the interface of a partially depolarized tissue one can be approximated as a single equivalent moving dipole (SEMD), for which one can compute its location and moments.

If one can localize the site of origin of the arrhythmia during the cardiac cycle then one can ablate it. Fitting the dipole parameters to body surface ECG signals provides a solution for the dipole location (as well as its strength and orientation). The location of the dipole at the point when the electrical activity is confined at the site of origin should coincide with the site of origin of the arrhythmia. In contrast to standard mapping techniques the inverse solution could be computed from only a few beats of the arrhythmia eliminating the need for prolonged maintenance of the arrhythmia. In addition, if one delivers low-amplitude bipolar current pulses to the tip of the ablation catheter and records the resulting body surface signals using the same inverse algorithm, one will be able to localize the tip of the catheter. Using this information one can guide the tip of the catheter to the site of origin of the arrhythmia.

The confounding factors of the proposed method involve the fact that the SEMD method as proposed here ignores boundary conditions and inhomogeneities in tissue conductivity. Furthermore, even the exact electrode position in the three-dimensional space may not be accurately determined. Thus the inverse solution obtained is distorted (not the true one). However, as long as the site of origin of the arrhythmia and the tip of the catheter are identified using the same algorithm, then when the two are brought together, both their positions will be distorted by the same amount. In other words, when the algorithm identifies that the site of origin of the arrhythmia and catheter tip are at the same location, then they *are* at the same location. Thus the distortion due to the above factors should not significantly affect the accuracy to which one can make the tip of the ablation catheter and site of origin of the arrhythmia coincide.

Figure 2-5 Evolution of the activation wavefront around scar tissue. Configuration of three different reentrant circuits are shown. In each panel the gray regions are regions of conduction block, which could be due to fibrous scar or collision of excitation fronts. Black arrows indicate the circulating wavefronts. Smaller gray arrows indicate wavefronts propagating in “bystander” regions of the scar that are not in the reentry circuit. A. The circulating reentry wavefront propagates along the border of the infarct region. B. The reentry circuit is contained in the infarct region. C. Portion of the reentry circuit is contained within the infarct region, but following exit from the infarct region, two wavefronts travel along the border of the infarct to reach the proximal “entrance” to the reentry circuit path through the infarct, forming a double loop reentry circuit [79]





Lesvos Island - Petra (Edition: A&E Moliviatis)

Chapter 3

Development of Optimization

Methods and Results

3.1 Motivation

Throughout this thesis cardiac bio-electric sources are characterized in terms of a single equivalent moving dipole. A dipole is represented with 6 parameters: (i) three location parameters, and (ii) three moment parameters. In the real world these cardiac electrical sources give rise to the electrocardiographic (ECG) signals that one observes i.e on the body surface (*the forward problem*).

However, one may wish to obtain the dipole parameters from ECG signals that may be recorded i.e. on the body surface (*the inverse problem*). The necessary steps to accomplish this are: (i) use of a model that computes the values of the potential at known observation sites for a dipole with known location and moments (ii) use of ECG signals to fit the dipole parameters by minimization (optimization) of an *objective – function*, (iii) use of an algorithm that confirms that an estimated solution is accepted or not.

The first part of this chapter is concerned with the presentation and evaluation

of different optimization methods used in the identification of the dipole parameters. For that we used simulated potentials generated by a computer model to develop and evaluate the optimization methods used in this study. The optimization problem we solve is as follows: Given a single function f that depends on one or more independent variables we want to find the value of those variables where f takes on a minimum value. We then calculate the value f takes at the minimum. The computational cost is often dominated by the cost of evaluating the function f (and possibly its partial derivatives with respect to its variables).

In the second part of this chapter a newly developed algorithm aimed at identifying the “best” dipole parameter estimates from a given set of potentials is introduced.

In the third part of this chapter we identify the best objective function for this type of problem. In this case we examine the properties of potential objective-functions with respect to their ability to identify the optimal solution in the presence of measurement noise and systematic error due to boundary effects.

Also, the sensitivity of our inverse solution to both (i) measurement noise and, (ii) dipole orientation are also evaluated.

Finally, we evaluate the application of prediction error theory and the spatial distribution of the χ^2/dof (dof: degrees of freedom) around the best solution in the estimation of the uncertainty of the dipole location.

3.2 The optimization methods

The methods employed to solve the optimization problem were (i) a conjugate gradient method [7, 17], (ii) a variable metric method [13, 63], and (iii) the Simplex method [2, 57]. The main points of these methods are presented (without derivations) in this chapter for the interested reader. Both variable metric and conjugate gradient methods require that the function’s gradient at arbitrary points can be computed,

while the Simplex requires only the function.

The goal of the variable metric methods, which are sometimes called quasi-Newton methods, is not different from the goal of the conjugate gradient methods: to gather information from successive line minimizations so that M such line minimizations lead to the exact minimum of a quadratic form in M dimensions. In that case, the methods will also be quadratically convergent for more general smooth functions.

The variable metric approach differs from the conjugate gradient in the way that it stores and updates the information that is accumulated. Instead of requiring intermediate storage of the order M , the number of dimensions, it requires a matrix of size $M \times M$.

3.3 Conjugate Gradient Method

The concept of "non-interfering" directions, more commonly known as conjugate direction is based on the fact that when we minimize a function along some direction \mathbf{u} , the gradient of the function must be perpendicular to \mathbf{u} at the line minimum; if not, then there would still be a non-zero directional derivative along \mathbf{u} .

If we next take a particular point as the origin of the coordinate system with coordinates \mathbf{x} , then any function can be approximated by its Taylor series

$$\begin{aligned} E(\mathbf{x}) &= E(\mathbf{P}) + \sum_i \frac{\partial E}{\partial x_i} + \frac{1}{2} \sum_{ij} \frac{\partial^2 E}{\partial x_i \partial x_j} x_i x_j + \dots \\ &\approx c - \mathbf{b}^T \mathbf{x} + \frac{1}{2} \mathbf{x}^T \mathbf{H} \mathbf{x} \end{aligned} \quad (3.1)$$

where,

$$c \equiv E(\mathbf{P}), \quad \mathbf{b} \equiv -\nabla E|_{\mathbf{P}}, \quad [\mathbf{H}]_{ij} \equiv \left. \frac{\partial^2 E}{\partial x_i \partial x_j} x_i x_j \right|_{\mathbf{P}} \quad (3.2)$$

The components of the matrix \mathbf{H} are the second partial derivative matrix of the function is called the Hessian matrix of the function at \mathbf{P} . To introduce the conjugate

gradient algorithm we consider the case of a quadratic error function of the form given in eq (3.1). The local gradient of this error function is given by

$$\mathbf{g}(\mathbf{x}) = \mathbf{b} + \mathbf{H}\mathbf{x} \quad (3.3)$$

and the error function (3.1) is minimized at the point \mathbf{x}^* given from eq (3.3), by

$$\mathbf{b} + \mathbf{H}\mathbf{x}^* = \mathbf{0} \quad (3.4)$$

If we can find a set of M vectors (where M is the dimensionality of the parameter space) which are mutually conjugate with respect to \mathbf{H} , so that

$$\mathbf{d}_j^T \mathbf{H} \mathbf{d}_i = 0 \quad \mathbf{j} \neq \mathbf{i} \quad (3.5)$$

then it is easily shown that these vectors will be linearly independent if \mathbf{H} is positive definite. Such vectors therefore form a complete, but non-orthogonal, basis set in weight space. If we now start from some point \mathbf{x}_1 , and we wish to get the minimum \mathbf{x}^* of the error function we write the difference between the vectors \mathbf{x}_1 and \mathbf{x}^* as a linear combination of the conjugate direction vectors in the form

$$\mathbf{x}^* - \mathbf{x}_1 = \sum_{i=1}^M \alpha_i \mathbf{d}_i \quad (3.6)$$

and if we define

$$\mathbf{x}_j = \mathbf{x}_1 + \sum_{i=1}^M \alpha_i \mathbf{d}_i \quad (3.7)$$

then eq (3.6) can be written as an iterative equation in the form

$$\mathbf{x}_{j+1} = \mathbf{x}_j + \alpha_j \mathbf{d}_j \quad (3.8)$$

This represents a succession of steps parallel to the conjugate directions, with step lengths controlled by the parameters α_j . In order to find expressions for the α 's eq (3.6) is multiplied by $\mathbf{d}_j^T \mathbf{H}$ and make use of eq (3.4) to obtain

$$-\mathbf{d}_j^T (\mathbf{b} + \mathbf{H}\mathbf{x}_1) = \sum_{i=1}^M \alpha_i \mathbf{d}_j^T \mathbf{H} \mathbf{d}_i \quad (3.9)$$

where, from eq (3.5) we see that the terms in the right hand side of eq (3.9) decouple allowing an explicit solution for the α 's in the form

$$\alpha_j = -\frac{\mathbf{d}_j^T(\mathbf{b} + \mathbf{H}\mathbf{x}_1)}{\mathbf{d}_j^T\mathbf{H}\mathbf{d}_j} \quad (3.10)$$

The last equation can be written in a more convenient form. Using the conjugacy condition eq (3.5) we may re-write eq (3.7) in the form

$$\mathbf{d}_j^T\mathbf{H}\mathbf{x}_j = \mathbf{d}_j^T\mathbf{H}\mathbf{x}_1 \quad (3.11)$$

This allows the numerator of the right-hand-side of eq (3.10) to be written in the form

$$\mathbf{d}_j^T(\mathbf{b} + \mathbf{H}\mathbf{x}_1) = \mathbf{d}_j^T(\mathbf{b} + \mathbf{H}\mathbf{x}_j) = \mathbf{d}_j^T\mathbf{g}_j \quad (3.12)$$

where, $\mathbf{g}_j \equiv \mathbf{g}(\mathbf{x}_j)$, and where use of eq (3.3) has been made. Thus, α_j can be written in the form

$$\alpha_j = -\frac{\mathbf{d}_j^T\mathbf{g}_j}{\mathbf{d}_j^T\mathbf{H}\mathbf{d}_j} \quad (3.13)$$

In order to construct a set of mutually conjugate directions the first direction to be the negative gradient $\mathbf{d}_1 = -\mathbf{g}_1$ is selected, and then choosing each successive direction to be a linear combination of the current gradient and the previous search direction

$$\mathbf{d}_{j+1} = -\mathbf{g}_{j+1} + \beta_j\mathbf{d}_j \quad (3.14)$$

The coefficients β_j can be found by imposing the conjugacy condition eq (3.5) which gives

$$\beta_j = -\frac{\mathbf{g}_{j+1}^T\mathbf{H}\mathbf{d}_j}{\mathbf{d}_j^T\mathbf{H}\mathbf{d}_j} \quad (3.15)$$

So, finally the minimum of a general quadratic error function can be obtained in at most M steps. Starting from a randomly chosen point \mathbf{x}_1 , successive conjugate directions are constructed using eq (3.14) in which the parameters β_j are given by eq (3.15) while at each step the parameter vector is incremented along the corresponding direction using eq (3.8) in which the parameter α_j is given by eq (3.13). So far, the discussion has been limited to quadratic error functions. For a general non-quadratic error function, the error in the neighborhood of a given point is approximately quadratic. For a non-quadratic error function, the Hessian matrix will depend on the current parameter vector, and so will need to be re-evaluated at each step of the algorithm and thus the evaluation of \mathbf{H} becomes computationally costly. In fact, it turns out that the coefficients α_j and β_j can be found without explicit knowledge of \mathbf{H} . This leads to the *conjugate gradient algorithm*. Using eq (3.3) we may write

$$\mathbf{g}_{j+1} - \mathbf{g}_j = \mathbf{H}(\mathbf{x}_{j+1} - \mathbf{x}_j) = \alpha_j \mathbf{H} \mathbf{d}_j \quad (3.16)$$

and now from eq (3.15) we obtain

$$\beta_j = -\frac{\mathbf{g}_{j+1}^T (\mathbf{g}_{j+1} - \mathbf{g}_j)}{\mathbf{d}_j^T (\mathbf{g}_{j+1} - \mathbf{g}_j)} \quad (3.17)$$

If we now take the scalar product of eq (3.16) with \mathbf{d}_j and use the definition of α_j obtained by eq (3.13) we obtain

$$\mathbf{d}_j^T \mathbf{g}_{j+1} = 0 \quad (3.18)$$

where, by induction we obtain

$$\mathbf{d}_k^T \mathbf{g}_j = 0 \quad \text{for all} \quad k < j \leq M \quad (3.19)$$

From eqs (3.14) and (3.19) we obtain

$$\mathbf{d}_j^T \mathbf{g}_j = -\mathbf{g}_j^T \mathbf{g}_j \quad (3.20)$$

which, together with eq (3.19) allows eq (3.17) to be written in the form

$$\beta_j = -\frac{\mathbf{g}_{j+1}^T(\mathbf{g}_{j+1} - \mathbf{g}_j)}{\mathbf{g}_j^T \mathbf{g}_j} \quad (3.21)$$

which is the Polak-Ribiere form. From eq (3.14) it follows that \mathbf{d}_k is given by a linear combination of all previous gradient vectors

$$\mathbf{d}_k = -\mathbf{g}_k + \sum_{l=1}^{k-1} \gamma_l \mathbf{g}_l \quad (3.22)$$

and using eq (3.19) we obtain

$$\mathbf{g}_k^T \mathbf{g}_j = \sum_{l=1}^{k-1} \gamma_l \mathbf{g}_l^T \mathbf{g}_j \quad \text{for all } k < j \leq M \quad (3.23)$$

Since, the initial search direction is just $\mathbf{d}_1 = \mathbf{g}_1$, we can eq (3.19) to show that $\mathbf{g}_1^T \mathbf{g}_j = 0$ where by use of induction we get

$$\mathbf{g}_k^T \mathbf{g}_j = 0 \quad \text{for all } k < j \leq M \quad (3.24)$$

And from the orthogonality property of eq (3.24) together with eq (3.21) we obtain Fletcher-Reeves [17] form,

$$\beta_j = \frac{\mathbf{g}_{j+1}^T(\mathbf{g}_{j+1})}{\mathbf{g}_j^T \mathbf{g}_j} \quad (3.25)$$

The expressions for β_j are equivalent provided the error function is exactly quadratic. Finally, the decision of how far to move in the chosen direction is made through a “bracketed” line search algorithm. Each line search proceeds in two stages. The first stage is to bracket the minimum by finding three points $a < b < c$ along the search direction such that $E(a) > E(b)$ and $E(c) > E(b)$. If the error function is continuous, this ensures that there is a minimum somewhere in the interval (a, c) . The second stage is to locate the minimum itself. If the error function is smooth and continuous, this can be achieved by a process of parabolic interpolation. This involves fitting a quadratic polynomial to the error function evaluated at three successive points, and then moving to the minimum of the parabola. The process can be repeated

by evaluating the error function at the new point, and then fitting a new parabola to this point and two of the previous points. This leads to the very robust Brent's algorithm [7].

Since, it is desirable to avoid the use of the Hessian matrix to evaluate α_j even in the case of a quadratic error function, the correct value of α_j is found by performing a line minimization along the search direction. For general non-linear error functions, the local Hessian matrix need not be positive definite where the use of robust line minimization techniques ensures that the error can not increase at any step. In practice, since the error function may be far from quadratic, the algorithm generally needs to be run for many iterations until a sufficiently small error is obtained or until some other termination criterion is reached. During the running of the algorithm, the conjugacy of the search directions tends to deteriorate, and so it is common practice to restart the algorithm after M steps by resetting the search vector to the negative gradient direction.

If the function to be maximized or minimized is not quadratic in \mathbf{x} , the desired extremum will not be located in exactly M steps. In this instance Fletcher and Reeves suggest restarting the process in the direction of the steepest ascent or descent after every $M + 1$ iterations.

3.4 Variable Metric Method

In the conjugate gradient algorithm, implicit use was made of second-order information about the error surface, represented by the local Hessian matrix. Using the local quadratic approximation of the Hessian we can obtain directly an expression for the location of the minimum of the error function. From equation (3.1) for the particular case of a local quadratic approximation around a point \mathbf{x}^* which is minimum of the

error function we get

$$E(\mathbf{x}) = \mathbf{E}(\mathbf{x}^*) + \frac{1}{2}(\mathbf{x} - \mathbf{x}^*)^T \mathbf{H}(\mathbf{x} - \mathbf{x}^*) \quad (3.26)$$

and the gradient at any point \mathbf{x} is given by

$$\mathbf{g} = \nabla E = \mathbf{H}(\mathbf{x} - \mathbf{x}^*) \quad (3.27)$$

and so the parameter vector \mathbf{x}^* corresponding to the minimum of the error function satisfies

$$\mathbf{x}^* = \mathbf{x} - \mathbf{H}^{-1}\mathbf{g} \quad (3.28)$$

The vector $-\mathbf{H}^{-1}\mathbf{g}$ is known as the Newton direction. Alternative approaches, known as quasi-Newton methods or variable metric methods are based on eq (3.28) but instead of calculating the Hessian directly, and then evaluating its inverse, they build up an approximation to the inverse Hessian over a number of steps. The quasi-Newton approach involves generating a sequence of matrices $\mathbf{G}^{(\tau)}$ which represent increasingly accurate approximations to the inverse Hessian \mathbf{H}^{-1} , using only information on the first derivatives of the error function. The problems arising from Hessian matrices which are not positive definite are solved by starting from a positive-definite matrix and ensuring that the update procedure is such that the approximation to the inverse Hessian is guaranteed to remain positive definite. From the Newton formula, eq (3.28), we see that the parameter vectors at steps τ and $\tau+1$ are related to the corresponding gradients by

$$\mathbf{x}^{(\tau+1)} - \mathbf{x}^{(\tau)} = -\mathbf{H}^{-1}(\mathbf{g}^{(\tau+1)} - \mathbf{g}^{(\tau)}) \quad (3.29)$$

which is known as the quasi-Newton condition. The left hand-side is the finite step we need take to get to the exact minimum while the right-hand side is known once we have accumulated an accurate $\mathbf{G}^{(\tau)}$. This might be better than using the true Hessian. This can be understood by considering the descent directions of E at x ,

which are the directions along which E decreases. For the Newton direction eq (3.29) to be a descent direction, it must be

$$(\mathbf{g}^{(\tau+1)} - \mathbf{g}^{(\tau)})^T (\mathbf{x}^{(\tau+1)} - \mathbf{x}^{(\tau)}) = -(\mathbf{x}^{(\tau+1)} - \mathbf{x}^{(\tau)})^T \mathbf{H} (\mathbf{x}^{(\tau+1)} - \mathbf{x}^{(\tau)}) < 0 \quad (3.30)$$

that is \mathbf{H} must be positive definite. In general, far from a minimum there is no guarantee that the Hessian will be positive definite. The quasi-Newton methods start with a positive definite, symmetric approximation to \mathbf{H} , that usually is the unit matrix, and build up the approximating $\mathbf{G}^{(\tau)}$ in such a way that the matrix $\mathbf{G}^{(\tau)}$ remains positive definite and symmetric. The last statement guarantees that far from the minimum, the search moves in a downhill direction. Close to the minimum, the updating formula approaches the true Hessian converging quadratically. Fletcher and Powell [63] modified Davison's algorithm [13], and derived a formula for $\mathbf{G}^{(\tau+1)}$ in terms of $\mathbf{G}^{(\tau)}$ and a correction term

$$\begin{aligned} \mathbf{G}^{(\tau+1)} = \mathbf{G}^{(\tau)} &+ \frac{(\mathbf{x}^{(\tau+1)} - \mathbf{x}^{(\tau)}) \otimes (\mathbf{x}^{(\tau+1)} - \mathbf{x}^{(\tau)})}{(\mathbf{x}^{(\tau+1)} - \mathbf{x}^{(\tau)}) \cdot (\mathbf{g}^{(\tau+1)} - \mathbf{g}^{(\tau)})} \\ &- \frac{[\mathbf{G}^{(\tau)} \cdot (\mathbf{g}^{(\tau+1)} - \mathbf{g}^{(\tau)})] \otimes [\mathbf{G}^{(\tau)} \cdot (\mathbf{g}^{(\tau+1)} - \mathbf{g}^{(\tau)})]}{(\mathbf{g}^{(\tau+1)} - \mathbf{g}^{(\tau)}) \cdot \mathbf{G}^{(\tau)} \cdot (\mathbf{g}^{(\tau+1)} - \mathbf{g}^{(\tau)})} \end{aligned} \quad (3.31)$$

where \otimes denotes the outer product of two vectors.

3.5 Simplex Method

The downhill Simplex method is due to Nelder and Mead [2, 57]. The method relies only on function evaluations not derivatives. A Simplex is the geometrical figure consisting, in N dimensions, of $N+1$ points (or vertices) and all their interconnecting line segments, polygonal phases, etc. For example, in three dimensions, Simplex is a tetrahedron (not necessarily the regular one). The algorithm is then supposed to make its own way downhill through the complexity of an N -dimensional topography, until it encounters a minimum. The multidimensional minimization starts by giving

the algorithm a starting guess, that is an N -vector of independent variables for each of the $N + 1$ points that define an initial Simplex. Taking one (any) of these points as the initial starting point \mathbf{P}_o , then we can take the other N points to be

$$\mathbf{P}_i = \mathbf{P}_o + \lambda \mathbf{e}_i \quad (3.32)$$

where, the \mathbf{e}_i 's are N unit vectors, and where λ is constant which is a guess of the problem's characteristic length scale.

If we initially consider the minimization of a function of n variables (without constraints), and P_0, P_1, \dots, P_n are the $(n + 1)$ points in n -dimensional space, we write y_i for the function value at P_i , and define

$$h \text{ as the suffix such that } y_h = \max_i(y_i) \quad [h \text{ for "high"}]$$

$$l \text{ as the suffix such that } y_l = \min_i(y_i) \quad [l \text{ for "low"}]$$

If \bar{P} defines the centroid of the points with $i \neq h$, and write $[P_i P_j]$ for the distance from P_i to P_j , during the process P_h is replaced by a new point. Three operations are used-*reflection*, *contraction* and *expansion*. These are defined as follows: the reflection of P_h is denoted by P^* , and its coordinates are defined by the relation

$$P^* = (1 + \alpha)\bar{P} - \alpha P_h \quad (3.33)$$

where α is a positive constant, the *reflection coefficient*. Thus, P^* is on the line joining P_h and \bar{P} , on the far side of \bar{P} from P_h with $[P^* \bar{P}] = \alpha[P_h \bar{P}]$. If y^* lies between y_h and y_l , then P_h is replaced by P^* and a new Simplex is started again. If $y^* < y_l$, i.e. if reflection has produced a new minimum, then P^* is expanded to P^{**} by the relation

$$P^{**} = \gamma P^* + (1 - \gamma)\bar{P} \quad (3.34)$$

The *expansion coefficient* γ , which is greater than unity, is the ratio of the distance $[P^{**} \bar{P}]$ to $[P^* \bar{P}]$. If $y^{**} < y_l$, P_h is replaced by P^{**} and the process is restarted; while

if $y^{**} > y_l$ then the expansion is considered failed and P_h is replaced by P^* before restarting. The steps called reflections, are constructed in such a way that the volume of the Simplex is conserved (hence its non-degeneracy is maintained). If on reflecting P to P^* , $y^* > y_i$ for all $i \neq h$, i.e. that replacing P by P^* leaves y^* the maximum, then a new P_h is defined to be either the old P_h or P^* , whichever has the lower y value, and form

$$P^{**} = \beta P_h + (1 - \beta) \bar{P} \quad (3.35)$$

The *contraction coefficient* β lies between 0 and 1 and is the ratio of the distance $[P^* \bar{P}]$ to $[P \bar{P}]$. Then P^{**} is accepted for P_h and the process is restarted, unless $y^{**} > \min(y_h, y^*)$, i.e. the contracted point is worse than the better of P_h and P^* . For such a failed contraction all P_i 's are replaced by $(P_i + P_l)/2$ and the process is restarted. A failed expansion may be thought of as resulting from moving into a valley (P^*) but at an angle to the valley so that (P^{**}) is well up on the opposite slope. A failed contraction, although rarer, can occur when a valley is curved and one point of the Simplex is much farther from the valley bottom than the others; contraction may then cause the reflected point to move away from the valley bottom instead of towards it. If there is a situation where the Simplex is trying to "pass through the eye of a needle", it contracts itself in all directions, pulling itself in around its best point. The coefficients α , β , γ give the factor by which the volume of the Simplex is changed by the operations of reflection, contraction or expansion respectively. The Simplex is not very efficient in terms of the number of function evaluations that it requires.

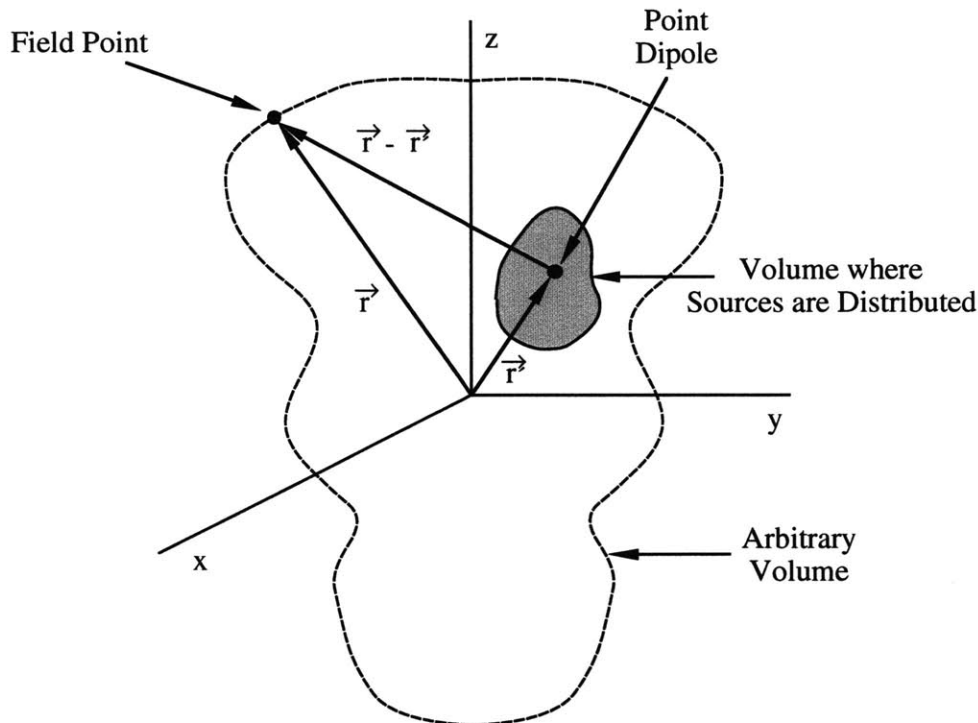
3.6 Techniques for Evaluation of Optimization Methods

The first of the computer simulations is concerned with the evaluation of the optimization methods in terms of their accuracy in identifying the true dipole.

3.6.1 The Models

For the forward problem formulation we considered two models: (i) an unbounded infinite homogeneous volume conductor and, (ii) a bounded spherical model.

Figure 3-1 The potential field in an infinite homogeneous medium; \mathbf{r} is the vector from the origin to the field point and \mathbf{r}' is the vector from origin to the point dipole.



The potential due to a single dipole in an infinite homogeneous medium (Figure 3-

1) is given by

$$\phi = \frac{\mathbf{p} \cdot (\mathbf{r} - \mathbf{r}')}{|\mathbf{r} - \mathbf{r}'|^3} \quad (3.36)$$

where,

\mathbf{r} , is the observation location,

\mathbf{p} , is the dipole moment,

\mathbf{r}' , is the dipole location

For the case of the bounded sphere the potential on the surface of the sphere (of radius $R = 12.5 \text{ cm}$) due to a dipole (p_x, p_y, p_z) located along the z-axis (at fR) has been presented by Geselowitz et al [23] to be

$$\begin{aligned} \phi = & \frac{p_z}{4\pi g f R^2} \left[\frac{1 - f^2}{(1 + f^2 - 2f\mu)^{3/3}} - 1 \right] \\ & + \frac{p_x \cos\psi + p_y \sin\psi}{4\pi g f R^2 \sin\theta} \left[\frac{3f - 3f^2\mu + f^3 - \mu}{(1 + f^2 - 2f\mu)^{3/2}} + \mu \right] \end{aligned} \quad (3.37)$$

where, $\mu = \cos\theta$, and θ and ψ are the azimuth and latitude respectively.

A random spaced grid (in θ and ϕ angles) on a hypothetical surface of a sphere was created and each site of the grid corresponded to an observation site (electrode location) $\mathbf{r}^i(\mathbf{r}^i, \theta^i, \phi^i)$. The radius of the hypothetical surface that the electrodes lie on is $r = 12.5 \text{ cm}$. Then the potential at each site in the grid was calculated using eq (3.36), and Gaussian noise (of standard deviation σ) was added to each potential value and the new value yielded the “measured” potential at the specific, i , site (ϕ_m^i); throughout these simulations 60 observation sites (“electrodes”) were selected.

The choice of the noise amplitude was guided by empirical knowledge that an ECG signal of the order of a few mV is usually corrupted by μV level noise.

3.6.2 The Objective Function

The objective function which we sought its minimization, in the inverse problem, to obtain the dipole parameter estimates is the χ^2/dof defined by

$$\chi^2/dof = \frac{1}{dof} \sum_{i=1}^I \left(\frac{\phi^i - \phi_m^i}{\sigma_i} \right)^2 \quad (3.38)$$

where,

ϕ^i , is the theoretical potential at location i ,

ϕ_m^i , is the measured potential at location i ,

σ_i , is the standard deviation of the measured potential at location i and here is taken to be the same for all electrodes

dof, is equal to the number of the measurement sites minus the number of the optimization parameters.

Provided that the measurement errors are actually normally distributed the quantity χ^2/dof is a sum of I squares of normally distributed quantities, each normalized to unit variance. In this case, the expected value of χ^2/dof is unity.

3.6.3 Calculation of the Derivatives of the Objective Function with Regard to the Dipole Parameters

Since, the Davison-Fletcher-Powell and the Fletcher-Reeves algorithms require calculation of the derivatives of the objective function (χ^2) in terms of the dipole parameters we now present those derivatives with regard firstly, to the dipole moment components

$$\begin{aligned} \frac{\partial \chi^2}{\partial p_k} &= \sum_{i=1}^I \frac{\partial \chi^2}{\partial \phi_m^i} \frac{\partial \phi_m^i}{\partial p_k} \\ &= 2 \sum_{i=1}^I \frac{\phi^i - \phi_m^i}{\sigma_i^2} \frac{r_k^i - r_k'}{|\mathbf{r}^i - \mathbf{r}'|^3}, \quad k = 1, 2, 3 \end{aligned} \quad (3.39)$$

and secondly the dipole location components

$$\begin{aligned}\frac{\partial \chi^2}{\partial r'_k} &= \sum_{i=1}^I \frac{\partial \chi^2}{\partial \phi^i} \frac{\partial \phi^i}{\partial r'_k} \\ &= 2 \sum_{i=1}^I \frac{\phi^i - \phi_m^i}{\sigma_i^2} \frac{\partial \phi^i}{\partial r'_k}\end{aligned}\quad (3.40)$$

where,

$$\frac{\partial \phi^i}{\partial r'_k} = -\frac{p_k}{|\mathbf{r}^i - \mathbf{r}'|^3} + \frac{3 \left(\sum_{j=1}^3 p_j (r_j^i - r'_j) \right) (r_k^i - r'_k)}{|\mathbf{r}^i - \mathbf{r}'|^5} \quad (3.41)$$

3.6.4 The 3 plus 3 Parameter Optimization Method

Because of the linear dependence of the potential (eq 3.36) on the dipole moments parameters, the latter can be separated from the spatial dipole parameters

$$\phi^i = \frac{\sum_{j=1}^3 p_j (r_j^i - r'_j)}{|\mathbf{r}^i - \mathbf{r}'|^3} \quad (3.42)$$

Consequently, any optimization method may be applied to the spatial parameters only, while an analytic optimization procedure may be performed to obtain the optimal fitting dipole moment parameters for a specific set of dipole spatial parameters and we coin the term *3 plus 3 parameter optimization* for this algorithm.

Using the χ^2 as an objective function the optimal dipole moment components (p_x, p_y, p_z) at each dipole location can be obtained by solving the following system of equations

$$\begin{aligned}0 &= \frac{\partial \chi^2}{\partial p_k} \\ &= \sum_{i=1}^I \frac{\partial \chi^2}{\partial \phi_m^i} \frac{\partial \phi_m^i}{\partial p_k} \\ &= 2 \sum_{i=1}^I \frac{\phi^i - \phi_m^i}{\sigma_i^2} \frac{r_k^i - r'_k}{|\mathbf{r}^i - \mathbf{r}'|^3}, \quad k = 1, 2, 3\end{aligned}\quad (3.43)$$

and after substituting eq (3.36) in the last one, we obtain

$$\sum_{j=1}^3 p_j \alpha_{kj} = \beta_k \quad (3.44)$$

that can be solved for all p_k 's, and where

$$\alpha_{kj} = \sum_{i=1}^I \frac{1}{\sigma_i^2} \frac{(r_k^i - r'_k)(r_j^i - r'_j)}{|\mathbf{r}^i - \mathbf{r}'|^6} \quad (3.45)$$

$$\beta_k = \sum_{i=1}^I \frac{1}{\sigma_i^2} \frac{\phi_m^i (r_k^i - r'_k)}{|\mathbf{r}^i - \mathbf{r}'|^3} \quad (3.46)$$

Thus, the potential is now given from an equation of the form $\phi^i = \phi^i(\hat{\mathbf{p}}(\mathbf{r}'), \mathbf{r}')$, where $\hat{\mathbf{p}}(\mathbf{r}')$ represents the optimal dipole moment at the location r' . We may now minimize the error in terms of the dipole location components, by taking

$$\begin{aligned} \frac{\partial \chi^2}{\partial r'_k} &= \sum_{i=1}^I \frac{\partial \chi^2}{\partial \hat{\phi}^i} \left(\sum_{j=1}^3 \frac{\partial \hat{\phi}^i}{\partial \hat{p}_j} \frac{\partial \hat{p}_j}{\partial r'_k} + \frac{\partial \hat{\phi}^i}{\partial r'_k} \right) \\ &= \sum_{j=1}^3 \frac{\partial \hat{p}_j}{\partial r'_k} \left(\sum_{i=1}^I \frac{\partial \chi^2}{\partial \hat{\phi}^i} \frac{\partial \hat{\phi}^i}{\partial \hat{p}_j} \right) + \sum_{i=1}^I \frac{\partial \chi^2}{\partial \hat{\phi}^i} \frac{\partial \hat{\phi}^i}{\partial r'_k} \end{aligned} \quad (3.47)$$

where $\hat{\phi}^i$ represents the potential at \mathbf{r} due to the optimal dipole. But from eq(3.43), we see that the sum in the parenthesis of eq (3.47) is zero, so

$$\begin{aligned} \frac{\partial \chi^2}{\partial r'_k} &= \sum_{i=1}^I \frac{\partial \chi^2}{\partial \hat{\phi}^i} \frac{\partial \hat{\phi}^i}{\partial r'_k} \\ &= 2 \sum_{i=1}^I \frac{\hat{\phi}^i - \phi_m^i}{\sigma_i^2} \frac{\partial \hat{\phi}^i}{\partial r'_k} \end{aligned} \quad (3.48)$$

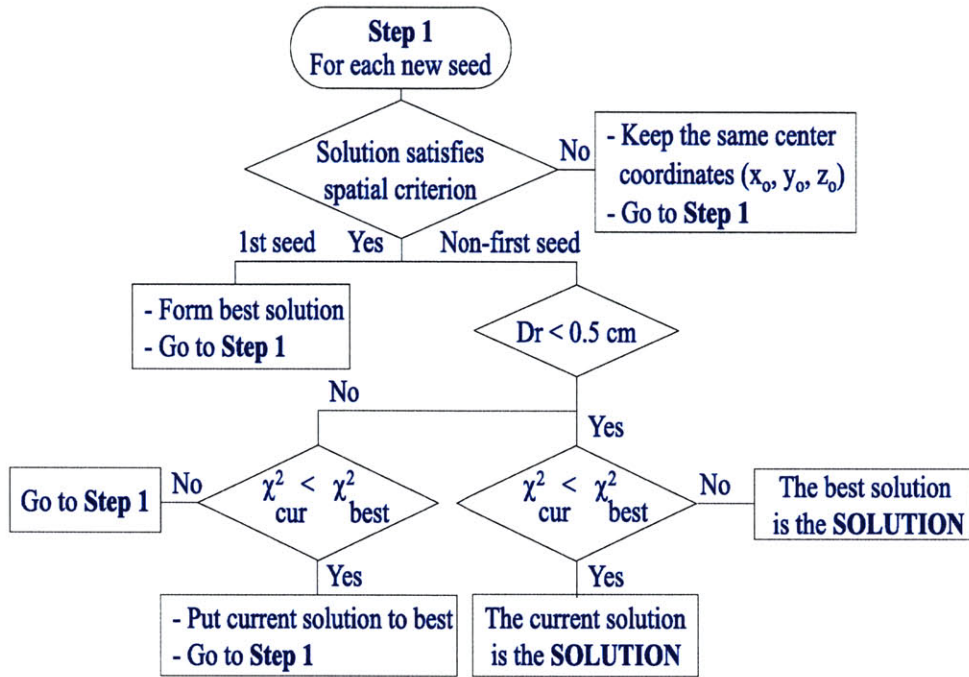
where,

$$\frac{\partial \hat{\phi}^i}{\partial r'_k} = -\frac{\hat{p}_k}{|\mathbf{r}^i - \mathbf{r}'|^3} + \frac{3 \left(\sum_{j=1}^3 \hat{p}_j (r_j^i - r'_j) \right) (r_k^i - r'_k)}{|\mathbf{r}^i - \mathbf{r}'|^5} \quad (3.49)$$

3.7 An Optimization Algorithm for the Estimation of the Single Equivalent Moving Dipole Parameters

We developed an inverse algorithm (Figure 3-2) that allows us to estimate the parameters of a single dipole by fitting the dipole parameters to the potentials obtained by

Figure 3-2 The algorithm used in the dipole parameter estimation.



an arbitrary source distribution, and using an optimization procedure to minimize an objective function. It employs a multiple seed value search (maximum of ten seeds). A spatial criterion was also imposed to force solutions to land inside a predefined volume. If during the search by the optimization method, a solution was found outside a predefined volume (that can be thought as the body), the value of the objective function was increased to force the optimization method to move the solution back into the specified volume. The algorithm terminated when two solutions were found to be closer than 0.5 cm. If after ten seeds were used, there were no solutions found that satisfied the spatial criterion and were closer than 0.5 cm, the algorithm outcome was considered non-convergent.

3.8 Numerical Studies and Results

The performance of the three optimization algorithms and for each of the two methods presented (6 or 3 *plus* 3 parameters) was evaluated in a series of simulation measurements.

These simulations were conducted with the following levels of measurement noise: 0.001, 0.01, 0.1 and 1.0 *mV*. The noise levels used here correspond to low, moderate, high and very high experimental noise levels. The typical magnitude of body surface ECG QRS complexes is on the order of a few mV.

It is important to note that there may be more than one solution to the inverse dipole problem. One may lie within the surface on which the potential measurements are made and a second may lie outside that surface. Thus we need to restrict the acceptable solutions to those that are physically meaningful, that is within the surface on which the measurements are taken. Furthermore, we may wish to further restrict the acceptable solutions to within a known volume within that surface. A case of an unwanted but still “admissible” solution is presented in Appendix A, where clearly the estimated solution cannot be accepted.

The spatial criterion provided information about the ability of each of the optimization methods to convergence in a restricted volume that in a realistic example could be the heart.

3.8.1 Application of the Inverse Algorithm in Evaluating the Spatial Uncertainty of the Dipole Identification Using All Optimization Methods

We have previously presented in this chapter three optimization methods: (i) the Davison-Fletcher-Powell (DFP), (ii) the Fletcher-Reeves-Polak-Ribiere (FRPR) and (iii) the Simplex, and two optimization approaches (i) a 6 parameter, and (ii) a

3 *plus* 3 parameter one (the overall number of methods was 6).

In this section, in computer simulations, we used the algorithm presented in Figure 3-2 to evaluate the accuracy of each of the 6 methods in identifying the dipole parameters.

We statistically analyzed the difference of the distance between the true and the estimated dipole location. The set-up of the simulation involved 100 runs for each one of which we (i) randomized the dipole location in a 5 cm radius sphere centered at (0,0,5) cm, (ii) we randomized the orientation of the dipole (see below); the magnitude of the dipole was fixed at 10 mVcm², (iii) added a different realization noise. As described before the electrodes were distributed over a hypothetical surface of 12.5 cm radius sphere centered at the origin. The dipole parameters were estimated through use of the algorithm presented in Figure 3-2.

Since the differential solid angle is given by $d\Omega = \sin(\theta)d\theta d\phi = d(\cos(\theta))d\phi$ we randomized $\cos(\theta)$ in the interval [-1,1] to obtain the dipole θ angle and randomized the ϕ angle in the interval $[0,2\pi]$.

The statistical analysis involved measuring the difference in the distance between the true and the estimated dipole location that corresponded to the one- and two-thirds fractiles of the distribution of solutions for each of the spatial dipole parameters. Assuming the estimated parameters followed a Gaussian distribution, the standard deviation of each parameter was estimated by the one-third and two-thirds of the values of that distribution from eq (3.50)

$$\sigma_i = \frac{\Delta X_{i_{2/3}} - \Delta X_{i_{1/3}}}{0.861} \quad (3.50)$$

Finally, the overall uncertainty σ was obtained from eq (3.51)

$$\sigma^2 = \sigma_x^2 + \sigma_y^2 + \sigma_z^2 \quad (3.51)$$

Also, the median of the difference for each of the spatial dipole parameters was

Table 3.1: Comparison of the *median* \pm *uncertainty* of the true minus the estimated solution using the 3 *plus* 3 parameter and the 6 *parameter* approaches, for each of the Davison-Fletcher-Powell (DFP), Fletcher-Reeves-Polak-Ribiere (FRPR) and Simplex methods for different noise realizations, σ_n (in parenthesis is the percent of runs which yielded convergent results). NC: Non-convergent

σ_n (m V)	3 PLUS 3 PARAMETERS		
	DFP	FRPR	Simplex
0.001	0.0001 \pm 0.0009 (40%)	0.0001 \pm 0.0007 (60%)	0.00004 \pm 0.0004 (100%)
0.01	0.0021 \pm 0.0090 (50%)	0.0004 \pm 0.0062 (63%)	0.00038 \pm 0.0038 (100%)
0.1	0.0045 \pm 0.0542 (90%)	0.0026 \pm 0.0419 (96%)	0.00374 \pm 0.0350 (100%)
1.0	0.0597 \pm 0.4059 (83%)	0.0735 \pm 0.3520 (94%)	0.03116 \pm 0.3888 (100%)

σ_n (m V)	6 PARAMETERS		
	DFP	FRPR	Simplex
0.001	NC	NC	5.5624 \pm 6.2824 (100%)
0.01	NC	NC	4.9858 \pm 6.9022 (100%)
0.1	3.1267 \pm 3.6296 (2%)	4.8987 \pm 2.9566 (3%)	4.7598 \pm 6.8981 (100%)
1.0	6.4196 \pm 8.5993 (100%)	12.500 \pm 12.409 (100%)	4.7112 \pm 6.5047 (100%)

estimated from eq (3.52)

$$D_{med}^2 = D_{med,x}^2 + D_{med,y}^2 + D_{med,z}^2 \quad (3.52)$$

The convergence success rate of each method was evaluated by the number of times out of the 100 runs that the algorithm converged.

The results of the analysis are summarized in Table 3.1. In each cell the median \pm the standard deviation and the convergence success rate for each of the methods and for each of the different noise levels are shown.

We see that the 3 *plus* 3 parameter implementation of the Simplex method was the most robust method presenting the highest convergence success rate for either

the 6 or the 3 *plus* 3 parameter implementation. We also observed that the 3 *plus* 3 parameter implementation of the Simplex method provided a median value of the distance of the true minus the estimated dipole locations closest to zero for all noise levels and the smallest standard deviation.

3.8.2 Selection of the Objective Function

The assumption that in a realistic case the detailed torso anatomy would be approximated with an infinite homogeneous volume conductor, makes the systematic error an important source of error compared to the measurement noise. Thus, the accuracy of any optimization algorithm would be sensitive to the selection of the objective function through the minimization of which the dipole parameter estimates are obtained. In this section we considered three objective functions which we statistically evaluated in their ability to identify the dipole parameters, in the case of two forward models (i) the unbounded infinite homogeneous volume conductor and (ii) the bounded sphere.

We evaluated three objective functions: (i) the χ^2/dof presented in eq (3.38), (ii) the root normalized mean square error (RNMSE)

$$RNMSE = \frac{\sum_{i=1}^I (\phi^i - \phi_m^i)^2}{\sum_{i=1}^I (\phi_m^i)^2} \quad (3.53)$$

and (iii) the *double root mean square error* coefficient

$$RDNMSE = \sum_{i=1}^I \frac{(\phi^i - \phi_m^i)^2}{(\sigma_i)^2 + (\phi_m^i)^2} \quad (3.54)$$

For the case of the unbounded volume conductor we used eq (3.36) to obtain the potential on a hypothetical surface conductor of the same radius (R) with the one that was for the bounded spherical model.

For the case of the bounded sphere the potential on the surface of the sphere was given by eq (3.37).

Table 3.2: Comparison of the objective function criteria using the inverse algorithm in identifying the spatial dipole parameters.

σ_n (mV)	χ^2/dof	
	Unbounded	Bounded
0.001	0.00003 \pm 0.0002 (100%)	0.78472 \pm 4.6512 (100%)
0.01	0.00027 \pm 0.0017 (100%)	0.78423 \pm 4.6523 (100%)
0.1	0.00103 \pm 0.0197 (100%)	0.78250 \pm 4.6679 (100%)
1.0	0.01159 \pm 0.1622 (100%)	0.61567 \pm 4.2041 (100%)

σ_n (mV)	RNMSE	
	Unbounded	Bounded
0.001	0.00003 \pm 0.0003 (100%)	0.80501 \pm 4.8493 (100%)
0.01	0.00057 \pm 0.0040 (100%)	0.80531 \pm 4.8447 (100%)
0.1	0.00657 \pm 0.0389 (100%)	0.75607 \pm 5.2682 (100%)
1.0	0.01852 \pm 0.4126 (100%)	0.71044 \pm 5.1132 (100%)

σ_n (mV)	RDNMSE	
	Unbounded	Bounded
0.001	0.00037 \pm 0.0042 (94%)	1.13388 \pm 5.3726 (97%)
0.01	0.00771 \pm 0.0473 (92%)	0.72055 \pm 5.7765 (97%)
0.1	0.02732 \pm 0.2870 (95%)	1.24999 \pm 6.0894 (92%)
1.0	0.17764 \pm 0.8762 (94%)	1.00476 \pm 5.9884 (97%)

The different objective functions tested here weighted the residuals at different electrodes based on the standard deviation of the noise and/or the magnitude of the measured potential. For this reason, to test the efficacy of the different objective functions it is necessary to conduct simulations with different noise levels at different electrodes. Thus, for each simulation we randomly selected the standard deviation of the noise at each electrode from a uniform distribution ranging from zero to 2α (we refer to α as the mean standard deviation of the noise; α is set to σ_n shown in

Table 3.2).

We again ran 100 simulations, in each of which in addition to randomizing the noise level at each electrode, we randomized the dipole location, the orientation of the dipole, and used different noise realizations.

One of the reasons to consider different objective functions, is that they may handle random versus systematic error in different ways. For this reason, we used two models in these simulations (100 simulations per model). One was the unbounded volume conductor eq (3.36) which exactly matched the assumptions of the ideal model assumed in the optimization method (no boundaries and no inhomogeneities in tissue conductivity). The second model is the bounded model eq (3.37). This model introduces systematic error in the estimation of the dipole parameters, because this model does not match the assumptions of the ideal model used in the optimizations.

We analyzed the difference of the distance between the true and the estimated dipole location for each of the above mentioned models in a computer simulation. The dipole parameters were obtained through use of the algorithm presented in Figure 3-2.

The results of this analysis presented are in Table 3.2. Each cell of the table includes the median (obtained from eq (3.52)) \pm the standard deviation (obtained from eq (3.51)) of the distance of the true minus the estimated dipole locations, and also the convergence success rate.

In the unbounded model, the χ^2/dof performed better than RNMSE and RDNMSE. The unbounded model involves no systematic error, because the inverse algorithm uses the same idealized formula (eq (3.36)) for the potential as represented in the unbounded model.

In the case of the bounded model, the median and standard deviation are much larger, because with each randomization of dipole location and orientation a different systematic error is introduced. This systematic error results from the fact that the formula for the potential used by the inverse algorithm differs from that used in the

bounded model. In the case of the bounded model χ^2/dof performed significantly better than the RDNMSE objective function and slightly better than the RNMSE objective function.

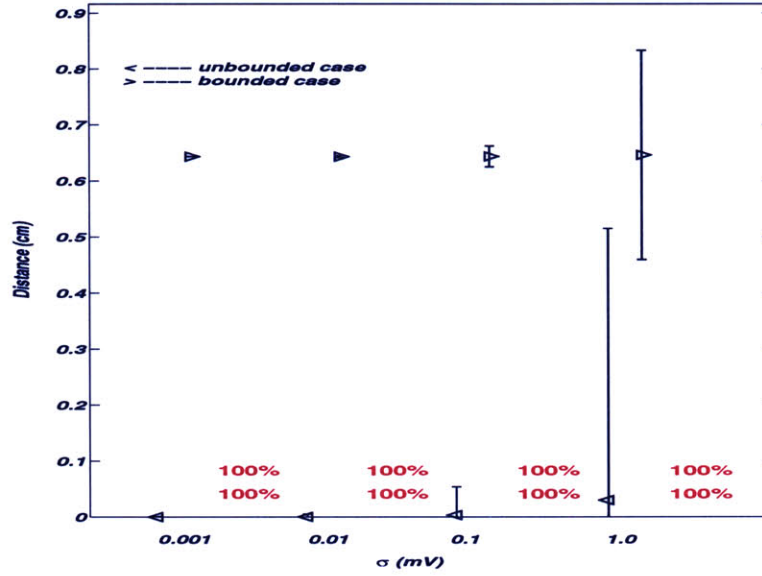
3.8.3 Effect of the Measurement Noise on the Uncertainty of the Spatial Dipole Parameter Estimation

In this section we evaluate the effect of measurement noise on the uncertainty of the spatial dipole parameter estimation. Measurement noise is responsible for the purely random component of the uncertainty. We statistically analyzed the distance between the true and the estimated location of a dipole in a computer simulation. The set-up of the simulation involved using a dipole at a fixed position $(0, 0, 5)$ cm with fixed moments components $(|P| = 10 \text{ mV cm}^2, \theta_d = 45^\circ, \phi_d = 270^\circ)$, and 100 runs were attempted for each one of which we used (i) a different noise realization (taken from the same distribution), (ii) the dipole parameters were obtained through use of the algorithm presented in Figure 3-2. The electrodes were taken on a spherical surface of radius 12.5 cm

Two forward models were employed: (i) the infinite homogeneous volume conductor (eq (3.36)), (ii) and the bounded conducting sphere (eq (3.37)). In the inverse problem the infinite homogeneous volume conductor model was used.

In Figure 3-3 and Table 3.4, we examine the effect of measurement noise on the ability of the algorithm to resolve the true dipole location. We plot the median and one standard deviation of the distance of the true minus the estimated dipole locations. Noise levels that ranged from μV to mV (equivalent to the dipole generated potentials) were used. We see that measurement noise has no significant effect until it becomes of comparable magnitude to the measured potentials. We also see that the systematic error causes a steady offset to the median solution from the true solution, but the standard deviations are comparable.

Figure 3-3 Effect of the measurement noise estimate on the dipole spatial parameter estimation. The median distance (“<” indicates the unbounded and “>” indicates the bounded case) and standard deviation between the true and the estimated location of a dipole are shown. The convergence rate for each of the two cases (unbounded and bounded) is also shown.

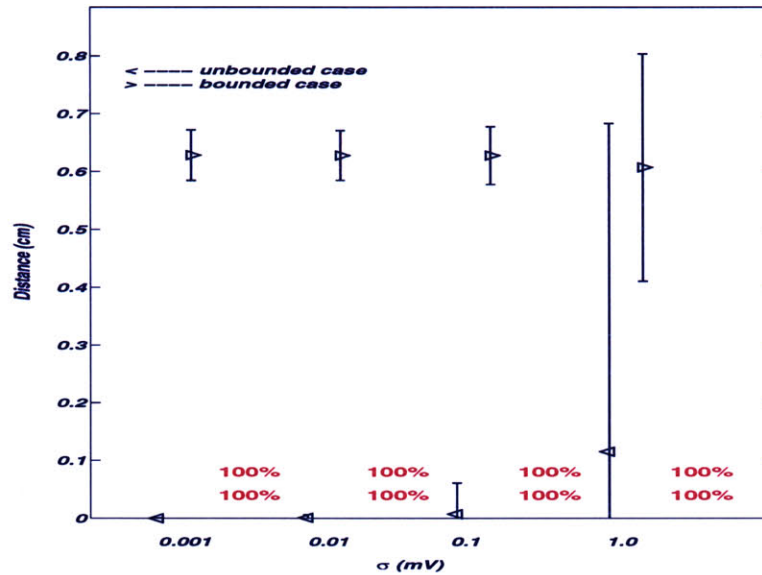


3.8.4 Effect of Dipole Orientation on the Uncertainty of the Spatial Dipole Parameter Estimation

We also examined the effect of both (i) measurement noise and (ii) dipole orientation on the ability of the algorithm to identify the equivalent dipole. We statistically analyzed the distance between the true and the estimated location of a dipole in a computer simulation. The set-up of the simulation involved 100 runs for each one of which we used a dipole at a fixed position (0, 0, 5) cm with magnitude 10 mVcm^2 . In each run we randomized the dipole orientation and used a different noise realization (taken from the same distribution). The dipole parameters were obtained through use of the algorithm presented in Figure 3-2. The electrodes were taken on a spherical surface of radius 12.5 cm.

Two forward models were employed: the (i) infinite homogeneous volume conductor (eq (3.36)), (ii) and the bounded conducting sphere (3.37). In the inverse problem the infinite homogeneous volume conductor model was used. In Figure 3-4 we again

Figure 3-4 Effect of the dipole orientation (for random solid angle Ω) on the uncertainty of the dipole spatial parameter estimation. The median distance (“<” indicates the unbounded and “>” indicates the bounded case) and standard deviation between the true and the estimated location of a dipole are shown. The convergence rate for each of the two cases (unbounded and bounded) is also shown.



plotted the median and standard deviation of the distance of the true minus the estimated dipole locations. In Figure 3-4 and Table 3.4 we observed that randomization of the solid angle did increase the standard deviation of the estimation at low noise levels in the case of the bounded spherical model, but that standard deviation is still small ($\cong 0.04$ cm). In the case of the unbounded homogeneous volume conductor randomization of the dipole did not increase the uncertainty.

3.9 Parameter Confidence Interval Estimation from the Prediction Error Theory

Since it is not enough to compute a vector $\hat{\boldsymbol{\theta}}$ (*hat* gives the *optimal* solution) and to state that this is the estimated value of the unknown parameter $\boldsymbol{\theta}$, we must also investigate the reliability and precision of the estimates. The prediction error approach is covered in [4] and here we will summarize the major themes around it. The assumptions that the derivation framework is based on are that (i) the number of electrodes is large; (ii) the residuals (difference between measured and predicted potential) are white; (iii) there is one global minimum and that minimum corresponds to the true dipole parameters. If we suppose that our estimate is an unconstrained minimum of some objective function $\Phi(\boldsymbol{\theta})$, then this objective function will depend on the data, that is the measured values \mathbf{W} . Thus we may indicate that dependence by writing $\Phi_N(\boldsymbol{\theta}, \mathbf{W}^N)$ (where N is the number of electrodes), or simply $\Phi(\boldsymbol{\theta}, \mathbf{W})$ and at the minimum will be,

$$\partial\Phi(\boldsymbol{\theta}^*, W)/\partial\boldsymbol{\theta} = 0 \quad (3.55)$$

where $\boldsymbol{\theta}^*$ corresponds to the minimum of $\Phi(\boldsymbol{\theta}^*, W)$. If we now slightly vary the data replacing W by $W + \delta W$, this would cause the minimum to shift from $\boldsymbol{\theta}^*$ to $\boldsymbol{\theta}^* + \delta\boldsymbol{\theta}^*$, where we must have

$$\partial\Phi(\boldsymbol{\theta}^* + \delta\boldsymbol{\theta}^*, W + \delta W)/\partial\boldsymbol{\theta} = 0 \quad (3.56)$$

Expanding now eq (3.55) in Taylor series and keeping only the terms up to first order, then after we subtract eq (3.56), we obtain

$$(\delta^2\Phi/\delta\boldsymbol{\theta}^2)\delta\boldsymbol{\theta}^* + (\partial^2\Phi/\partial\boldsymbol{\theta}\partial\mathbf{W})\delta\mathbf{W} \approx 0 \quad (3.57)$$

so, we may approximately write

$$\delta\boldsymbol{\theta}^* \approx -\mathbf{H}^{*-1}(\partial^2\Phi/\partial\boldsymbol{\theta}\partial\mathbf{W})\delta\mathbf{W} \quad (3.58)$$

where, $\mathbf{H}^* = (\partial^2 \Phi / \partial \boldsymbol{\theta}^2)_{\boldsymbol{\theta}=\boldsymbol{\theta}^*}$. The covariance matrix is given by

$$Cov \hat{\boldsymbol{\theta}}_N \equiv E(\delta \boldsymbol{\theta}^* \delta \boldsymbol{\theta}^{*T}) \quad (3.59)$$

where the superscript T denotes transposition, so that

$$Cov \hat{\boldsymbol{\theta}}_N \approx E(\mathbf{H}^{*-1} (\partial^2 \Phi / \partial \boldsymbol{\theta} \partial \mathbf{W}) \delta \mathbf{W} \delta \mathbf{W}^T (\partial^2 \Phi / \partial \boldsymbol{\theta} \partial \mathbf{W})^T \mathbf{H}^{*-1}) \quad (3.60)$$

or

$$Cov \hat{\boldsymbol{\theta}}_N \approx \mathbf{H}^{*-1} (\partial^2 \Phi / \partial \boldsymbol{\theta} \partial \mathbf{W}) \mathbf{V}_W (\partial^2 \Phi / \partial \boldsymbol{\theta} \partial \mathbf{W})^T \mathbf{H}^{*-1} \quad (3.61)$$

where, \mathbf{V}_W is the covariance matrix of the data, i.e. $\mathbf{V}_W \equiv E(\delta \mathbf{W} \delta \mathbf{W}^T)$. In eq (3.61) the expressions \mathbf{H}^* and $\partial^2 \Phi / \partial \boldsymbol{\theta} \partial \mathbf{W}$ are evaluated at $\boldsymbol{\theta} = \boldsymbol{\theta}^*$, so they can be taken out of the expectation. If \mathbf{W}_m represents the results of the m_{th} experiment, with covariance matrix \mathbf{V}_m and is independent of \mathbf{W}_n ($n \neq m$), then eq (3.61) reduces to

$$Cov \hat{\boldsymbol{\theta}}_N \approx \mathbf{H}^{*-1} \left[\sum_{m=1}^n (\partial^2 \Phi / \partial \boldsymbol{\theta} \partial \mathbf{W}_m) \mathbf{V}_m (\partial^2 \Phi / \partial \boldsymbol{\theta} \partial \mathbf{W}_m)^T \right] \mathbf{H}^{*-1} \quad (3.62)$$

Equation (3.62) applies to any objective function, whether or not it has a basis in statistics [4]. Here we are going to make a change in notation to substitute the vector \mathbf{W} with the measured potentials $\boldsymbol{\phi}_m$. If we now suppose that our estimate

$$\hat{\boldsymbol{\theta}} = \arg \min_{\boldsymbol{\theta}} \Phi(\boldsymbol{\theta}) \quad (3.63)$$

is the unconstrained minimum of some objective function

$$\Phi(\boldsymbol{\theta}, \boldsymbol{\phi}_m) = \frac{1}{N} \sum_{i=1}^N \frac{1}{2} [\varepsilon^i(\boldsymbol{\phi}_m^i, \boldsymbol{\theta})]^2 \quad (3.64)$$

where, N is the number of the measurement points, $\varepsilon^i(\boldsymbol{\phi}_m^i, \boldsymbol{\theta}) = \boldsymbol{\phi}_m^i - \boldsymbol{\phi}^i(\boldsymbol{\theta})$.

We note that this objective function depends on the data (as we described in the beginning of the paragraph), and in particular depends on the measured values $\boldsymbol{\phi}_m$ of the random variables. Then the covariance matrix of the predicted vector parameters, with $\boldsymbol{\theta}^*$ approximated by $\hat{\boldsymbol{\theta}}$, will be given by [45]

$$Cov \hat{\boldsymbol{\theta}}_N = \frac{1}{N} \left[\frac{1}{N} \sum_{i=1}^N [\varepsilon^i(\boldsymbol{\phi}_m, \hat{\boldsymbol{\theta}})]^2 \right] \left[\frac{1}{N} \sum_{i=1}^N \psi(i, \hat{\boldsymbol{\theta}}) \psi^T(i, \hat{\boldsymbol{\theta}}) \right]^{-1} \quad (3.65)$$

and,

$$\begin{aligned}
\psi(i, \hat{\boldsymbol{\theta}}) &= \frac{\partial}{\partial \hat{\boldsymbol{\theta}}} \varepsilon^i(\phi_m^i, \hat{\boldsymbol{\theta}}) \\
&= \frac{\partial}{\partial \hat{\boldsymbol{\theta}}} [\phi_m^i - \phi^i(\hat{\boldsymbol{\theta}})] \\
&= -\frac{\partial}{\partial \hat{\boldsymbol{\theta}}} \phi^i(\hat{\boldsymbol{\theta}})
\end{aligned} \tag{3.66}$$

where the diagonal elements will give the variance of each of the parameters. If we now choose the objective function to be

$$\Phi(\boldsymbol{\theta}, \phi_m) = \frac{1}{N} \sum_{i=1}^N \frac{1}{2} \left[\frac{\varepsilon(\phi_m^i, \boldsymbol{\theta})}{\sigma_i} \right]^2 \tag{3.67}$$

then the covariance matrix of the estimated parameters will be given by use of eq 3.65 where we substitute the ratio $\varepsilon^i(\phi_m, \hat{\boldsymbol{\theta}})$ by $\varepsilon^i(\phi_m, \hat{\boldsymbol{\theta}})/\sigma_i$ as,

$$Cov \hat{\boldsymbol{\theta}}_N = \frac{1}{N} \left[\frac{1}{N} \sum_{i=1}^N \frac{\psi(i, \hat{\boldsymbol{\theta}}) \psi^T(i, \hat{\boldsymbol{\theta}})}{\sigma_i^2} \right]^{-1} \tag{3.68}$$

where the potential $\phi(\hat{\boldsymbol{\theta}})$ will be given by eq (3.36), and $\psi(i, \hat{\boldsymbol{\theta}})$ is again given by equation (3.66). It should be noted that another property of $\hat{\boldsymbol{\theta}}$ is that it is asymptotically normally distributed. This allows us to compute the 95% confidence interval of each parameter j as $ci_{95\%}^j = 1.96 * \sigma_j$ where, $\sigma_j = \sqrt{var(\hat{\theta}_j)}$. Thus, with 95% probability, the predicted value will be lying within $1.96 * \sigma_j$ from the true solution. Alternatively, if we repeat an experiment hundred times, then each replication would yield a separate estimate θ_j^* ; then the true value would be obtained in an interval of the form

$$\theta_j^* - 1.96 * \sigma_j \leq \hat{\theta}_j \leq \theta_j^* + 1.96 * \sigma_j \tag{3.69}$$

in about ninety five of these intervals.

Subsequently, we may form an overall confidence interval by combining the confidence intervals of individual estimated parameters. Here, since we are interested in

the uncertainty or the prediction error only of the spatial parameters of the dipole, we include only those

$$ci_{95\%} = \sqrt{\frac{1}{3} \sum_{i=1}^3 (ci_{95\%}^i)^2} \quad (3.70)$$

in the overall confidence interval estimate.

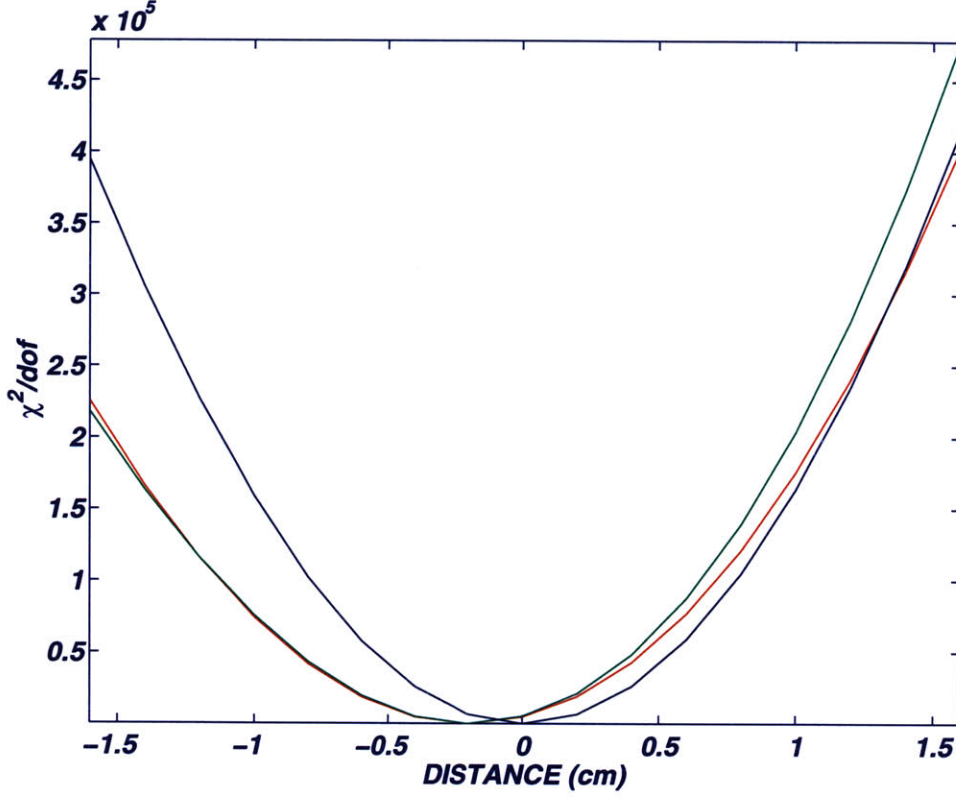
3.10 An Estimate of the Dipole Spatial Uncertainty Using Characteristics of the χ^2/dof

In Figure 5-11, we look into the changes of the χ^2/dof space around the best solution. We calculated the χ^2/dof along the major axis (x,y,z) and around the best solution in a series of points starting from a negative value and extending to the same positive value on the positive axis (i.e [-1.6,1.6]), when the origin coincides with the best solution. We found that the χ^2/dof increases monotonically away from the best solution.

The observation that χ^2 appears to be monotonic around the best solution or the minimum χ^2 value, allows us to compute a distance away from the best solution that χ^2 will change by a known percentage. We may for example estimate the distance along each of the major axis (in both negative and positive directions) from the best solution that would cause the χ^2 to change (here increase) by 95%.

However, the χ^2 asymptotically approximates a normal distribution ($\mu = \text{dof}$, $\sigma^2 = 2 * \text{dof}$) for a large number of dof, and since throughout this study the dof is $\cong 50$, it is valid to consider here the χ^2 distribution to be normal. Since, the χ^2 distribution is defined only for positive values we can shift it to the origin and take the 95% confidence half interval to be $\chi_{.975}^2 - \chi_{.50}^2$ for the specific dof.

Figure 3-5 Distribution of χ^2/dof values along each of the major orthogonal axes (i.e $-x \rightarrow +x$) and around the optimal solution.



Here, the number of dof = 54 and the 95% confidence interval will be given by [65]

$$ci_{(\chi^2)_{95\%}} = (\chi^2)_{0.975|_{dof=54}} - (\chi^2)_{0.50|_{dof=54}} \quad (3.71)$$

$$= 76.172 - 53.33 \quad (3.72)$$

$$= 22.842$$

So, if we originate at the best solution a search along the major axis (i.e. from zero to \pm x-axis) until a 95% χ^2 confidence interval is achieved, we obtain six lengths (confidence intervals) that can be combined in the form

$$ci_{(\chi^2)_{95\%}} = \sqrt{\frac{1}{6} \sum_{i=1}^6 (ci_{(\chi^2)_{95\%}}^i)^2} \quad (3.74)$$

Alternatively, the uncertainty in each of the major axis is obtained from the two confidence intervals (for the positive/negative directions) from eq (3.75)

$$\sigma_i = \frac{1}{1.96} \sqrt{\frac{1}{2} \left[(ci_{(\chi^2)_{95\%}}^{-i})^2 + (ci_{(\chi^2)_{95\%}}^{+i})^2 \right]} \quad (3.75)$$

3.11 The Accuracy of the Optimization Algorithm in Computer Simulations

In this section, we calculated the ability of the prediction error and the spatial variation of χ^2 to predict the uncertainty in the estimate of dipole location as obtained from multiple parallel simulation. For this comparison we wanted to evaluate only the random component of the error in dipole location, thus we used the simulations described earlier in which the dipole location and orientation were fixed, and only noise realization varied from run to run. In Table 3.3 we compare the standard deviation of location computed from the prediction error theory (eq (3.68)), and the spatial variation of χ^2 applied to the results of the first of 100 simulations, with the standard deviation of location estimated from the distribution of dipole location estimations obtained from the 100 simulations with different realizations of the noise.

In this analysis we employed two models (i) an unbounded infinite homogeneous volume conductor (eq (3.36)), and (ii) the bounded sphere model (eq (3.37)).

We see that the prediction error and the spatial variation of χ^2 led to similar estimates of the standard deviation which although small in absolute terms, were significantly greater than the standard deviation measured directly from the distribution resulting from different noise realizations.

Table 3.3: The dipole spatial uncertainty for measurement noise magnitude of $\sigma_n = 0.01 \text{ mV}$ in a computer simulation unbounded model (upper table) and in a bounded spherical model (lower table).

INTERVENTION	$\sigma_x \text{ (cm)}$	$\sigma_y \text{ (cm)}$	$\sigma_z \text{ (cm)}$	$\sigma \text{ (cm)}$
Noise Realizations	0.0027	0.0038	0.0029	0.0055
Prediction Error	0.0114	0.0130	0.0095	0.0114
Spatial Variation in χ^2	0.0156	0.0149	0.0142	0.0149

INTERVENTION	$\sigma_x \text{ (cm)}$	$\sigma_y \text{ (cm)}$	$\sigma_z \text{ (cm)}$	$\sigma \text{ (cm)}$
Noise Realizations	0.0009	0.0011	0.0013	0.0019
Prediction Error	0.0115	0.0133	0.0097	0.0116
Spatial Variation in χ^2	0.0058	0.0055	0.0052	0.0095

3.12 Discussion

In this chapter we used computer simulations to evaluate different optimization methods for identifying the dipole parameters from surface potential measurements. The first set of simulations involved use of an unbounded model in which we randomized the dipole location and orientation, and added different realizations of the measurement noise. We found that the 3 *plus* 3 parameter outperformed the 6 parameter method, and that the Simplex method outperformed the Davison-Fletcher-Powell (DFP), Fletcher-Reeves-Polak-Ribiere methods (FRPR).

We next compared the use of different objective functions, the χ^2/dof , the root-normalized-mean-square-error (RNMSE) and root-double-normalized-mean-square-error (RDNMSE). The latter two objective functions were developed to improve the performance of our inverse algorithm in the presence of systematic error (resulting for example from boundary effects and/or inhomogeneities in tissue conductivity). To evaluate these functions we used both an unbounded volume conductor and a

bounded spherical model, in which the magnitude of the noise varied from electrode to electrode. The bounded spherical model included boundary effects not included in the model used by the inverse algorithm. In these simulations we randomized the dipole location, orientation, and used different noise realizations. We found that the χ^2/dof method still had overall best performance for both the unbounded and bounded models. We note however, that the χ^2/dof should be used with caution in realistic experiments because of the difficulty in estimating the measurement noise in each electrode. These considerations would probably mostly affect the absolute numerical value of chi-square obtained experimentally more than the ability of χ^2/dof as an objective function to guide the inverse algorithm to best estimate of the inverse solution.

Randomization of dipole location and orientation in the above simulations involving the bounded spherical model, led to an increase in the uncertainty of the localization because a different systematic error was introduced with each simulation. The systematic error in the bounded spherical model is due to boundary effects which are not accounted for in the ideal model used in the inverse algorithm.

In experimental conditions, systematic error may result from imprecise knowledge of the location of the electrodes, non-detailed torso geometry, inhomogeneities in tissue conductivity, as well as boundary effects. In the ultimate application of this technology, systematic error is not as important as random error, because it will only be necessary to superimpose the dipole associated with the site of initiation of an arrhythmia and the dipole created with passing current through a bipolar electrode located on the tip of an ablation catheter. Thus systematic errors associated with the estimation of the dipole location will cancel. However, random error is important because this will limit the ability to superpose these two dipoles.

To determine the random component in the uncertainty in the spatial dipole parameters, we ran simulations for unbounded and bounded models in which the

Table 3.4: The uncertainty due to noise realizations (upper table) and random dipole orientation as well as noise realizations (lower table).

σ_n (mV)	σ (cm)	
	Unbounded	Bounded
0.001	0.00002 \pm 0.0005	0.64341 \pm 0.0003
0.01	0.00032 \pm 0.0051	0.64338 \pm 0.0017
0.1	0.00333 \pm 0.0507	0.64372 \pm 0.0184
1.0	0.03002 \pm 0.4852	0.64630 \pm 0.1867

σ_n (mV)	σ (cm)	
	Unbounded	Bounded
0.001	0.00011 \pm 0.0006	0.62829 \pm 0.0437
0.01	0.00103 \pm 0.0055	0.62779 \pm 0.0429
0.1	0.00737 \pm 0.0535	0.62761 \pm 0.0500
1.0	0.11516 \pm 0.5677	0.60711 \pm 0.1965

dipole location and orientation were fixed and we only added different realizations of the measurement noise. The uncertainties in position in these cases were similar to those in the case of the unbounded model in which dipole location and orientation were randomized. This is as expected, because in the case of the unbounded model no systematic errors should be introduced (the results are summarized in Table 3.4).

We also examined the effect of randomizing the dipole orientation while holding the dipole location fixed and while adding different realizations of the measurement noise. The purpose of this simulation was to determine whether a significant error would be introduced when attempting to superpose the catheter tip dipole with the dipole of the arrhythmia initiation site, when the two dipoles have different orientation (if necessary by using a multiple electrode catheter, one could create parallel dipoles). However, in these simulations the effect of dipole orientation was small even in the

case of the bounded spherical model.

In the remaining of this thesis we will be using the χ^2/dof as the objective function, and also the 3 *plus* 3 optimization approach and the Simplex method to obtain the dipole parameter estimates.



Lesvos Island - Eressos (Edition: A&E Moliviatis)

Chapter 4

Computer Simulations on A Distributed Source Model

4.1 Motivation

Although the idea of using the single equivalent dipole (SEMD) model to characterize the cardiac electrical sources from body surface electrocardiographic (ECG) recordings is an appealing one, in reality cardiac electrical activity is spatially distributed in three dimensions and evolves with time. However, for many arrhythmias the electrical activity within the heart is highly localized for a portion of the cardiac cycle. During the remainder of the cardiac cycle the electrical activity may become more diffuse as the waves of electrical activity spread.

Furthermore, the limited spatial sampling (restricted by the number of the electrodes placed on the body), as well as the spatial smearing and distortions caused by the inhomogeneous volume conductor, significantly reduce our ability to non-invasively localize cardiac electrical events (i.e. arrhythmogenic foci and reentrant pathways inside the heart).

In this chapter we employ a computer simulation model that represents a dis-

tributed source, to investigate the intrinsic limitations associated with representing cardiac electrical with a SEMD throughout the cardiac cycle. We also studied the effects of electrode location, wave-front size, measurement noise (one source of error), and signal to noise ratio (SNR) in resolving accurately the SEMD parameters, from potentials generated by a distributed source model.

We have also investigated the temporal applicability of the SEMD model during the cardiac cycle by understanding when and where cardiac activation is highly localized.

4.2 Model description

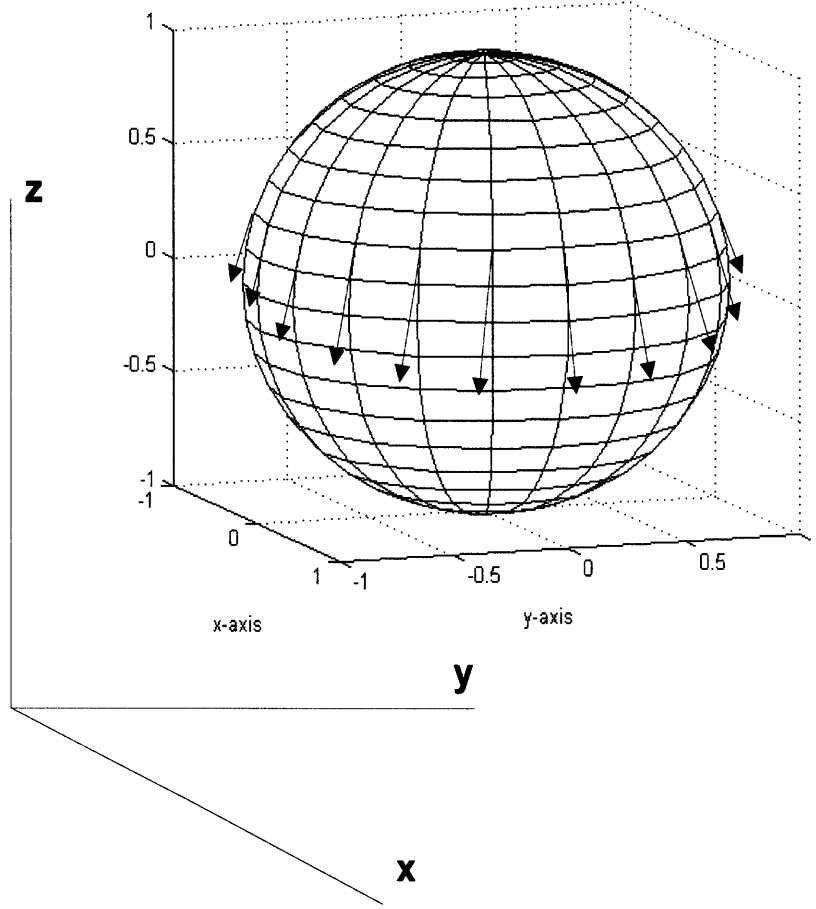
Our aim was to show in computer simulations model the intrinsic limitations associated with the use of a SEMD to localize cardiac electrical sources. If the assumption of the dipolar nature of cardiac excitation is valid we were also probing the temporal and spatial course of its applicability with the intention of deciding when and where cardiac activation is highly localized.

We thus introduced a distributed source model to investigate the dipolar nature of a wave of depolarization spreading from a focal source over the surface of a spherical shell (of radius r_{sh}).

We assumed a wavefront tangent to the surface of the heart (which we assume to be the sphere shown in Figure 4-1) that propagated from north to south pole. We assumed a constant dipole-moment density P_i , $i = 1, 2, \dots, n$ at each belt resulting by taking two slices of the heart sphere at specified z – *levels*, and a number of dipoles (that represented the distributed source) were located at equal arc-lengths on the circumference of the belt, and which accounted for the overall dipole moment density of the belt

$$\frac{P_1}{2\pi R_1} = \frac{P_2}{2\pi R_2} = \dots = \frac{P_n}{2\pi R_n} \quad (4.1)$$

Figure 4-1 Representation of the distributed source model.



where, P_j and r_j are the scalar total moment and the radius of the j_{th} respectively.

In other words if such N dipoles made for the wavefront in each belt, then N remained constant for all belts and dipole-moment density at step N was given by

$$P_n = \frac{R_n}{R_1} P_1 \quad (4.2)$$

4.3 Results

Using this distributed source model we tried to examine the intrinsic limitations associated with representing the cardiac activation as an equivalent moving dipole.

The inverse algorithm employed here used a multi-seed (ten) iteration to find two solutions that were located inside the sphere, and were less than 0.5 cm apart. Then the minimum error solution from the two was chosen (for more information the reader may consult Figure 3-2, where the same algorithm is applied with the addition that the solution obtained at each stage (θ angle), here served as the initial seed in the next stage).

In Figure 4-2 we plotted the error

$$Error = \sum_{i=1}^I (\phi^i - \phi_m^i)^2 \quad (4.3)$$

and the root mean normalized square error (RNMSE)

$$RNMSE = \sqrt{\frac{\sum_{i=1}^I (\phi^i - \phi_m^i)^2}{\sum_{i=1}^I (\phi_m^i)^2}} \quad (4.4)$$

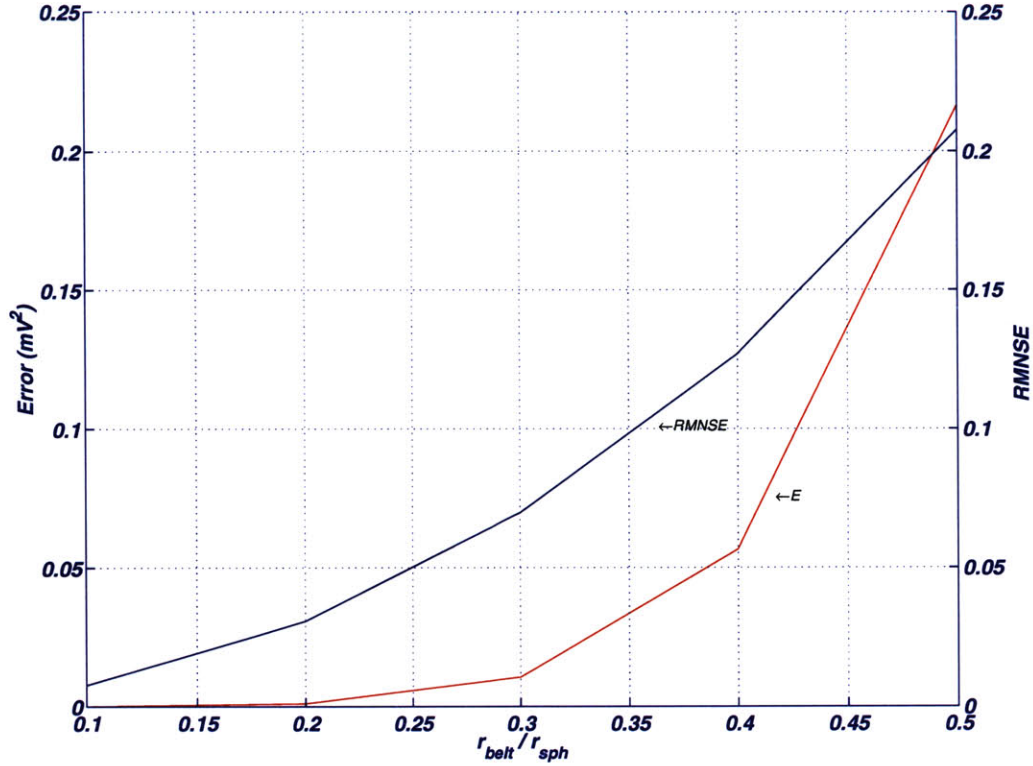
as a function of r_{belt}/r_{sph} (for belts centered at the origin) for the ideal case of no-noise. We saw that as the belt radius became larger both the error and RNMSE increase monotonically. Due to cylindrical symmetry the solution's coordinates are at the geometrical center of the belt (the origin). The increase of the error function with r_{belt} reflects the increasing distributedness (non-dipolar nature of the source).

Then, we allowed the depolarization wavefront to propagate from the bottom of the heart ($\theta = 0^\circ$, north pole) to the apex ($\theta = 180^\circ$, south pole), thus obtaining a sequence of activation fronts (belts) in planes perpendicular to the z-axis. At each z-level we either compute the contribution to the potential from each dipole at the circumference of the belt (distributed source model) or the potential due to a dipole that is moving from north to south pole and its magnitude is equal to the dipole-moment density at the specified z-level (focal source model). In either case we compute the $\delta P/P$ and $\delta r/r$, where

$$\frac{|\delta P|}{|P|} = \frac{\sqrt{(P_x^f - P_x^i)^2 + (P_y^f - P_y^i)^2 + (P_z^f - P_z^i)^2}}{\sqrt{(P_x^f)^2 + (P_y^f)^2 + (P_z^f)^2}} \quad (4.5)$$

$$|\delta r| = \sqrt{(r_x^f - r_x^i)^2 + (r_y^f - r_y^i)^2 + (r_z^f - r_z^i)^2} \quad (4.6)$$

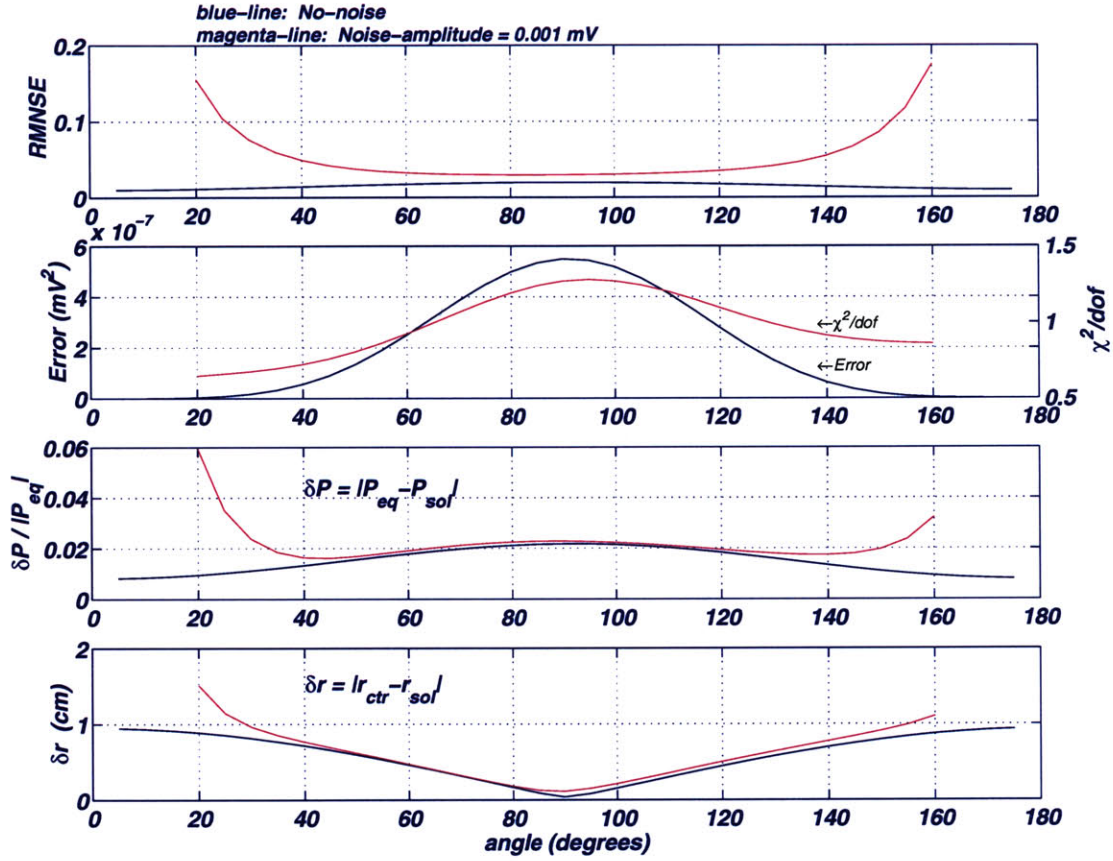
Figure 4-2 The error and Root Mean Normalized Square Error (RNMSE) as a function of z_{belt}/r_{sph} .



where, f and i stand for the forward and inverse values respectively. The forward moment components for the distributed source model are equal to the components (P_x, P_y, P_z) of an equivalent dipole resulting from the sum of the projections of each of the individual dipole components on the circumference of the belt. Similarly, the forward equivalent dipole location for the distributed source model is equal to the components (x_d, y_d, z_d) of an equivalent dipole resulting from the sum of the projections of the coordinates of each of the individual dipole components (that make the distributed source on the circumference of the belt). The inverse equivalent dipole moments and location are provided by the optimization scheme applied. In Figure 4-3, we provide two types of plots, each corresponding to a different noise implementation: (i) a no-noise approach and (ii) a noise ($\sigma = 0.001 \text{ mV}$) approach. Noise amplitude

was chosen such that it would have comparable size to the size of the potentials that

Figure 4-3 The Root Mean Normalized Square Error (RNMSE), Error, χ^2/dof , $\delta P/P_{eq}$, δr as a function of the angle that the wavefront forms with the z-axis.



the distributed source would generate at the poles. So, we plot the RNMSE, error and χ^2/dof (3.38), $|\delta P| / |P_{eq}|$ and δr as a function of the angle θ (where, $\cos(\theta) = z_{belt}/r_{sh}$) that the wavefront forms with the z-axis (θ extends from 5 to 175 degrees).

We firstly observe that in the presence of noise the inverse algorithm for the equivalent dipole location fails to converge for small dipole sources (those at small and large angles in Figure 4-3), where the potentials (from the forward problem) are comparable in magnitude to the simulated noise. The above implies that an inverse solution can only detect a distributed source if it has a sufficient size (length of

excitation front), which means that the equivalent dipole location obtained from the algorithm will generally differ from the geometrical center of the source distribution.

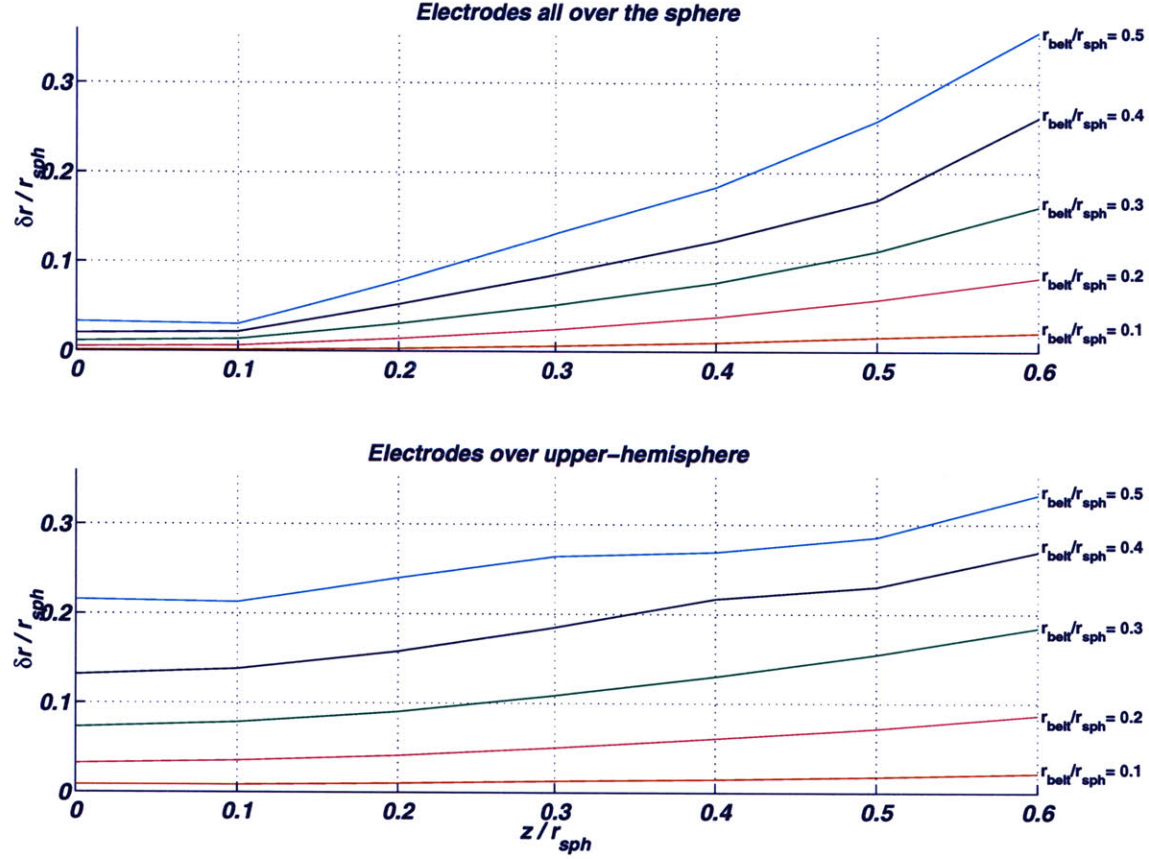
Secondly, the RNMSE becomes larger in the simulation that noise was used at small or large θ angles, that is when the size of the source becomes smaller (and mostly represents a dipole), and the amplitude of the measured potentials is comparable to the amplitude of the measurement noise. The last statement can be shown to be correct in Figure 4-2 where a smaller belt size, in a no-noise case, provided smaller RNMSE.

Thirdly, we observe that the $|\delta P| / |P_{eq}|$ for very small (and large angles) is larger, then reaches a minimum for $\theta \approx 45^\circ$ and slightly increases again. For small angles $|\delta P| / |P_{eq}|$ is large because of the low signal-to-noise ratio; while at 90° the $|\delta P| / |P_{eq}|$ is large because of the proximity of the dipole moment components of the distributed source to the surface of the sphere electrodes; and finally in the middle of these two above mentioned cases $|\delta P| / |P_{eq}|$ takes its minimum value. The situation is much simpler in the no-noise case where we see only the effect of the proximity of the dipole moment components to the surface electrodes.

Fourthly, the δr becomes smaller when the size of the distributed source, and the signal-to-noise ratio, get their largest value. We observe that δr of the equivalent dipole at the poles (where the source is mostly dipolar) is larger than the equator. This can be explained by the low signal-to-noise ratio. Conversely, in the no-noise case the δr becomes minimum at 90° when the potentials get their largest value. That is contrary to what someone would expect given that the distributed source is mostly dipolar at the poles. However, in Figure 4-4 we see that even for an off-center belt the $\delta r/r_{sph}$ became larger the larger the break of symmetry became.

In Figure 4-4 we plot the $\delta r/r_{sph}$ as a function of z/r_{rsph} for different r_{belt}/r_{sph} and for electrodes placed all over the sphere (upper panel) and the upper hemisphere (lower panel). We firstly observe that the position of the electrodes is a significant

Figure 4-4 The $\delta r/r_{sph}$ is plotted as a function of z/r_{sph} for different r_{belt}/r_{sph} and for electrodes placed all over the sphere (upper panel) and the upper hemisphere (lower panel).



contributing factor to the localization of the equivalent dipole. Uniform distribution of the electrodes that provides a global view of the source seems to be the best option in reducing the spatial error in the distributedness of a source.

Secondly, we observed that the spatial error increased with the extent that the distributed source was off-center (z/r_{sph}) and also with the size of the distributed source (r_{belt}/r_{sph}).

4.4 Discussion and Conclusions

To date, there have been numerous attempts to develop advanced and detailed models for the analysis of electrocardiographic (ECG) signals, yet the most common model for practical applications is still the equivalent current dipole. This model provides useful information even in situations where the underlying assumption may be heavily violated. Such might be the case if the source is not confined to a circumscribed area and its structure is much more complex than can be described by an equivalent dipole. In this case it is often justified to assume the equivalent dipole location as the center of the source and to consider the amplitude of the moment as a measure of the mean activity of the source. The equivalent dipole plays this special role because it is the leading term of a multipole expansion.

Study of the distributed source model showed that the χ^2/dof and RNMSE became larger as the size of the distributed source increased. At very small and large angles the algorithm (in the case of added noise) failed to converge as a result of the small dipole moment that gave rise to potentials (in the forward problem) that were of comparable magnitude with the simulated noise magnitude. We thus observe the seeming paradox that it is most likely to find a dipole when the source is less dipolar and this is because while the moment density remained constant (wavefront), the wavefront length (or length of the active tissue) became bigger, which results in a bigger source and a bigger SNR. But bigger source did not mean that it was a dipole any more.

The conclusions of this computer simulation investigation were that: (i) the location of the equivalent dipole we obtained is generally different from the geometrical center of the distributed source, (ii) the trajectory of the equivalent dipole will depend on the location of the source relative to the position of the electrodes, (iii) the best localization of the equivalent dipole is achieved when the source is smallest but due to the small signal to noise ratio, we can only find sources that are larger than a

certain size, (iv) the above represent intrinsic limitations associated with identifying equivalent dipole sources when the actual sources are rather distributed.



Lesvos Island - Sigri (Edition: A&E Moliviatis)

Chapter 5

Evaluation of the Algorithm to Identify the SEMD in Real ECG Signals

5.1 Motivation

In this chapter we investigate and evaluate the applicability of our inverse algorithm to identify the single equivalent moving dipole (SEMD) from body surface electrocardiographic (ECG) recordings, presented in chapter 3.

Body surface ECG signals were obtained from a swine animal model during pacing from an epicardial sock electrode array that was surgically placed around the animal's heart.

The key issue addressed in this chapter relates to the fundamental question raised throughout this thesis: what is the resolution of our inverse algorithm in localizing electrical events in the heart, from body surface ECG signals.

5.2 Experimental Protocol

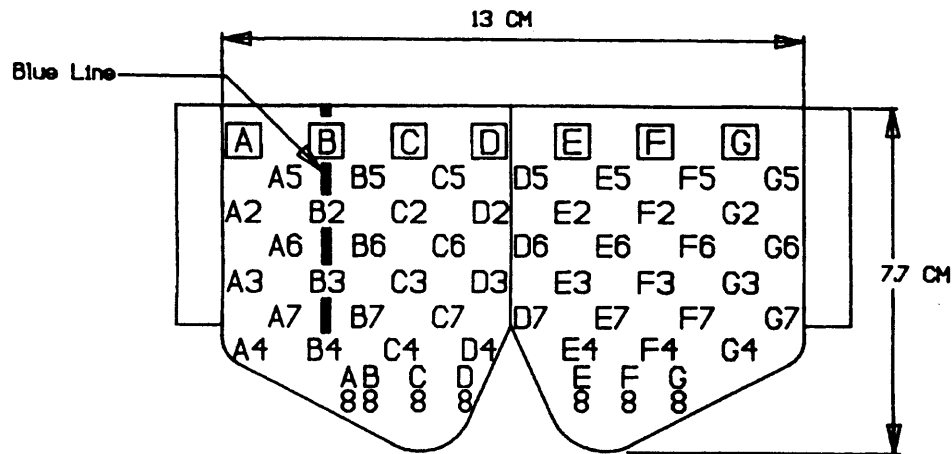
The experimental protocol was approved by the MIT Committee on Animal Care. Five female Yorkshire pigs weighing 18 to 20 kg were studied. This population was sufficient to study the feasibility and validity of a proposed algorithm to identify and characterize cardiac electrical sources from body surface ECG signals. This species was selected because: (i) the pig heart is sufficiently large to allow for cardiac instrumentation of the ventricles, (ii) the pig heart is reasonably large to allow the study of the applicability of our inverse algorithm on a scale comparable with the human, and (iii) the pig provides a desirable model for cardiovascular disease because the coronary collateral circulation is similar to that in humans [15].

The animals were tranquillized with sodium xylazine (0.2 mg/kg IM) and ketamine (2 mg/kg IM) and anesthetized with sodium pentobarbital (20 mg/kg IV). The animals were then intubated, artificially ventilated and were provided with supplemental oxygen. Catheters were placed in the jugular vein for drug delivery and in the aorta via the common carotid artery for monitoring blood pressure.

Blood pressure and ECG were monitored throughout the study to insure the hemodynamic stability of the animals. A sternotomy was performed and a 56-electrode epicardial sock (Bard Electrophysiology, Billerica, MA, USA) was placed around the heart and aligned relative to the left ascending coronary artery (Figure 5-1 [29, 94]). Sock dimensions were 13 cm around the perimeter of the opening, and 7.7cm in length. The leads that constituted the bipolar electrodes of the sock were 3mm apart. A blue colored line on the sock served as a reference to the sock's anatomical position with respect to the heart. The blue line was aligned with the left ascending coronary artery of the heart. The sternotomy was closed in layers, and the pneumothorax was evacuated. The skin was cleaned with alcohol and was mildly abraded.

Heart rate, blood pressure, and core temperature were monitored during the experiment to assure hemodynamic stability of the animals. At the conclusion of the

Figure 5-1 Diagram of electrode position on the sock.



experiment, the animals were euthanized with injection of sodium pentobarbital (100 mg/kg IV).

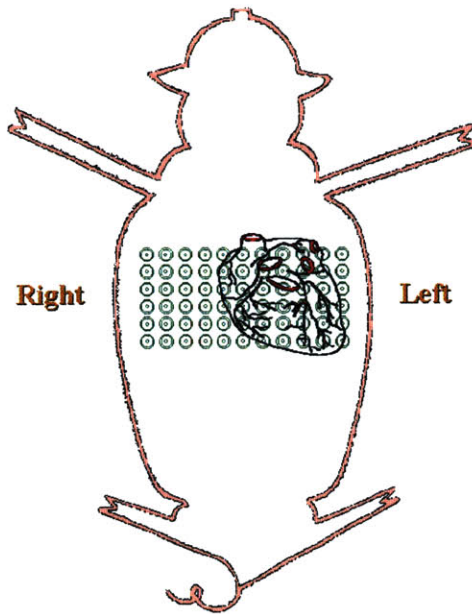
Signal quality was also monitored in real time during the experiments.

5.3 Data Acquisition and Processing

An inflatable electrode cuff with 60 electrodes in a ten by six array, with a 2.5 cm center-to-center electrode spacing, was fitted around of the animal such that the electrodes were located in the left half of the body (Figure 5-2). Each electrode consisted of a conductive AgCl disk of 8mm diameter. The unipolar ECG signals were measured with respect to a common reference point, the Wilson's central terminal. Data were recorded from the limb leads.

The cuff was inflated during periods of data acquisition to improve electrode to skin contact. The unipolar body surface potentials were measured in reference to Wilson's central terminal. The leads from each electrode were connected to a multi-channel bio-electrical mapping system [30,32] that was designed to provide continuous

Figure 5-2 Configuration of the body surface electrodes [33].



recording with adjustable gain and frequency response. After amplification, signals were filtered by a programmable band pass filter (0.05 to 1.4 KHz). The signals then were entered to a Masscomp Concurrent Computer (Westford, MA) via a 12 bit analog to digital converter.

Immediately after the closure of the sternotomy, baseline recordings were recorded during the sinus rhythm, during pacing at 150 and 170 beats/min. Pacing stimuli were delivered at a current that assured capturing of the intrinsic heart rhythm (Medtronic programmable stimulator, Model 7350). The stimulator was battery powered so as to minimize electrical interference with the multichannel recording system. Data segments of 5 to 10 sec in length were recorded that typically contained a minimum of 5 to 30 beats in each segment. The cardiac electrical signals were amplified and band-pass filtered between 1 and 175 Hz using a custom built bio-electrical amplifier. The signals were digitized at 500 Hz and analyzed off-line using custom built software.

5.4 The ECG Analysis Process

The steps followed in data analysis are presented in Figure 5-4, where S stands for step. Following data collection (S1), each of the body surface ECG channels (60) was visually inspected to secure good data quality (S2).

Inadmissible data could occur from (i) insufficient capturing from epicardial pacing, (ii) not good contact of the electrodes to the skin, (iii) electrode failure during the experiment.

Then the R wave in the QRS complex was identified in each ECG beat and for each channel and subsequently the baseline of each beat was adjusted relative to a manually identified PR segment (S3).

We first identified ECG complexes, then determined fiducial points by a template-matching based QRS detection algorithm. The resulting annotations and RR intervals were graphically examined for evidence of spurious and/or undetected events. The annotation file was left intact and indicated locations of normal as well as abnormal QRS complexes (premature ventricular depolarizations, supraventricular beats, aberrantly conducted sinus beats). After this initial phase, an iterative, adaptive template matching scheme was used to refine initial fiducial point estimates (S4). For this refinement phase the vector magnitude waveform of the QRS complex from standard ECG leads (I,II,III) was calculated for each beat. This was done by calculating the square root of the sum of the squares of each of the three baseline-corrected orthogonal leads. Baseline correction included estimation of the baseline in the isoelectric PQ segment by averaging successive samples in this time window for each lead and subsequently subtracting this estimate before construction of the vector magnitude. The average vector magnitude QRS complex was then calculated with the use of initial fiducial point estimates. With this average as a template, the fiducial points corresponding to each QRS complex were then shifted to maximize the cross-correlation between each beat and the template [75].

Next, a median beat (S5) was then created to represent each data segment by aligning each beat within the data segment according to the R wave (Figure 5-5). and identifying the median value on a point-by-point basis within the beat. Alternatively, in this step we have developed an algorithm able to perform beat-to-beat analysis (continuous analysis) across all channels. This algorithm has the ability to select a baseline segment before each QRS complex for individual beat noise estimation. Since, for each sample-point (time instant), the algorithm obtains N solutions that correspond to the best solutions of the same sample-point for the N beats, the selection of the solution with the minimum RNMSE was chosen to be the best solution for that sample-point (as an alternative choice, the solution with the median RNMSE value can be selected).

After estimation of the median beat for each channel, a noise estimate was obtained (S6) from each median beat (and channel) in a predefined noise window (Figure 5-5).

Having completed the pre-processing of the data, in the next step our algorithms can be applied. We then apply the inverse algorithm (S7), trying to fit the ECG potentials (60), using the single equivalent moving dipole (SEMD) model, for every instant (sample point) in the cardiac cycle (Figure 5-6). The inverse algorithm was the same with that presented in Figure reffig:algo2, with the exception that when a solution obtained for a point in the cardiac cycle it served as the initial seed for the next point.

Similarly, if after all seed iterations, there were no solutions found that satisfied the spatial criterion and were closer than 0.5 cm , the algorithm was considered non-convergent for the specific instant of the cardiac cycle and was reset to the next sample point.

5.5 On the Resolution of the Inverse Algorithm

In Figure 5-7 we see a schematic of the ventricle and a focal reentry circuit is indicated by the thick arrow. Concentric lines indicating spread of the VT excitation from the focus. The QRS complex is observed after reentry wavefront has propagated out of the circuit depolarizing myocardium further from the VT origin. It becomes apparent that a sizable heart tissue has to become activated before someone is able to “perceive” that a cardiac electrical event has occurred. Thus, a threshold of signal to noise ratio has to be met before the operator is able to “see” the activation focus.

Therefore, in the remaining of this paragraph we will give a simple and approximate estimate of the minimum size activation front that can be detected and attributed to a SEMD (double layer) generator.

If ϕ_i and ϕ_o are the intra-cellular and extracellular potentials respectively, and I_m is the net membrane current per unit volume flowing from the intra-cellular medium to the extracellular medium, then the electrical behavior of the resulting continuous system is described by the following set of equations,

$$\nabla \cdot \sigma_i \nabla \phi_i = I_m \quad (5.1)$$

$$\nabla \cdot \sigma_o \nabla \phi_o = -I_m \quad (5.2)$$

where σ_i/σ_o are the effective conductivities of the intra-cellular and extracellular space respectively. Combining equations 5.1 and 5.2 we obtain

$$\nabla^2 \phi_o = -(\sigma_i/\sigma_o) \nabla^2 \phi_i = \frac{1}{\sigma_o} \nabla \cdot \mathbf{J}_i \quad (5.3)$$

Equation 5.3 has the form of Poisson’s equation and identifies the current dipole moment per unit volume \mathbf{J}_i (as seen by the extracellular medium) as,

$$\mathbf{J}_i = -\sigma_i \nabla \phi_i \quad (5.4)$$

The solution of Poisson's equation can be written as,

$$\phi_o = \left(\frac{1}{\sigma_o} \int_{\Delta V} \mathbf{J}_i dV \right) \cdot \nabla \left(\frac{1}{r} \right) \quad (5.5)$$

where ΔV is the active volume where there is trans-membrane current. From eq. 5.5 we obtain

$$\mathbf{p} = \frac{1}{\sigma_o} \int_{\Delta V} \mathbf{J}_i dV \quad (5.6)$$

since

$$\nabla \left(\frac{1}{r} \right) = \frac{\hat{a}}{r^2} \quad (5.7)$$

where \hat{a} is the unit directional vector.

From equations 5.5 and 5.6, by taking $\nabla \phi_i \cong 180mV/mm$ (Figure 5-8), and $\delta z \cong 0.5mm$, for $\sigma_i/\sigma_o \cong 0.37$ [48] and at a distance $r \cong 10cm$ (distance from the heart to body surface), we obtain that, for potentials just above the noise level, $\cong 10\mu V$, the smallest surface of excitable tissue $\delta x \delta y$, that can be detected at the body surface is $\cong 0.03cm^2$ (a square with sides $\cong 0.6$ cm).

5.6 Temporal Evolution of the SEMD Parameter Estimates During the Cardiac Cycle

In Figure 5-9 we present the temporal evolution of the dipole location and dipole moments during the cardiac cycle. The SEMD parameter estimates of the best solution obtained from the median beat analysis (median beat derived from 17 beats).

Notice that the dipole location and moment vary sharply during the QRS complex and very slowly with reduced amplitude during repolarization.

5.7 Prediction of the ECG Signals From the SEMD Parameter Estimates

The ability of the SEMD model and our inverse algorithm to “explain” and predict the measured data is presented in Figure 5-10. A sequence of ECG beats was split in two halves, from which the first half was used to form a median beat for each channel, in which the algorithm was applied. Then, the SEMD parameter estimates obtained for each instant in the cardiac cycle were used to reconstruct the ECG values shown in Figure 5-10, where the measured (in red) and the predicted ECG signals (in blue), in the form of median beats from nine body surface sites are shown.

In addition, to verify the ability of our algorithm to perform beat-to-beat analysis of the ECG signals is verified by plotting the reconstructed ECG data obtained from the SEMD parameters that correspond to the minimum RNMSE for the specific sample point across beats (green line). We also, give the correlation coefficient (r), between the measured and the predicted signals (across the whole beat) for each of the approaches. The correlation coefficient was obtained by use of

$$r = \frac{Cov(\phi_m^i \phi_p^i)}{\sqrt{Cov(\phi_m^i \phi_m^i) Cov(\phi_p^i \phi_p^i)}} \quad (5.8)$$

where, ϕ_m^i represents measured potentials at lead i , ϕ_p^i represents predicted potentials at lead i and Cov is the covariance matrix. The high correlation coefficient throughout the cardiac cycle (although we are mostly interested for the QRS complex), shows that the SEMD model may be a good representation of cardiac electrical activity even when the assumptions for using this model are highly violated (i.e. during the T-wave cardiac electrical activity is highly distributed and non-localized). The high correlation coefficient between the predicted ECG signals from the continuous analysis and the median ECG signal for each beat, shows that these SEMD parameter estimates are highly reproducible in a beat-to-beat basis.

5.8 Early Activation Analysis in the ECG Signal

The site of earliest activation and the interface between areas with respectively low and high membrane currents are characterized by signals with initial negativity [78]. This signal has a high dV/dt if the recording electrode is positioned close to the current generating tissue. In unipolar ECG signals, the highest negative derivative (dV/dt) of the intrinsic deflection is usually easily recognized and allows accurate determination of local activation times during mapping procedures [22,61,72]. Different algorithms have been used to evaluate the reproducibility of activation detection, that use the maximum negative derivative [5], or the maximum derivative in either direction [64].

In this study we have used a 3-point derivative and the maximum absolute value of the slope given by 5.8 to identify the earliest activation in the surface unipolar ECG signal,

$$\frac{dV(t_i)}{dt} = \frac{V(t_{i+1}) - V(t_{i-1})}{2 * SI} \quad (5.9)$$

where SI is the sampling interval.

5.9 Estimation of the SEMD Spatial Uncertainty

Using Characteristics of the χ^2/dof

In Figure 5-11 we present the spatial variation of χ^2/dof at one point in the cardiac cycle.

We calculated the χ^2/dof along the major axis (x,y,z) and around the best solution in a series points starting from a negative value and extending at to the same positive value on the positive axis (i.e [-2,2]), when the origin coincides with the best solution. We found that the χ^2/dof increases monotonically away from the best solution, while

the largest fluctuation as a function of distance is noticed along the z-axis (that extends along the body).

The observation that χ^2 appears to be monotonic around the best solution or the minimum of χ^2 value, allows us to estimate the uncertainty of the dipole location using the variation of the χ^2 around the best solution according to the method described in section 3.10.

5.10 Measurement Noise Dependent Statistical Properties of the SEMD Parameter Estimates

To estimate the uncertainty in the dipole location due to the measurement noise, we employed the following procedure. We estimated the magnitude in each of the electrodes as described in section 5.4. Then we added a random realization of the noise to the median ECG signal (file 11j94:C6) for each electrode and then obtained the SEMD parameter estimates by applying the algorithm presented in Figure 5-6.

We repeated this procedure 100 times and estimated the variation in the spatial dipole parameter estimates. A distribution for each of the SEMD parameters was obtained for each point throughout the cardiac cycle. The statistical analysis involved the selection of the solution that corresponded to the one- and two-thirds of the distribution of solutions for each of the spatial SEMD parameters. Assuming the estimated parameters follow a gaussian distribution, the standard deviation of each parameter is estimated by the one-third and two-thirds of the values of that distribution.

$$\sigma = \frac{X_{2/3} - X_{1/3}}{0.861} \quad (5.10)$$

In Figure 5-12 we plot the median and one standard deviation of each of the spatial SEMD parameters. We observe that the uncertainty (due to measurement

noise) in the position of the SEMD is small throughout the cardiac cycle, except at the portion of the signal around the pacing spike and after repolarization completion because of the low signal-to-noise ratio. However, it is especially low during the portion of the cardiac cycle that we are mostly interested in; i.e. from the earliest activation time indicated by the first marker in the ECG signal ($\sigma_x = 0.005 \text{ cm}, \sigma_y = 0.006 \text{ cm}, \sigma_z = 0.011 \text{ cm}$), till the minimum value of the RNMSE error indicated by the second marker ($\sigma_x = 0.009 \text{ cm}, \sigma_y = 0.013 \text{ cm}, \sigma_z = 0.031 \text{ cm}$). Thus, estimation the effect of measurement noise on the SEMD parameter estimates indicates that measurement noise should not have a significant effect in the estimation.

We have previously introduced the concept of the prediction error and the methodology to estimate the predicted uncertainty of each of the parameters. In order to evaluate the applicability of the prediction error theory in estimating the predicted uncertainty of the SEMD parameters in ECG signals we used eq (3.68) to estimate the covariance matrix of the estimated parameters from the median ECG signals, from which we obtained the predicted uncertainty of each of the spatial parameters of the SEMD (shown in the first three lines of Figure 5-13 in magenta). The confidence intervals at the time of the earliest activation are: ($\sigma_x = 0.006 \text{ cm}, \sigma_y = 0.006 \text{ cm}, \sigma_z = 0.010 \text{ cm}$). In the same plots (one to three of Figure 5-13) we show the confidence interval of each of the spatial parameters of the SEMD due to different measurement noise realizations.

We see that the uncertainty derived from the prediction error theory and the uncertainty due to the measurement noise realizations are in excellent agreement indicating that the prediction error theory may be used to estimate the uncertainty of the spatial parameters of the SEMD model due to measurement noise.

In Figure 5-14 we plot the confidence interval from the best solution that the χ^2 changed be 95% (given by 3.74). Here, the number of dof = 50 (file 11j94:c6) and

the 95% confidence interval will be given by [65]

$$ci_{(\chi^2)_{95\%}} = (\chi^2)_{0.975|_{dof=50}} - (\chi^2)_{0.50|_{dof=50}} \quad (5.11)$$

$$= 71.42 - 49.33 \quad (5.12)$$

$$= 22.09 \quad (5.13)$$

In the same lines (one to three of Figure 5-14) we show the confidence interval of each of the spatial parameters of the SEMD due to different noise realizations. The confidence intervals for due to the spatial variation in the χ^2 at the time of the earliest activation were: ($\sigma_x = 0.013 \text{ cm}$, $\sigma_y = 0.015 \text{ cm}$, $\sigma_z = 0.024 \text{ cm}$).

We also provide in the fourth entry the χ^2 and RNMSE across the cardiac cycle.

In the fifth entry of each of the Figures 5-13 and 5-14 we plot the median ECG signal obtained at a body surface site. In the same entry with the left marker we indicate the end of the pacing spike, and with the right one the earliest activation point. The distance between these two markers indicates the distance between these two SEMD locations.

We see that both parameters (the one obtained the prediction error theory and the one obtained by the spatial variation of the χ^2) follow variations of the ECG signals during in the cardiac cycle: (i) they are large during the pacing spike and the end of the end of the T-wave, when repolarization is completed and signal to noise ratio is low, (ii) take their minimum value close to the peak of the QRS complex, (iii) increase during the terminal portion of the QRS when the activation front becomes largely distributed, (iv) remain relatively constant during the ST-segment and T-wave; the later is in agreement with the observation we made in Figure 5-9 where no significant motion in the position of the SEMD was observed during repolarization (the position of the equivalent dipole reflects the position of the geometrical center of the highly distributed repolarization wave-front).

We noted that the 95% confidence interval values due to χ^2 variation are larger

than the 95% confidence interval values due to the prediction error theory for the same time instants. This is because the latter assumes that the model used is the right model and the only source of error is due to measurement noise, while the later is an estimate that includes the realistic anatomic geometry and tissue inhomogeneities.

5.11 Beat-to-beat Variation of the SEMD Parameter Estimates

To further examine the beat-to-beat variation and uncertainty of the SEMD parameter estimates with time, the inverse algorithm was applied to a series of sequential beats (file 11j94:C6). Then, the statistical properties for each sample-point across beats were calculated. The results of this analysis are summarized in Figure 5-15. In Figure 5-15, we plot the median solution and one standard deviation (obtained from eq 5.10) around it for each of the SEMD spatial parameters (lines 1-3) along the cardiac cycle (line 5). The median solution represents the median distance from the origin of the solution along each of the major axis. We also show the χ^2 and RNMSE obtained from the median beat. We see that the uncertainty is large during the pacing spike and also after the T-wave, when repolarization is completed and the signal to noise ratio is small. However, it is especially low during the portion of the cardiac cycle that we are mostly interested in; i.e. from the earliest activation time indicated by the first marker in the ECG signal ($\sigma_x = 0.22 \text{ cm}, \sigma_y = 0.38 \text{ cm}, \sigma_z = 0.14 \text{ cm}$), till the minimum value of the RNMSE error indicated by the second marker ($\sigma_x = 0.36 \text{ cm}, \sigma_y = 0.70 \text{ cm}, \sigma_z = 1.65 \text{ cm}$).

The significance of this figure lies not only in the fact that the spread of the spatial SEMD parameters is small when we want to ablate, but also in the fact that it demonstrates that analysis of only a few beats of a monomorphic rhythm like monomorphic ventricular tachycardia could provide meaningful results about the

locus of the tachycardia.

5.12 Resolvability of two Epicardial Pacing Sites

The ability of our algorithm in resolving electrical events in the heart was evaluated in Figure 5-16. In this figure data from two pacing sites are displayed. We used two epicardial sites (files 11j94:B6,11j94:C6) that were located 2.8 *cm* (center-to-center) apart on the epicardial sock, to stimulate the heart. In the second entry we plot the χ^2/dof and RNMSE obtained from the analysis of the median ECG signals obtained during the first protocol and in the third entry we present a representative example of one electrode ECG signal. Similar, information is presented in the fourth and fifth entries for data obtained during the second pacing protocol. All plots all aligned to the last point of the pacing spike that was visually selected by the author. Also, the earliest activation point for each pacing site is indicated on the ECG signal by a marker.

In order to estimate the spread of the solutions at each time point during the cardiac cycle we used the continuous analysis algorithm to estimate the beat-to-beat variation in the SEMD parameters at each time point during the cardiac cycle.

In the first entry we plot a quantity called *coefficient of variation* (CV) ($0.0 \leq CV \leq 1.0$) defined as

$$CV = \frac{\sqrt{\sigma_1^2 + \sigma_2^2}}{|\mathbf{r}_1 - \mathbf{r}_2|} \quad (5.14)$$

where $\sigma_i^2 = \sigma_{ix}^2 + \sigma_{iy}^2 + \sigma_{iz}^2$ and each of the σ_{ij} is obtained from 5.10, \mathbf{r}_i is the median position vector of the i_{th} protocol obtained from $D_{i,med}^2 = D_{i,x-med}^2 + D_{i,y-med}^2 + D_{i,z-med}^2$

Values of the CV of close to zero/one show good/bad separability of the two cluster distributions (solutions), while values larger than 1.0 are uninterpretable.

In the same figure we plot the median distance (D) and one standard deviation (σ) around D for each point during the cardiac cycle. From Figure 5-16 we see that for the time window that CV provides the best separability (in the sample number window of [15,25]), the value of D when CV becomes minimum is 2.85 cm and σ is 0.39 cm . In the same window the range of D was $(2.84\text{ cm} \leq D \leq 3.60\text{ cm})$, while the range of σ was $(0.39\text{ cm} \leq \sigma \leq 1.20\text{ cm})$ that is very close to the physical distance of the two electrodes on the sock.

When both pacing protocols were aligned according to their earliest activation points D was found to be 3.35 cm and σ was 0.49 cm .

We also calculated the coefficient of variation, the median distance (D), and the one standard deviation (σ) around D for each point during the cardiac cycle from using the median ECG signals (Figure 5-17) to which different noise realizations were added. Now, D is the distance between the spatial SEMD parameters obtained from the analysis of the median ECG signals during pacing from each of the pacing sites, where σ is given by $\sigma_i^2 = \sigma_{ix}^2 + \sigma_{iy}^2 + \sigma_{iz}^2$ and each of the σ_{ij} is obtained from 5.10 applied to the distribution of the spatial SEMD parameters obtained from different noise realization.

In the same figure we plot the median distance (D) and one standard deviation (σ) around D for each point during the cardiac cycle. From Figure 5-16 we see that for the time window that CV provides the best separability (in the sample number window of [15,25]), the value of D when CV becomes minimum is 2.66 cm and σ is 0.01 cm . In the same window the range of D was $(2.22\text{ cm} \leq D \leq 2.80\text{ cm})$, that is very close to the physical distance of the two electrodes on the sock, while the range of σ was $(0.01\text{ cm} \leq \sigma \leq 0.03\text{ cm})$.

When both pacing protocols were aligned according to their earliest activation points D was found to be 3.06 cm and σ was 0.02 cm .

We observed that using the spatial SEMD parameters obtained from the analysis

of the median ECG signals yielded lower values of σ at the time window during the cardiac cycle we are mostly interested in. Beat-to-beat analysis of the ECG signals yielded higher σ due to respiratory effects in the beat-to-beat variation in position of the heart.

5.13 Ventricular Activation-Recovery

The intracardiac distribution of current sources and sinks in ventricular activation and recovery are different. During ventricular depolarization (activation), the sources and sinks of depolarization currents are concentrated in comparatively narrow regions comprising the activation fronts and the adjacent myocardial fibers. On the other hand, during ventricular repolarization (recovery) every myocardial fiber starts that has been in the pathway of the activation front, emits recovery currents and continues to do so until recovery has been completed. Recovery is not synchronous in all the fibers, and while some fibers are in a more advanced stage than the others, extracellular currents will flow from the former to the latter, distributing themselves to the whole heart.

During the QRS-complex, recovery currents are generated only by those fibers through which the excitation front has already passed. Initially only a few fibers are emitting currents and the current intensity is low. During the T-wave (phase 3 of the action potential) however, when most fibers are recovering, the intensity of the repolarization currents is stronger and the surface potentials are strongly affected by the recovery currents. Thus, the peak in the terminal portion of the QRS may be attributed to the largely distributed recovery currents. During the ST-segment and the beginning of the T-wave the ventricular fibers are generating recovery currents. These generators are no longer more concentrated in small regions (as during the QRS-complex), but rather occupy most of the myocardium. Finally, during the last portion

of the T-wave some fibers have totally recovered while others are still completing the repolarizing process. Then extracellular currents flow from fibers that have completely repolarized to those that have partly recovered. At every stage of ventricular recovery the pathway of extracardiac currents and thus the surface potentials will depend on the location in the heart of the more completely repolarized fibers in relation to those that are less repolarized.

5.14 Pacing Spike Identification

This study was designed to evaluate the ability of an inverse algorithm to non-invasively characterize electrical sources in the heart. A reasonable approach in identifying cardiac electric events is to resolve the location of pacing sites in the heart. In this manner single-site epicardial pacing through a sock which was placed around the heart appeared to be a reasonable model to verify the localization accuracy of the SEMD model.

On the other hand pacing from two epicardial sites provides information about the ability of the inverse algorithm to resolve complex potential patterns, electrograms, and activation sequences when multiple, interactive wave fronts are present in the heart.

The pacing protocol can be viewed also as simulating single or multiple ventricular ectopic foci. Focal sites of initiation of arrhythmogenic activity can result from abnormal automaticity, triggered activity, or micro-reentry [36,79]; since, the focus is usually confined to a small region of the myocardium, it can be simulated by pacing the myocardium at a single site.

In previous studies [69,76], pacing spike representation with a SEMD, showed that the location of the SEMD may not correspond with the position of the pacing electrode because of intrinsic or cardiac factors such as wavefront displacement

and non-dipolarity. In terms of the dipolarity of these initial waveforms Spach and Barr [76] have described the activation fronts (resulting from two ventricular sites), occurring 40 msec after the stimulus, as not well represented by a SEMD. Ideker et al [34] has reported a distance of 3.7 mm with a range of 2.6-4.6 mm between the initial SEMD location and a sub-epicardial pacing electrode implanted in the left ventricle in rabbit.

In our study the pacing spikes were bipolar electrograms delivered by each of the electrodes on the epicardial sock. The inter-lead distance of the electrodes was 3mm, while the inter-electrode distance varied depending on the relative position of the electrode to the heart, but in every case it was significantly larger than the inter-electrode distance.

Although, it seems natural that the bipolar pacing spike would be mostly represented through the dipole model, in Figure 5-9, in the right column we see that although the positions of the pacing spike for each of the bipolar pulses should coincide, indeed they are not. Furthermore, our results showed that it was not possible with some degree of certainty to localize the pacing spike with the SEMD model, when the median beat of each channel was used (Figure 5-12). The same result was obtained when the continuous algorithm was used and pacing spike identification was attempted on a beat-to-beat basis (5-15). Even when an additional offset (made from the mean electrogram in a time window preceding the beginning of the pacing-spike) was subtracted from the pacing-spike voltage amplitude, that also did not lead to successful identification.

These results might be explained, in part, by the fact that other investigators [20, 58, 89], in tank studies, have suggested that the potential distribution observed outside and inside the wavefront in

the initial stages of propagation following a pacing spike, is similar to that produced by two collinear dipoles at 180° from one another (linear quadrupole) as indicated in Figure 5-18. However, these results refer to the potential and current patterns 9 msec after the introduction of the pacing spike. When the pacing spikes from various epicardial sites were identified they were found within single mm from the actual positions and with an estimated error of ≈ 15 mm.

5.15 The Effects of Thoracotomy

The effects of thoracotomy were assessed by comparing pre- and post operative normal ECGs. For all animals the pre- and postoperative vector loops were similar. The SEMD trajectory showed more differences, but their general feature were retained. Similar results were obtained by Savard et al [69]. However, the animals became ischemic during the operation an indication of which is presented in ST elevation that was observed in all experimental days. The arrhythmogenic effect of thoracotomy was also noticed in frequent atrial tachycardia episodes and in some cases death of the animal soon after opening the chest.

5.16 On the Unipolar Electrocardiogram

Potentials generated by current sources in a volume conductor such as the heart are always recorded with respect to the potential at a reference site. Unipolar signals are referenced to an electrode that theoretically is located at an infinite distance from the recording site. Therefore, a unipolar signal reflects influences from both local and distant electrical events, and their contribution decreases with distance (eq. 2.6). Simultaneous recordings of both intracellular and extracellular electrograms have shown that the down-stroke of the unipolar electrogram, the intrinsic deflection coincides with the upstroke of the action potential beneath the exploring electrode

[35]. The intrinsic deflection mirrors local activation, while sections of the electrogram occurring before or after the intrinsic deflection are caused by activation fronts distant from the recording electrode.

While the initial deflection of the electrocardiogram is negative at a site where activation arises, the reverse is not true. Anisotropy may cause initially negative deflections at sites where an activation front passes. These negative deflections, however, are of low amplitude and a low negative derivative and are followed by a bi-phasic component.

Because peak values of membrane currents are the main contribution to recorded potentials, if we assume that the recorded potentials are the result of a sum of individual current dipoles (eq. 2.6) that can be regarded as one dipole, then knowing that the current dipole generates positive potentials at the “source” (the area in front of the wavefront) and negative potentials at the “sink”, we may interpret the characteristics of the unipolar signals generated by a wavefront propagation (in a one dimension, that is along fibers or as a plane wavefront) in terms of the SEMD assumption as: (i) at sites where the activation front (dipole) encounters an electrode, the area in front of the dipole is encountered first and the potentials are positive, resulting in a positive signal deflection; when the wavefront is located under the electrode, the induced potential is zero and becomes negative when the wavefront moves away from the electrode. (ii) a wavefront that is moving towards inexcitable barriers, such as infarcted zones or tissue boundaries will generate positive deflections only; since the dipole cannot pass the recording site the latter will be always located in the positive area of the current dipole.

Although the straightforward interpretation makes appealing the unipolar signal, the fact that it reflects both local and remote activation, may cause some large deflections to mask small local events. Also, the sensitivity to far-field effects makes the unipolar signal vulnerable to 60-Hz interference, thus requiring careful design of the

recording system.

Alternatively, a bipolar recording may be used. Bipolar signals may allow identification of low amplitude local activity, which can be buried within large remote components in the unipolar mode. It has been recently demonstrated [31, 33], that measurement of the surface Laplacian of the potential is highly sensitive in resolving cardiac bio-electric events. This might be due to the fact that the signal recorded by the Laplacian electrode is resulting from a SEMD source that decays with the inverse fourth power of distance of the SEMD from the Laplacian electrode. In contrast, the SEMD's contribution to the signal recorded by a unipolar electrode only decays as the inverse square power of distance.

Since detection of the earliest sign of activation in the surface ECG signal is of major importance in identifying the arrhythmia source, it might be that, in the future, use of a combination of unipolar and bipolar signals could provide an optimal approach in enhancing the utility of the SEMD methodology in identifying the site of the arrhythmia.

5.17 On the Single Equivalent Moving Dipole Assumption

The single equivalent dipole localization method is based on a mathematical model, that like any other model, leads to conclusions that are valid only under the model's underlying assumptions. Because of variations in resistivity, shape and thickness of the human body it appears that any simplifying assumptions about the torso anatomy may be important source of error.

The validity of the SEMD method assumption depends upon the manner in which the assumption is formulated. Let's consider the following versions of the dipole assumption (i) The physical dipole assumption: when the body surface ECG potential

measurements closely approximate that of a dipole field and in fact are generated by a point dipole (ii) The spatially constrained equivalent dipole assumption: when the body surface ECG potential measurements closely approximate that of a dipole field, are generated by a spatially restricted region of current sources and sinks and lastly can be attributed to an equivalent dipole that is located in or near the region of current sources or sinks. (iii) A non-spatially constrained equivalent dipole assumption: when the body surface ECG potential measurements closely approximate that of a dipole field, that are generated by an arbitrary distribution of current sources and sinks and lastly can be attributed to an equivalent dipole that can be located anywhere relative to the distribution current sources or sinks.

These three descriptions that ascribe to a potential field properties generated by a point dipole differ in the extent to which the term “dipole” refers to the physical dipole configuration of sources and sinks as opposed to a mathematical description of a potential field. Also, they differ to the degree that the equivalent dipole is appropriate for the configuration of the actual sources and sinks. The assumptions pertain to the equivalent dipole are distinguished by whether or not they make additional assumptions regarding the actual distribution of sources and sinks relative to the equivalent dipole; the spatially constrained case that assumes that the distribution of sources and sinks is relatively restricted in size and is located near the location of the best fitting equivalent dipole, is the stronger.

However, as a physical description of sources and sinks, the dipole approximation refers to two closely spaced point sources of current having equal and opposite polarity. This physical definition cannot be met by physiological sources since they are, to some degree, by their nature always spatially distributed. On the other hand the dipole approximation also refers to the second term in the multipole expansion that is used to express the potential due to an arbitrary configuration of sources. The significance of the dipolar term in the potential field lies on the fact that its contribution falls off

as the inverse square of the distance from the source, while contributions from higher terms fall off with increasingly higher powers.

When the SEMD objective function statistic is indicative of inappropriate convergence, then the SEMD appears to be inappropriate for the specific data set. On the other hand a satisfactory objective function value indicates if the body surface ECG potential measurements approximate a dipole field or if the spatially unconstrained assumption for the equivalent dipole is met. Thereafter other statistics are required to verify if the field is generated by a spatially restricted distribution of current sources and sinks located closely to the equivalent dipole.

During the depolarization phase of the ventricles, which occurs in the QRS complex of the electrocardiogram, the electric forces in the heart attribute to the equivalent cardiac generator are distributed on the excitation fronts as electric double layers, so that the location, the direction, and the magnitude of the equivalent dipole are expected to indicate the mean location, the normal direction, and the size, respectively of the corresponding excitation front.

In clinical applications, the excitation front grows so large as it propagates in the ventricles that it can no longer be regarded as being localized. Moreover, the excitation front sometimes has openings in it, hence, it is desirable to find a relation between the SEMD and the related excitation front. The geometry of the excitation front that forms the double layer, is responsible in determining the potential distribution. When an excitation front reaches the myocardium boundary, part of the excitation front is broken and the closing boundaries are not any more single-connected. Then there are exist several excitation fronts.

5.18 On the Significance of the RNMSE in ECG Signals in the Limit of Small Measurement Noise

The non-dipolar components during some phases of the ventricular excitation have been first reported by [88], as evidenced by multiple maxima or minima at the same time on the normal human thorax. However, there have been only few studies from the standpoint of electrocardiographic inverse solutions on the dipolarity and SEMD locus during the cardiac cycle.

The RNMSE, that represents the minimized root-mean-square deviation between the measured potential distribution and that generated by the SEMD after being normalized to the root-mean-square value of the measured potential distribution, suggests, how much potential component is left which cannot be attributed to the SEMD in the absence of noise. When the electrical of the heart is low, for example during the early part of the QRS, the potential distributions are largely disturbed by noise, and even though χ^2/dof is small, the RNMSE is large.

The RNMSE may also reflect the complexity of the excitation fronts. If the RNMSE is small with a SEMD, it can be said that the excitation front propagating in the heart has a simple shape. If the RNMSE is large, contrary to this, with a SEMD, there may be plural excitation fronts or the excitation front is largely distorted. In such a case, another (second) equivalent dipole or a higher order source (i.e. quadrupole, etc) may be responsible for the measured potential. It may also be that the RNMSE is considerably reduced after an additional source has been added, and thus it follows that there exist two significant excitation fronts, each equivalent source representing a mean position, direction and size of the corresponding excitation front. If the RNMSE remains large even with an additional source, there may be more

than two excitation fronts or the excitation front may have a complicated shape.

During the early and last stage of the depolarization, when there is still a small excitation front, the SEMD location “coincides” with the mean location of the excitation front. Later, after 20 ms following the onset of the ventricular depolarization, the deviation of the SEMD location from the mean location of the excitation front is large, even though there is only one excitation front. The reason is that the excitation front at this time originated from fusion of several excitation fronts and has a more complicated shape throughout the ventricular depolarization. Afterwards, there is a dominant closing boundary attended by several small ones, and the SEMD is estimated near the center of the largest one. Alternatively, during the terminal part of depolarization an excitation front reaches the boundary of the myocardium and a hole is made on the excitation front; then, since the hole can be replaced by an excitation front with a reversed polarization, an excitation front with a hole is expressed as a superposition of two dipole layers, with reversed polarization. Thus, body surface potentials caused by one or more excitation fronts is equally and oppositely affected by the reversed polarity excitation front, so that while χ^2 decreases the RNMSE increases. This is in agreement with [88], that described non-dipolar behavior during this phase of ventricular depolarization as reflected of multiple maxima or minima in body surface potential maps.

The RNMSE of ventricular repolarization was stable and low. Although we were able to search for the SEMD during the repolarization process, which corresponded to the T-wave of the electrocardiogram, we restricted ourselves in the interpretation of the RNMSE only to the depolarization processes, because the excitation front is distributed over the entire heart during repolarization, and hence it was difficult to ascribe them properties of a SEMD.

Finally, in a diseased heart when the excitation front reaches an infarction in the myocardium where the electric dipole moment is not developed, a hole is made on the

double layer of the excitation front and the RNMSE becomes larger there. Hence, it may be possible to estimate the location and size of the infarction from the timing and the magnitude of a peak in the RNMSE curve.

5.19 Discussion

In this chapter, we present results from experiments conducted in a swine model. In these experiments, the heart was paced from various epicardial electrodes located on a sock encompassing the heart, and surface potentials were recorded from 60 body surface electrodes. We applied our newly developed inverse algorithm, to the body surface potentials and estimated the dipole parameters for each point in the cardiac cycle.

We showed that the algorithm we developed to identify the SEMD yielded reconstructed potentials that were highly correlated with the measured potentials, even though the cardiac electrical source was not well-localized at every instant (i.e. during the T-wave) and the distortions due to the bounded, heterogeneous volume conductor were ignored. This was shown to be valid (i) in the case that the the SEMD parameter estimates obtained from the median beat of the first half of a sequence of paced beats, were used to reconstruct the ECG values at the same sites, and predict the median beat of the second half of the paced sequence, (ii) when beat-to-beat analysis of the SEMD parameter estimates was performed and the minimum RNMSE value at each instant was chosen as the best solution of all best solutions across beats.

We estimated the uncertainty in the location of the dipole using a number of methods (file 11j94:C6). The first method involved adding to the median ECG beat different realizations of the estimated measurement noise, and applying the inverse algorithm. The uncertainty of the dipole location was estimated from the distribution of the spatial SEMD parameters. The second method involved application of the

prediction error theory to the estimation of the confidence interval of the spatial SEMD parameters. The third method involved analysis of the spatial variation of the χ^2 . The fourth method involved an analysis of the distribution of the spatial SEMD parameters obtained from analysis of a series of sequential beats. The first three methods yielded very similar estimates of the uncertainty (and also very small, at the point of the earliest activation $\cong 0.01$ cm). The fourth method that involved beat-to-beat analysis yielded larger values of the uncertainty (at point of earliest activation 0.25 cm). The likely reason that the fourth method yielded a larger estimate of the uncertainty is likely due to the respiratory motion of the heart and chest during the cardiac cycle. The respiratory motion varies the actual position of the dipole in space, but we are interested in the position of the dipole with reference to the heart since the catheter tip will also move with the heart and thus respiratory motion. Thus the uncertainty associated with the first three methods is probably more relevant. In any event, even an uncertainty of 0.25 cm would not be too significant from a practical point of view, since the size of an ablation lesion is $\cong 0.2$ cm (for a 7 French catheter). We also demonstrated that our inverse algorithm could easily resolve two pacing sites within $\cong 2$ cm of each other.

In Table 5.1 we summarize the results of the spatial uncertainty of the SEMD parameters. We see that that the results due to measurement noise realizations, are in excellent agreement to that estimated by means of the prediction error theory, and is comparable to the spatial uncertainty estimated by the spatial variation of the χ^2 .

The fact that the predicted uncertainty and the uncertainty due to the measurement noise realizations are in agreement indicates that the prediction error theory may be used to estimate the uncertainty of the spatial parameters of the SEMD model due to measurement noise.

We used the coefficient of variation (CV) as an indicator of the significance of

Table 5.1: The spatial uncertainty at the point of earliest activation.

INTERVENTION	σ_x (cm)	σ_y (cm)	σ_z (cm)	σ (cm)
Noise Realizations	0.005	0.006	0.011	0.013
Prediction Error	0.006	0.006	0.010	0.013
95% Change in χ^2	0.013	0.015	0.024	0.018
Beat-to-Beat	0.220	0.380	0.140	0.461

the measured distance between the instantaneous SEMDs for two pacing sites. We applied the CV to identify the spatial separation between dipoles in the heart, near the beginning of the QRS complex that is when the electrical activity is highly localized (??). We found that CV was small indicating good separability during the beginning of the QRSs. The distance between the SEMDs became comparable to the uncertainty during the T-wave.

In Figures 5-13 and 5-14 we see that the confidence interval for the location of the dipole is minimal at the time of earliest activation when the source is well localized but also remains small through the peak of the QRS when the source is more distributed. The confidence interval does not directly reflect the size of the source but the uncertainty in the location of the best equivalent dipole representation of that source (its equivalent "center"). When the source is stronger then the location of its equivalent dipole is better determined despite the larger size of the source. This is similar to the results observed in Chapter 4. During the beginning of the QRS, when cardiac electrical activity is concentrated in space, the optimal SEMD indicates the equivalent source position. However, when the electrical activity is diffuse and complex in shape (i.e. during the late QRS, or the T-wave), the optimal SEMD position is a "weighted" mean of the distributed electrical activity.

The χ^2/dof is a statistic that on average compares the residual of the fit to the measurement noise. While a χ^2/dof value of ≈ 1.2 are a legitimate reference value

to characterize the goodness of the fit, values smaller and larger than the above mentioned threshold were encountered throughout the analysis; the former may be attributed to noise over-estimation while for the later noise under-estimation alone can cause highly improbable χ^2/dof values. However, the χ^2/dof reflects also the systematic deviation between the ideal model used by the inverse algorithm and the actual forward problem solution which includes boundary effects, inhomogeneities in tissue conductivity and detailed torso geometry. On the other hand although the RNMSE it cannot discriminate between lack of fit due to noise and lack of fit due to an incorrect model, since it neglects noise contribution.

It should be noted that, although in this study the earliest activation in the surface ECG has been used as a reference time point for the instant during the cardiac cycle that can be mostly represented with a cardiac SEMD, it could be that intra-cardiac electrograms obtained from the catheter inserted inside the heart could be used in defining another time reference. In this case it may only required that the signal-to-noise ratio in the surface ECG exceeds a specific threshold to ascertain a highly localized activation front. Intra-cardiac signals are routinely obtained and used during the standard ablation procedure, either in unipolar or bipolar mode.

Our algorithm assumed that the noise was white, which means all measurement electrodes were uncorrelated to each other. However, in reality, correlated noise always exists in some degree, in physiologic signals, which will impact the solutions. One way of handling the correlated noise to calculate the covariance matrix and include it in the objective function to be minimized.

Figure 5-3 A typical representation of the median beat of 60 channel ECG recording.



Figure 5-4 The process of data collection and analysis.

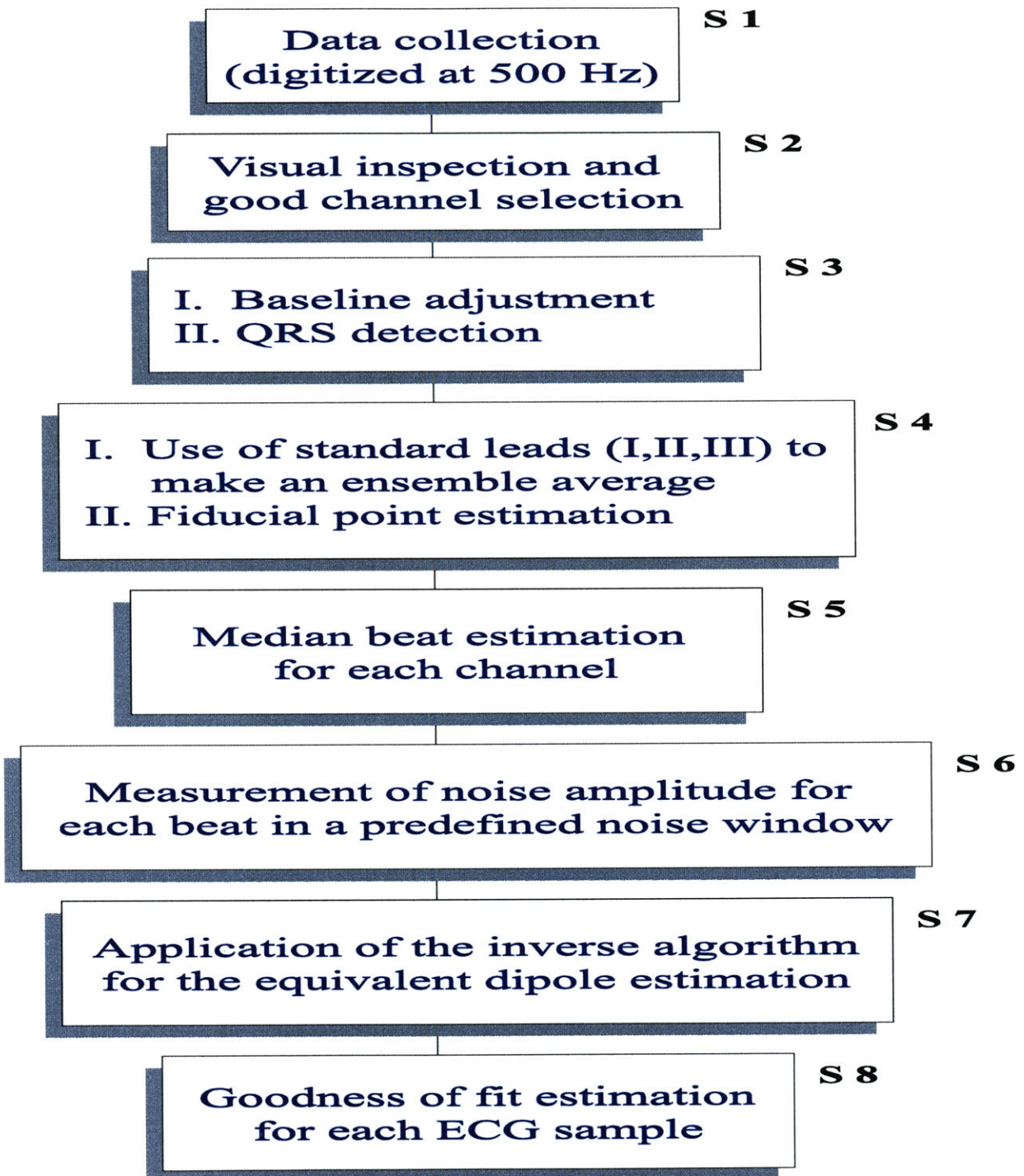


Figure 5-5 ECG beat alignment according to the peak of the QRS

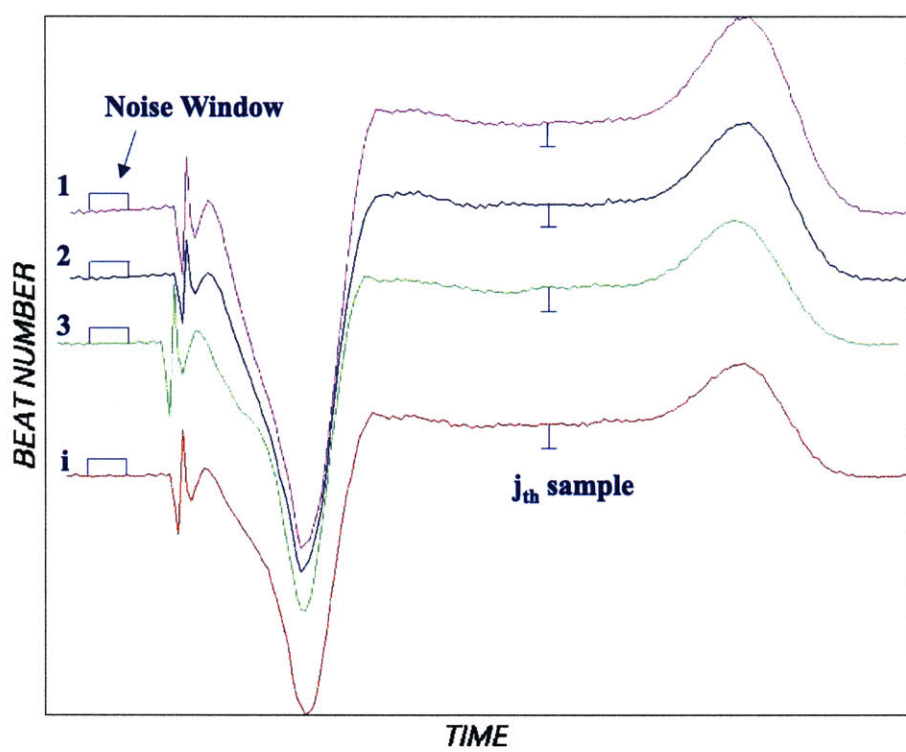


Figure 5-6 The algorithm used in the identification of the equivalent cardiac generator.

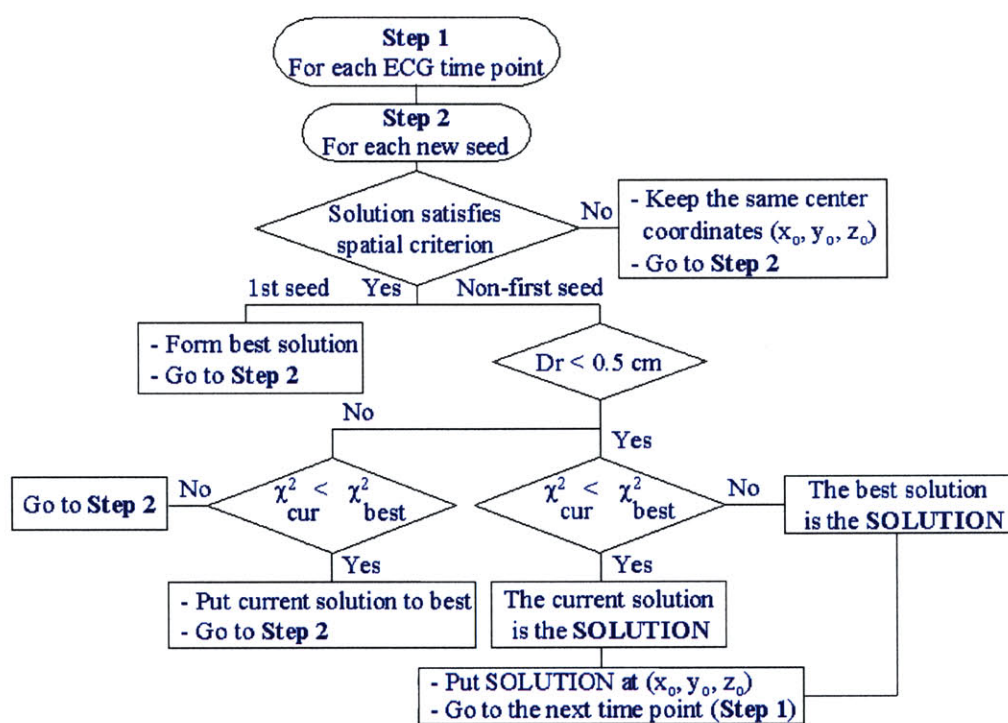


Figure 5-7 The principles of activation mapping for a theoretical reentry circuit [79].

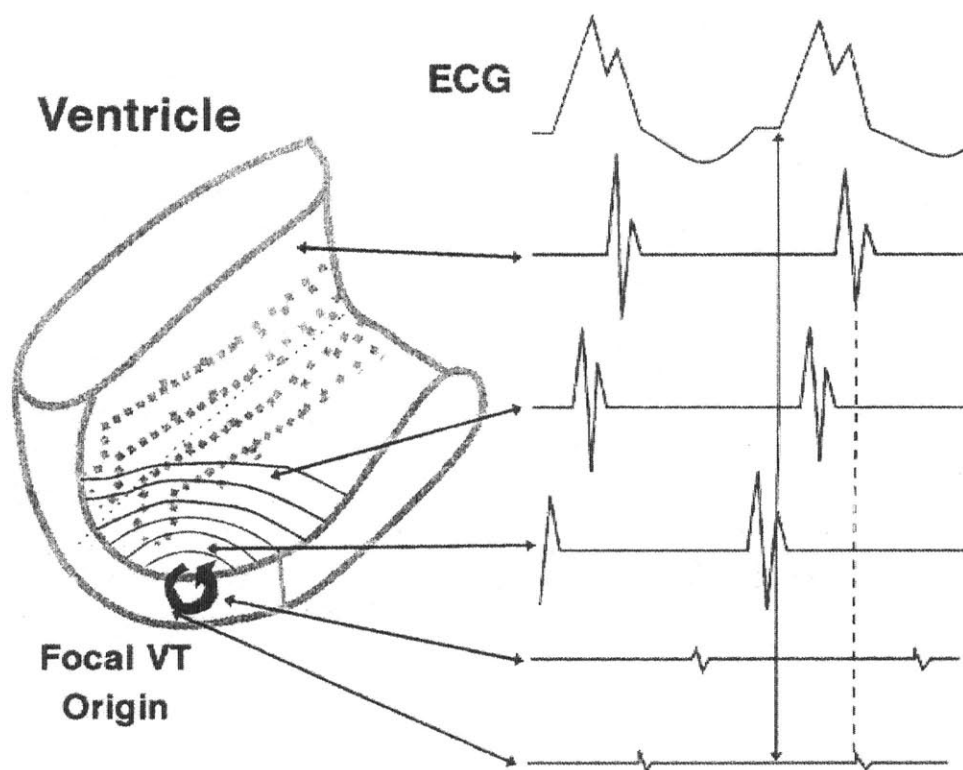


Figure 5-8 Dipole moment of a piece of partially depolarized tissue.

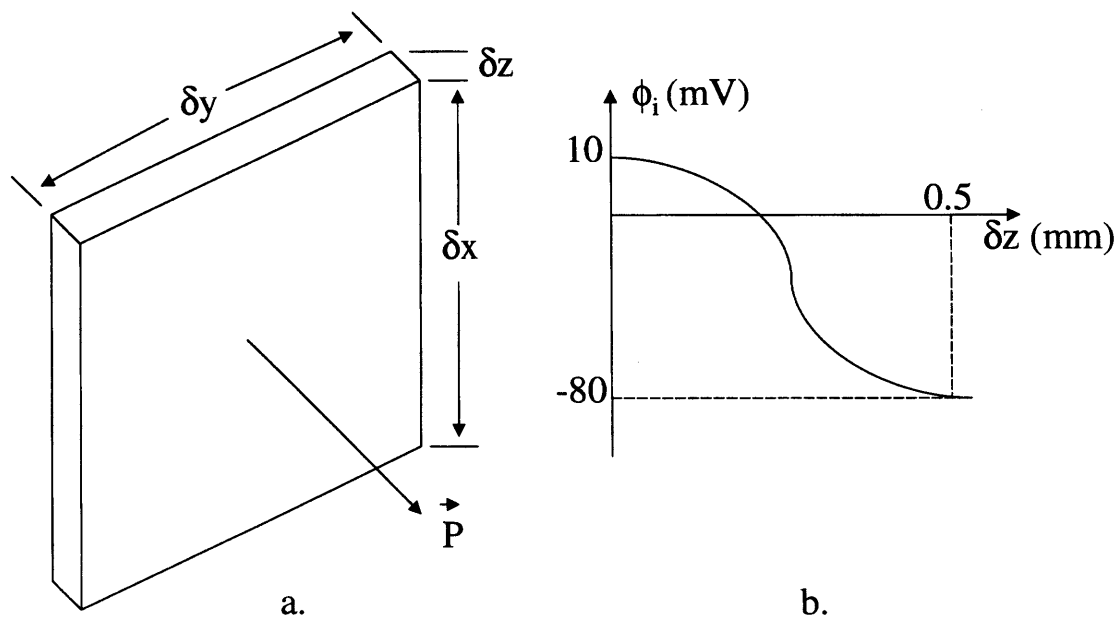


Figure 5-9 Variation of the single equivalent moving dipole parameter estimates across the cardiac cycle (shown in the lower panel).

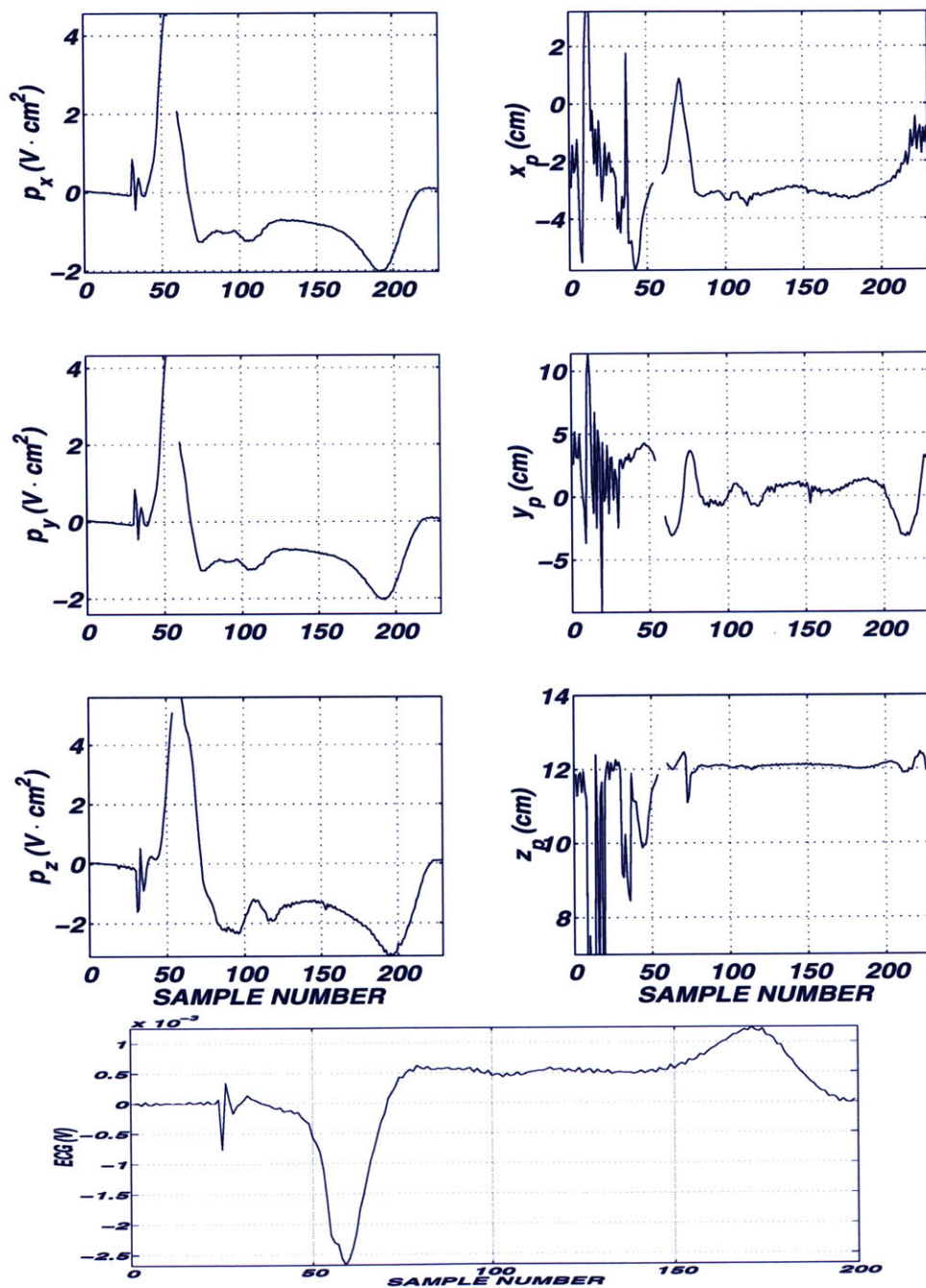


Figure 5-10 Measured (in red), predicted (in blue) ECG signals (median beat) and predicted from continuous data (in green) from nine body surface sites. The correlation coefficient (r) between the measured and predicted signals for each channel is also shown.

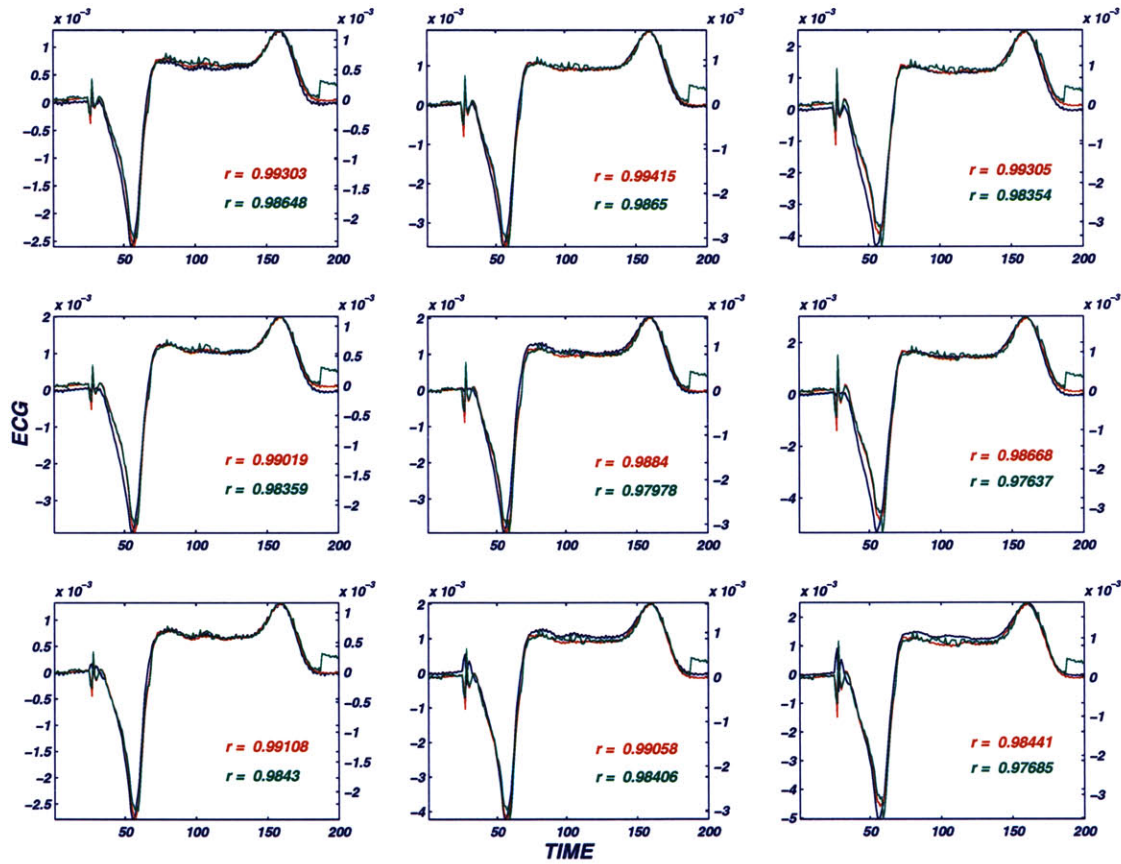


Figure 5-11 Distribution of χ^2/dof values along each of the major orthogonal axes (i.e $-x \rightarrow +x$) and around the optimal solution.

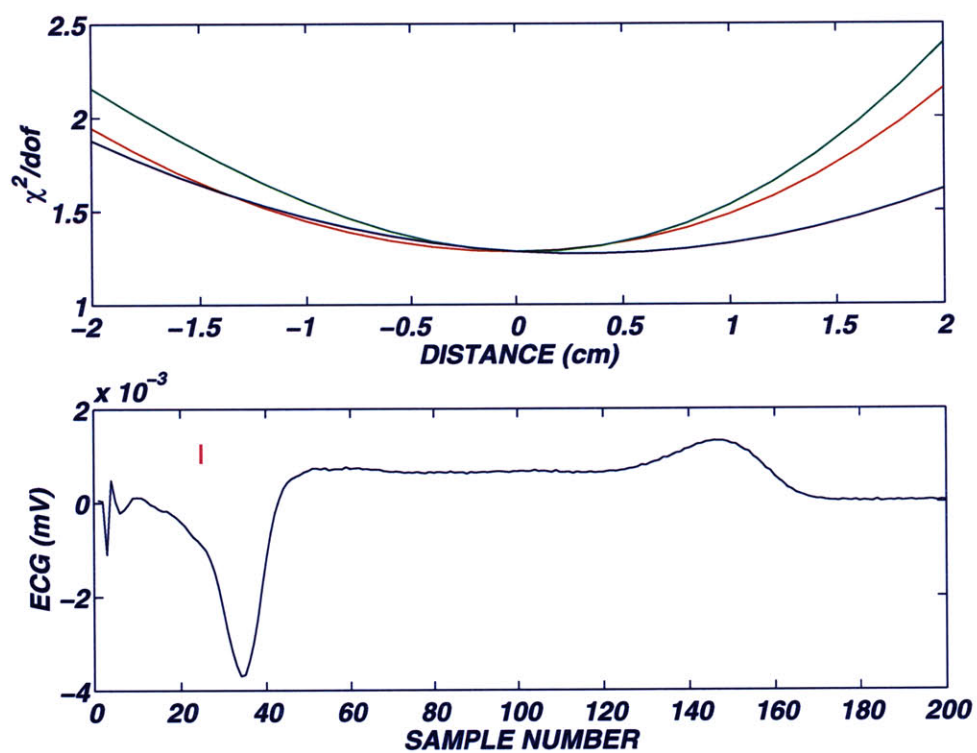


Figure 5-12 The measurement-noise dependent statistical nature of the SEMD parameter estimates.

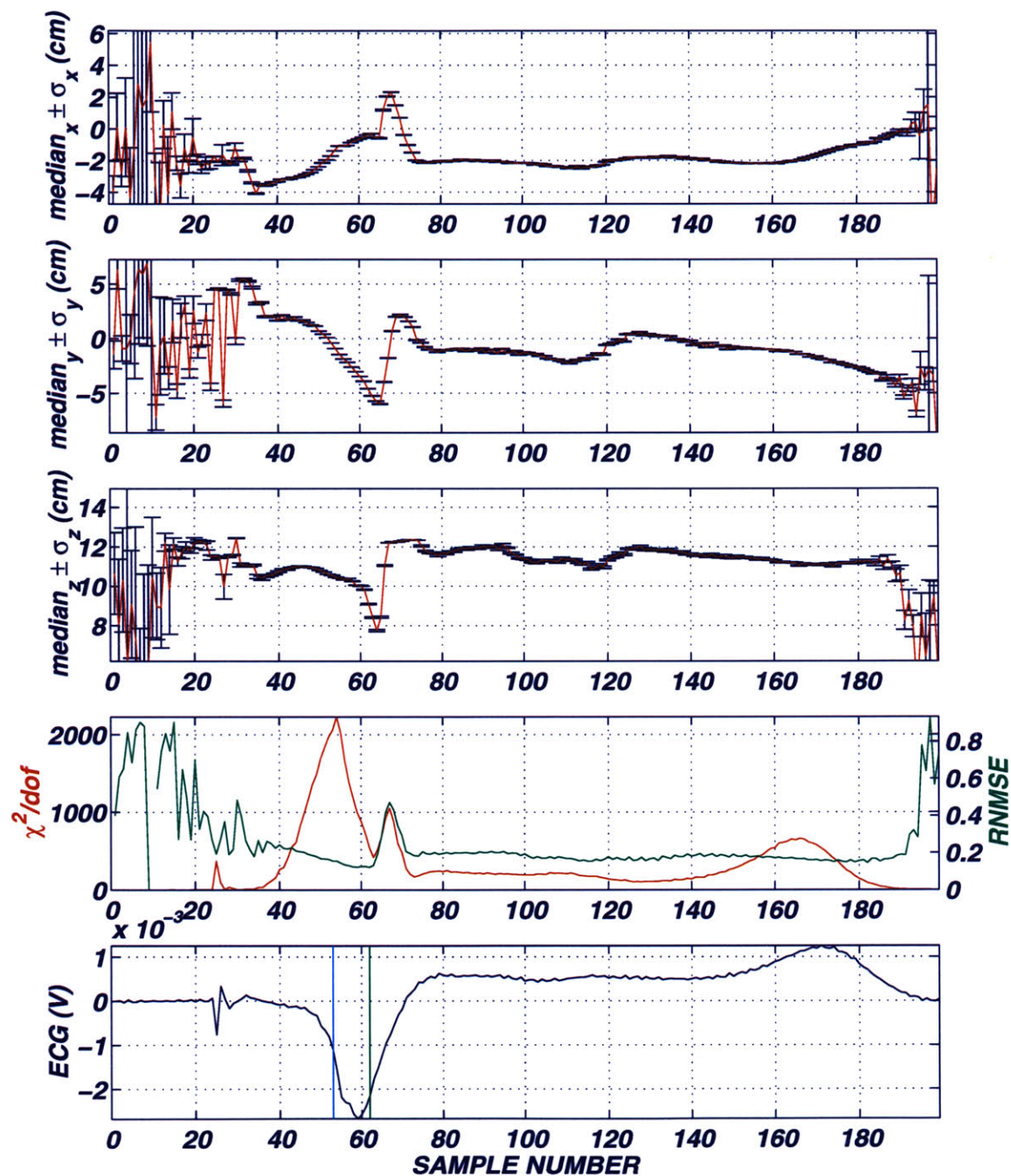


Figure 5-13 Confidence interval of the spatial SEMD parameter estimates obtained from different noise realizations and the prediction error theory.

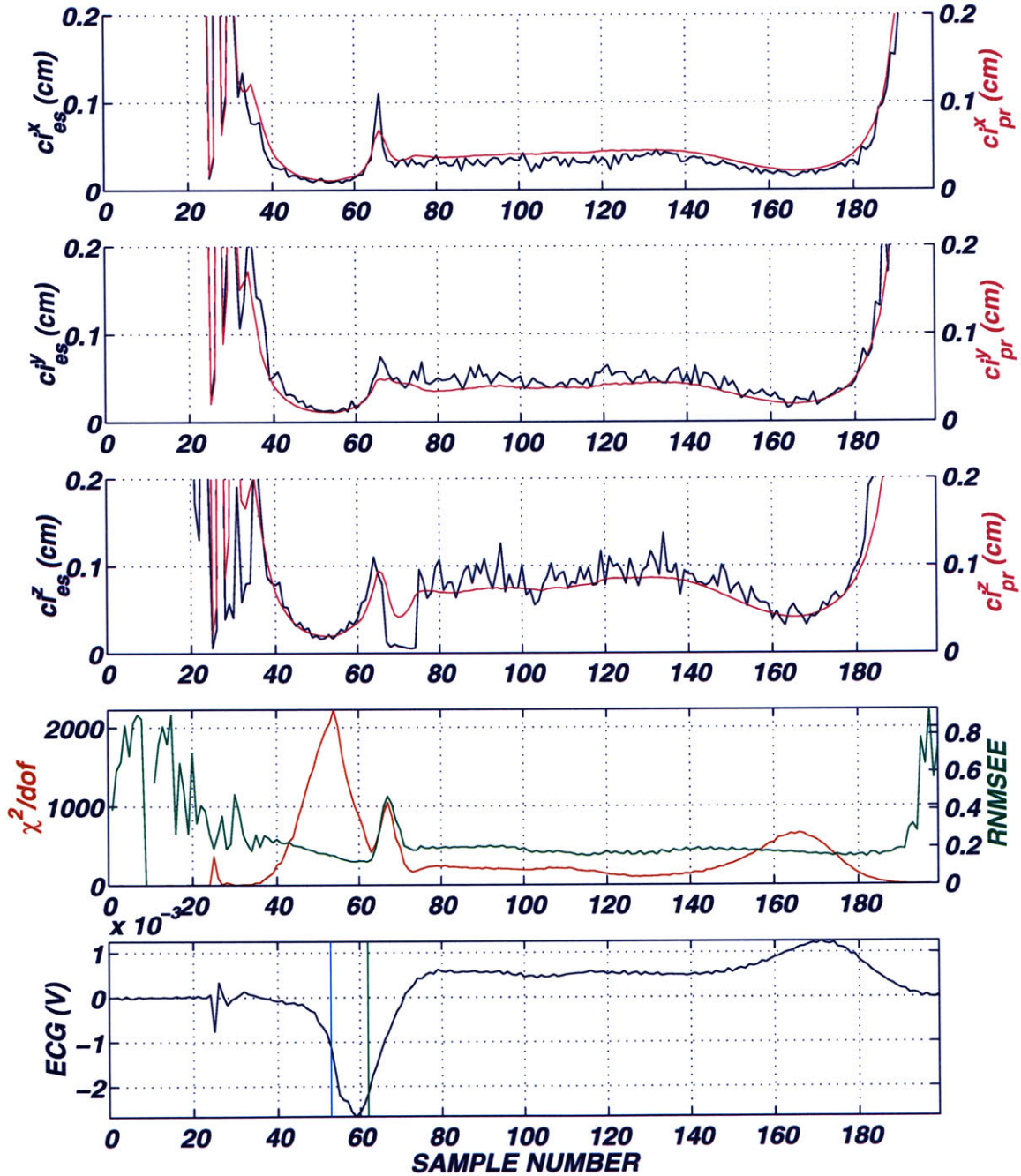


Figure 5-14 Confidence interval of the spatial SEMD parameter estimates obtained from different noise realizations and spatial variation in χ^2 .

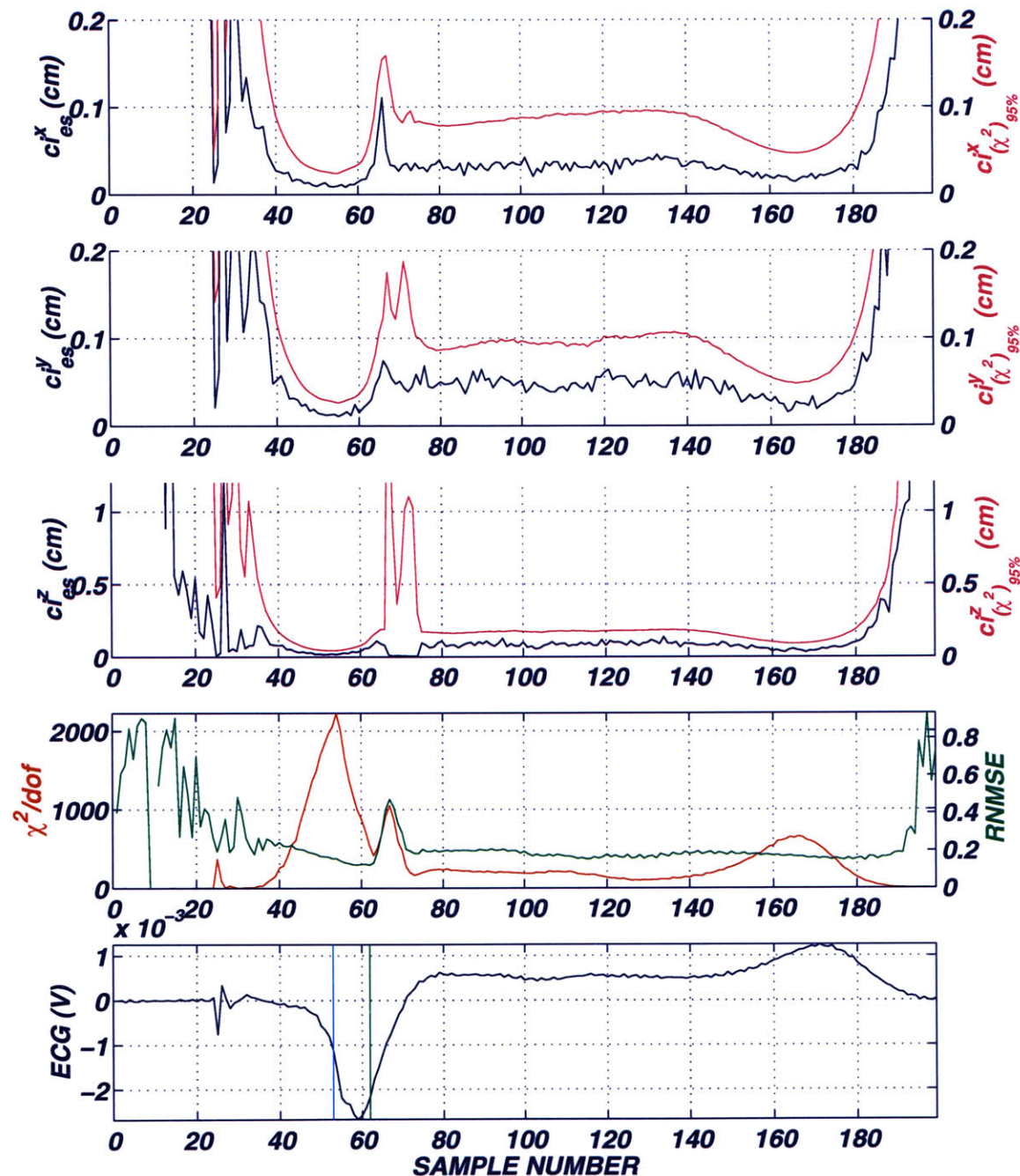


Figure 5-15 The beat-to-beat statistical nature of the single equivalent moving dipole parameter estimates.

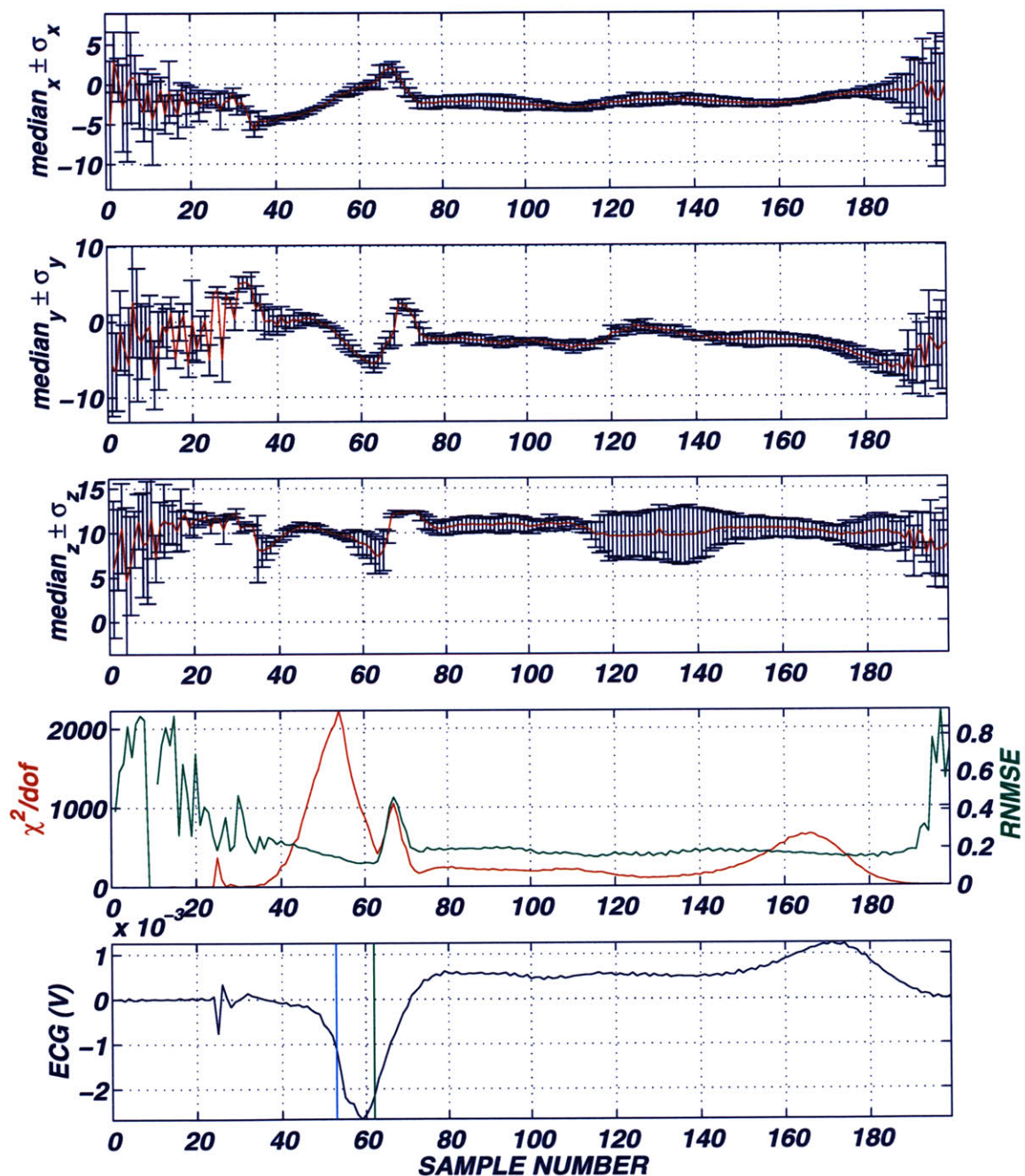


Figure 5-16 Resolution of two epicardial pacing sites based on beat-to-beat analysis.

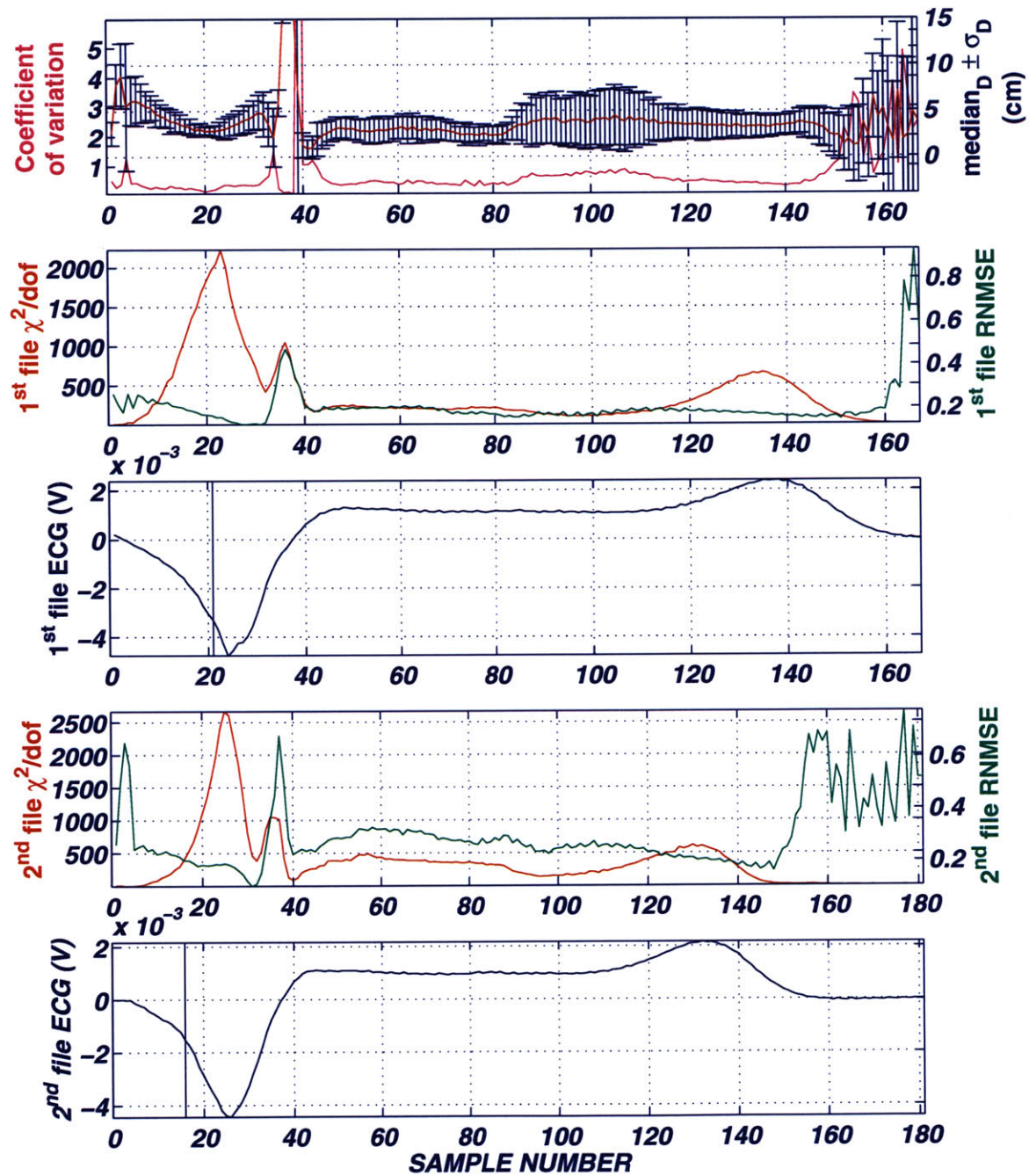


Figure 5-17 Resolution of two epicardial pacing sites based on median beat analysis and different noise realizations.

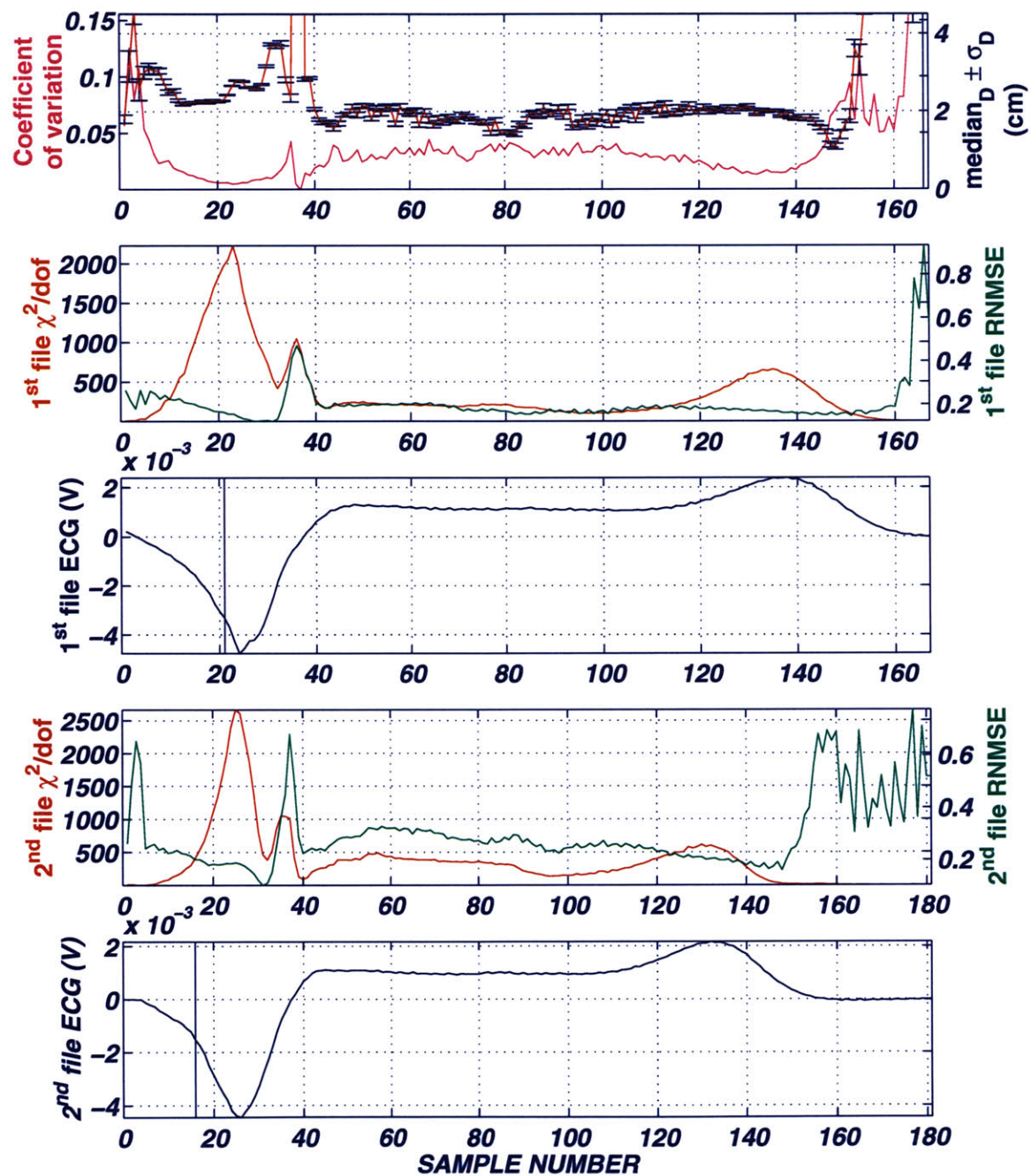
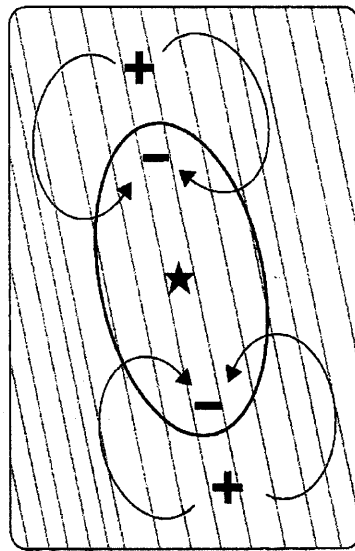


Figure 5-18 Potentials and currents associated with epicardial pacing ([58]); the diagram illustrates potential and current patterns associated with a single with a single pacing spike (★). The region of negativity is elliptical, with the major axis oriented along the fibers.





Lesvos Island - Molivos (Edition: A&E Moliviatis)

Chapter 6

Summary of Results and Conclusions

6.1 Goals Achieved With this Thesis

The major goals achieved with this thesis are three: *Firstly*, we showed that the SEMD model can represent cardiac electrical throughout the cardiac cycle, and especially during the beginning of the QRS when we are mostly interested in (Figure 5-10), *secondly*, we showed that we can localize electrical sources in the heart (Figure 5-16), and *thirdly* we showed that the random dipole orientation is not a significant contributor of error in identifying the spatial dipole parameters, thus the tip of the ablation catheter that is of unknown orientation can be guided to the site of the origin of the arrhythmia (the ablation site).

6.2 Detailed Summary of Results

This thesis explored the development and evaluation of a new methodology that would allow the cardiac electrophysiologist to use body surface electrocardiographic (ECG) signals to both identify the site of origin of the arrhythmia in the heart, and guide

the ablation catheter to the same site.

The process we followed in order to achieve that goal was to firstly use computer simulations to evaluate different optimization routines for their (i) convergence power and (ii) accuracy. Three optimization routines were employed: (i) the Fletcher-Reeves-Polak-Ribiere (FRPR), (ii) the Davison-Fletcher-Powel (DFP), and (iii) Simplex. The first two required computation of the function's gradient at arbitrary points, while the Simplex requires only the function. Also two search approaches were taken: (i) one that searched in the six parameter space (for all dipole parameters), (ii) one that searched in the spatial space of the dipole parameters. We found that that the 3 *plus* 3 parameter methods out-performed the 6 parameter ones. The 3 *plus* 3 Simplex method, as opposed to the DFP and FRPR methods, (i) converged at a significantly higher rate and, (ii) converged to the true location with very small uncertainty.

Our intention to ignore boundary effects and inhomogeneities in tissue conductivities in an empirical study led us to examine the effectiveness of various objective functions in handling systematic error in identifying the spatial dipole parameter estimates. To evaluate the effect of the systematic error these functions we used both an unbounded volume conductor and a bounded spherical model, in which the magnitude of the noise varied from electrode to electrode. The bounded spherical model included boundary effects not included in the model used by the inverse algorithm. In these simulations we randomized the dipole location, orientation, and used different noise realizations. We found that the χ^2/dof method still had overall best performance for both the unbounded and bounded models.

In computer simulations we estimated the spatial dipole uncertainty resulting from both measurement noise and dipole orientation randomization. We found that measurement noise did not have a major effect on the spatial dipole parameters, except in the case of unusually high noise (equal in magnitude to the simulated

potentials). The dipole randomization increased the uncertainty in the case of the bounded model, because variation in the dipole orientation induces a systematic error due to the fact that the inverse algorithm uses an ideal model that does not take into account boundary effects or other non-idealities. The significance of the last results lies on the fact that one may with very small spatial uncertainty guide the catheter tip (that in general one does not know its direction) to the site of origin of the arrhythmia. We found that the uncertainty of the above simulation is sufficient to justify the use of our approach in clinical applications such as radio-frequency catheter ablation procedures.

We also investigated a distributed source model to understand the intrinsic limitations associated with the use of a SEMD to localize cardiac electrical sources. The distributed source model provided us with further understanding regarding the temporal applicability of the SEMD model due to the spatial course of cardiac electrical activation.

The conclusions of the use of the distributed source model can be summarized to: (i) the SEMD location was different from the geometrical center of the distributed source, (ii) accurate localization of the SEMD requires a balance between the size of the source (small being better) and the strength of the source with respect to the noise. Generally, large sources have greater strength. This balance determines the size of the source that can be most accurately localized.

In the last part of this thesis our inverse algorithm was applied to body surface ECG signals obtained from an experimental swine model, while the animal's heart was paced epicardially from a sock that was surgically placed during a thoracotomy.

The spatial uncertainty of the SEMD parameter estimates obtained from different noise realizations were very small ($\cong 0.1$ cm). The beat-to-beat variation of the SEMD parameter estimates at the point of the earliest activation showed that the spread of the spatial SEMD parameters is small at the time that one would be interested to

ablate. The latest analysis yielded the largest uncertainty, likely due to the respiratory motion of the heart and chest.

We also showed that the distance of two sources on the heart (epicardial pacing sites) could be identified to be very close to their physical distance.

This thesis aimed to evaluate (i) if and (ii) to what degree a SEMD used to characterize cardiac electric sources attributing to measured body surface ECG signals, can be used as a tool to in real time applications requiring reliable and fast identification of localized cardiac electrical events.

The answers to the last two questions, lying in this thesis, are many-fold. Firstly, we have shown that the SEMD model can represent the ECG signals attributed to bio-electric sources in the heart with high degree of accuracy throughout the cardiac cycle. Secondly, we have shown that our algorithm does not employ computationally intensive approaches (i.e. that include properties of the bounded, heterogeneous volume conductor) can become a real time tool i.e. in guiding the ablation catheter to the site of the arrhythmogenic activity. Thirdly, we have shown that the SEMD model and our algorithm are able to discriminate localized electrical events in the heart with small uncertainty.

In practical use, we expect the SEMD method would be used to rapidly find the site of the arrhythmia. Conventional mapping using electrograms recorded from the catheter tip would be used for the final confirmation and refinement of the catheter tip location prior to ablation. We have demonstrated that the uncertainty in position from the SEMD method presented in this thesis has more than enough accuracy to be used to identify the site rapidly identifying the site for catheter ablation.

However, we should note the many limitations imposed to this study by the experimental procedures themselves. Firstly, the ECG obtained signals were noisy, a problem that can be easily addressed with current advanced noise reduction amplifiers and electrodes. Secondly, we encountered large spatial errors in the location of

the electrodes that were taken to be on the surface of a cylinder rather their actual positions on the animal torso, a problem that can be also addressed (the reader should read the suggested solution to that problem in chapter 7). In addition, use of the ablation catheter to deliver current pulses for calibration purposes will greatly enhance the applicability of this technique (the reader should again read the suggested solution to that problem in the next chapter's suggested future work).

6.3 Final Conclusions on the Accuracy of the SEMD Optimization Algorithm

The conclusions of this thesis are summarized in Table 6.1 by means of the random component of localization uncertainty, at point of earliest activation (estimated from ECG signals obtained during pacing from an epicardial site; file 11j94:C6).

We estimated the root-normalized-square of the noise across channels for the median beat (σ_m) using eq (6.1)

$$\sigma_m = \sqrt{\frac{1}{60} \sum_{i=1}^{60} \sigma_i^2} \quad (6.1)$$

We used the estimated values of σ_m to obtain the localization uncertainty from computer simulations using (i) an unbounded and, (ii) a bounded model, (iii) from experimental ECG signals obtained for different measurement noise realizations at the point of earliest activation, (iv) from computer simulations obtained from from different measurement noise realizations and, (v) random dipole orientations as well as different measurement noise realizations, (vi) from from experimental ECG signals obtained from beat-to-beat estimation of the spatial SEMD dipole parameters.

We have estimated the uncertainty in dipole location in several ways. We estimated the uncertainty due to measurement noise in the simulations involving both an unbounded and a bounded model. For a noise level comparable to what we found experimentally ($14 \mu V$) we found an uncertainty of 0.0111 cm and 0.0039 cm respectively (see Table 6.1, SUDNR and SBDNR).

In experimental data, from adding different realizations of the noise to a median beat we found an uncertainty on the order of 0.01 cm at the point of earliest activation (see Table 6.1, Experimental DNR). These are estimates of the random component of the uncertainty which is most relevant to the problem of superposing a dipole at the tip of the catheter with the dipole at the arrhythmia site.

With respect to the ability to superpose the catheter tip dipole and the dipole associated with the origin of the arrhythmia the random component of the uncertainty due solely to the effects of measurement noise would seem most relevant. These uncertainties are extremely small compared to the size of the ablation lesions ($\cong 0.2$ cm with a 7 French catheter). The uncertainty due to dipole orientation randomization is relevant, if the catheter tip dipole and arrhythmia site dipole are not aligned. These uncertainties are also very small $\cong 0.04$ cm for the bounded spherical model.

Finally, we estimated the uncertainty in dipole location from the beat-to-beat variation of dipole location at the point of earliest activation. This yielded the largest uncertainty, likely due to the respiratory motion of the heart and chest (see Table 6.1, Experimental BTB). Since the catheter tip moves with the heart the variation in position due to respiratory motion is not a significant factor. However, even the beat-to-beat uncertainty which includes respiratory motion is acceptable ($\cong 0.5$ cm).

Table 6.1: Uncertainty in the spatial SEMD parameter estimates.

	Dipole Spatial Uncertainty (cm)
SUDNR ¹	0.0111
SBDNR ²	0.0039
Experimental DNR ³	0.0135 ^a
SUDNR and RDO ⁴	0.0118
SBDNR and RDO ⁵	0.0438
Experimental BTB ⁶	0.4609

¹SUDNR: Simulation Unbounded Different Noise Realizations

²SBDNR: Simulation Bounded Different Noise Realizations

³DNR: Different Noise Realizations, estimated by adding different noise realizations to the median beat

⁴SBDNR and RDO: Simulation Unbounded Different Noise Realizations and Randomizations of Dipole Orientation

⁵SBDNR and RDO: Simulation Unbounded Different Noise Realizations and Randomizations of Dipole Orientation

⁶BTB: Beat-to-beat, estimated by computing beat-to-beat variation in dipole location

^aNoise estimated at 14 μV



Lesvos Island - Plomari (Edition: A&E Moliviatis)

Chapter 7

Impact and Future Direction

7.1 Significance and Relevance of the Research

The success of trans-catheter radio-frequency ablation for ventricular arrhythmias using the conventional mapping techniques is no more than 70% even in the hands of the best operators [83].

We believe that our algorithm will enable cardiac electrophysiologists to use the trajectory of the equivalent cardiac dipole generator to guide the catheter to the focus of the arrhythmia and deliver curative radio-frequency energy to the site with much greater accuracy and less discomfort to the patient. Successful catheter ablation of ventricular tachycardia will have a significant impact in reducing sudden cardiac death in our society, use of defibrillators, and potentially harmful antiarrhythmic medications. This will have important implications in the patients quality of life and prognosis, as well as significant economic implications.

The ability to perform three dimensional mapping and view the arrhythmia in real-time represents a step ahead from the standard fluoroscopic two-dimensional imaging or activation mapping. Analysis of the dipole trajectory will identify the optimum location for delivery of radio-frequency energy (e.g. at the position of the

dipole corresponding to the point in time when the goodness of fit parameter is minimized) and will enable the direction of the ablation catheter to the site of origin of the arrhythmia.

The stability of the ECG inverse solution is verified by examining the following criteria: (i) stability of the RNMSE in an anatomical area around the best solution, (ii) stability of the χ^2/dof in an anatomical area around the best solution, (iii) stability of the prediction error in terms of the size of the distributed source and the effect in the uncertainty in the best solution, around the best solution, (iv) stability of the error in the position (dr) of the best solution.

7.2 Advantages and Disadvantages of our System Compared with Commercial Systems

Once the mapping catheter is placed inside the heart, its location can be determined through use of an approach that we describe later on in this chapter. So, if the operator moves the catheter from one position in the heart to another, its position and movement (trajectory) can be tracked.

The guidance of the ablation catheter in the heart will not be anymore by means of a two-dimensional fluoroscopic image as a result of the three-dimensional projection of the cardiac anatomy. The identification of an area of cardiac tissue that could potentially be the reentrant-loop, will allow cardiac electrophysiologists to revisit the site and deliver additional radio-frequency energy, even if the tachycardia is not inducible any more.

The choice for the anatomical reference (recording catheter that will resolve the location of the ablation catheter as well guide it towards the ablation site) can be either intracardiac [53,81] or outside the body [24,70]. The advantage of an internally placed catheter is that it compensates for patient position and the movement of the

heart within the chest such as occurs during respiration, as well as providing an additional catheter that can be used to pace or record electrograms. The disadvantage of using an internal reference catheter is that dislodgment of the catheter from its fixed position will result in a shift in the relative location of the mapping catheter and consequently in a requirement to recreate the map from the beginning. In contrast, reference electrodes positioned outside the body may eliminate the problem of movement of the reference catheter and also correct for patient movement, but may only partially compensate for respiration.

7.2.1 Impact on Quality of Life and the Economics

Most arrhythmias that are treated today with a catheter ablation procedure do impair functional capacity and the patient's sense of well being. The quality of life also improved after radio-frequency ablation in patients that had received an implantable cardioverter defibrillator [87]. Except for ablation of ventricular tachycardia and modification or ablation of the atrio-ventricular node, radio-frequency ablation can be performed on an out-patient basis. The total charges for an out-patient ablation procedure are typically US\$ 10,000 to US\$ 12,000 [37]. In addition, successful catheter ablation leads to a reduction in the number and duration of patient hospitalizations. All the above have significant implications for the already heavy health-care cost of this patient population.

Radio-frequency ablation for a variety of supra-ventricular arrhythmias is curative and has been demonstrated to improve the health-related quality of life [8]. Accessory pathway ablation has been demonstrated to be cost effective in patients with paroxysmal supraventricular tachycardia or atrial fibrillation. Alternatively, ablation procedures have been found to result in long-term reductions in health care expenditures, i.e the cost of radio-frequency ablation is less than the long-term costs associated with management of paroxysmal supraventricular tachycardia that is refractory

to treatment with drugs.

7.2.2 Impact on the Use of the Cardioverter-defibrillator and Anti-arrhythmic Drugs

Because the recurrence of an ablated ventricular tachycardia or the onset of a new ventricular tachycardia may be fatal, radio-frequency ablation is rarely used as the sole therapy for ventricular tachycardia. Instead, it is usually used in patients with coronary artery disease as an adjunct to an implantable cardioverter-defibrillator or, less commonly, to anti-arrhythmic drug therapy.

Successful radio-frequency ablation in patients that have received an implantable cardioverter-defibrillator will lead firstly to a reduction of the frequency of shocks for those patients (and improvement of patient acceptance of this therapeutic modality), and secondly to a decrease in the need of anti-arrhythmic medications with their potentially pro-arrhythmic and/or other side effects [87].

7.2.3 Impact on the Treatment of Multiple VT Morphologies

In selected patients with ventricular tachycardia and prior infarction, the long-term success rate of radio-frequency ablation of ventricular tachycardia is up to 70%, with serious complications in less than 2% of patients [6,39]. These success rates refer only to the particular ventricular tachycardia targeted for ablation, not to all ventricular tachycardias in a given patient. Use of our technique will reduce the time required to perform the mapping while the patient is in VT and make it more tolerated by the patient. Thus, attempts to treat more than one VTs may become more feasible and well received by the patient and consequently more appealing to the electrophysiologist.

7.2.4 Impact on Reducing Exposure to Radiation

Radio-frequency ablation procedures require fluoroscopy, and the amount of radiation exposure depends on the equipment and the technique used. Acute skin injury is rare and can be avoided by minimizing radiation exposure [60]. In one study, it was estimated that each hour of fluoroscopy was associated with a life-time risk of fatal cancer of 0.1% and a risk of genetic defect in the patient's offspring of 20 per 1 million births [9]. Although radio-frequency ablation usually can be accomplished with less than 60 minutes of fluoroscopy, reduced exposure time would make the procedure more applicable to certain patients (i.e children).

In addition, and quite importantly reduced radiation exposure of the operator electrophysiologist will be a great benefit.

7.3 Other Arrhythmias That Can be Treated With Radio-frequency Ablation

As success rates increase and the risk of complications becomes lower, catheter ablation is becoming an increasingly popular procedure of treating life threatening cardiac arrhythmias. To further improve the success rate and make the overall procedure faster and easier, catheter ablation is also indicated in the following cardiac arrhythmias.

7.3.1 Paroxysmal Supraventricular Tachycardia

The most common mechanism of paroxysmal supraventricular tachycardia is atrioventricular nodal reentry, which is responsible for approximately 60 to 65 percent of the cases. In most patients with this arrhythmia, posterior atrio-nodal input to the atrio-ventricular node serves as the anterograde limb, or "slow pathway", of the

reentry circuit, and anterior atrio-nodal inputs serve as the retrograde limb, of “fast pathway”. Atrioventricular nodal reentrant tachycardia can be eliminated by radio-frequency ablation of either the fast or the slow pathway, but without eliminating the risk of inadvertently creating atrio-ventricular block. Yet, atrio-ventricular nodal reentrant tachycardia and accessory pathway tachycardias are ideally suited for radio-frequency ablation, because critical components of their reentry circuits can usually be permanently eliminated with discrete applications of radio-frequency current.

7.3.2 The Wolff-Parkinson-White Syndrome

Wolff-Parkinson-White (WPW), refers to abnormal electrical activation of the ventricles via an accessory pathway, other than the AV node, that connects the atria with the ventricles. In the past, most patients with Wolff-Parkinson-White syndrome were treated with drugs and surgical ablation was performed only in patients whose arrhythmias were refractory to drug treatment or were life threatening. Today, radio-frequency ablation has eliminated the need for surgical ablation in almost all patients with WPW and has decreased the need for anti-arrhythmic drug therapy in most of the patients.

7.3.3 Atrial Flutter

Type I atrial flutter (generated by a large, counterclockwise reentry circuit in the right atrium), that is the most common variety of atrial flutter, can be successfully eliminated by radio-frequency ablation of a critical isthmus of tissue between the tricuspid annulus and the inferior vena cava. Because of high success rate and low risk of complications, radio-frequency ablation of type I atrial flutter is appropriate not only in patients with atrial flutter that is refractory to drug treatment, but also in patients who desire an alternative to anti-arrhythmic drug therapy or repeated electrical cardioversion. However, there are cases of atypical atrial flutter that arise

in the right or left atrium and are difficult to map and ablate. Therefore, because of the lower probability of success in such cases, radio-frequency ablation is usually reserved for patients in whom atrial flutter is refractory to drug therapy.

7.3.4 Atrial Fibrillation

An uncontrolled ventricular rate during atrial fibrillation is often responsible for uncomfortable symptoms, functional limitation, and cardiomyopathy induced by tachycardia. If the ventricular rate cannot be controlled with drug therapy, radio-frequency energy can be used either to ablate or modify the atrioventricular node. The goal of the atrioventricular node modification is to control the ventricular rate without creating high-grade atrioventricular block. Symptoms, functional capacity, and left ventricular function improve after either radio frequency ablation or modification of the atrio-ventricular node in patients with atrial fibrillation [52].

7.3.5 Idiopathic Ventricular Tachycardia

The two most common varieties of idiopathic ventricular tachycardia are ventricular tachycardia arising in the right ventricular outflow tract [40] and verapamil-responsive left ventricular tachycardia [54]. When there is only one site of origin of ventricular tachycardia, as is usually the case in patients with idiopathic ventricular tachycardia, radio-frequency ablation is often curative. Because of its high efficacy, and low risk, radio-frequency ablation of idiopathic ventricular tachycardia may be appropriate when the arrhythmia is refractory to drug treatment.

7.4 Proposed Studies

7.4.1 Saline Tank Studies

In vitro studies, conducted in a saline tank using an anatomically and geometrically realistic saline torso tank and current dipole sources, will be proven very insightful. The body surface potentials will be measured over the chest. These potentials will be used to identify the position and strength of the dipoles that were employed to generate those potentials. Thus, the ability of our algorithm in localizing multiple simultaneously active and spatially separated electrical current sources will be tested. In addition the robustness of our algorithm in various signal-to-noise ratio conditions will be verified.

Specifically, use of up to 150 locations of body surface potentials, obtained from an array of electrodes located over the torso surface, will be used to identify the location, magnitude and orientation of known, multiple spatially separated electric dipole sources. The effects of electrode location and electrode number reduction as well as measurement of noise in the ability of our algorithm to indicate and discriminate multiple dipoles will be verified. Thus, we will evaluate the in-vitro sensitivity and specificity of our algorithm under carefully designed simulated conditions.

7.4.2 Realistic Anatomic Geomertry Computer Simulations

The accuracy and robustness of our algorithm in identifying the equivalent dipole generator should be tested and verified in a finite element model that includes tissue inhomogeneities as well as detailed anatomic geometry. A fully detailed model of the human torso will serve as a complete and accurate forward model. Use of a single dipole source in the forward problem will allow the following to the inverse algorithm: (i) the error in the location of the equivalent dipole due to the assumption of the homogeneous volume conductor, (ii) individual contribution of the various

anatomical compartments to the positional error, (iii) sensitivity of the solution on the number of electrodes employed, as well as percentage error in the position of the equivalent dipole as a function of percentage error in the accuracy with which the position of each electrode is measured.

Use of two separated dipole sources will serve as a good model to verify the resolution of the inverse algorithm. Specifically, (i) the minimum distance that the two dipoles can be separately identified as a function of their relative size, (ii) the minimum distance that the two dipoles can be identified separately as a function of their relative orientation.

The significance of systematic error and measurement noise in the accuracy of the equivalent dipole localization should also be evaluated. An estimate of the systematic error introduced by use of the infinite homogeneous volume conductor versus the detailed realistic anatomic geometry may be introduced in the estimation of χ^2/dof , thus making it a more objective goodness of fit criterion.

Finally, signal to noise studies will indicate the minimum size of the activation front necessary to give rise to potentials that can be detected at the body surface. As part of these studies the size of the source may be approximated with approaches similar to the ones presented in this thesis.

7.4.3 Clinical Studies

Finally, a system to verify in clinical studies the applicability and accuracy of our algorithm in patients scheduled to undergo catheter ablation procedure should be built.

Such as a system would include a personal computer that would perform the following tasks: (i) multi-channel signal acquisition and display, (ii) digital signal processing, for estimation of the equivalent dipole at each point in the cardiac cycle (iii) estimation of the statistical properties of the fit and finally (iv) display of the

trajectory and the spatial error of the equivalent dipole.

Following induction of ventricular tachycardia a few cycles only should be recorded in order to identify the site of origin of the arrhythmia. The electrical location of the catheter will be identified by applying a low amplitude signal to the catheter electrode and using the same algorithm to locate the catheter tip. Comparison of the site selected by our algorithm will be made with the site that the electrophysiologist will initially identify (in terms of catheter tip location) as well as to the site that, following ablation, leads to the abolition of inducibility of the ventricular tachycardia.

This clinical study will provide a direct head to head comparison between (i) the site that when ablated leads to termination of VT inducibility at electrophysiologic testing, (ii) the site that is selected to be ablated and (iii) the site that our algorithm chooses as the optimal one.

7.4.4 Guiding the Catheter to the Ablation Site

The localization of the tip of the ablation catheter will be achieved through the delivery at its tip of a low amplitude ($\approx 5\mu A$), high frequency (up to 2KHz) signal. Two kilohertz may be a good compromise between something that is high enough to be easily separated by demodulation from the ECG signal and other interference, and low enough not to present serious cross-talk and loading effects of stray capacitance. These pulses are known to have no biological effect and are substantially below the recommended safety level of $10\mu A$ for signals below 1.0KHz.

Although in chapter 3, we showed in Figures 3-3 to 3-4 that the estimation of the equivalent dipole was not affected by the orientation of the dipole in the forward problem, caution should be taken when a higher degree of complexity forward problem is used, such the real torso is used, where tissue inhomogeneities are expected to contribute to the systematic error more than the transition from the zero- to first order model presented in chapter 3. Thus, it may be required that more attention

should be given to the orientation of the tip of the catheter.

An approach to overcome potential difficulties to guide to the tip of the catheter to the ablation site due to the sensitivity of the inverse algorithm to the direction of the tip of the catheter, the current pulses may be orthogonal, with the polarity inverted every other sample. Prior knowledge of the timing and the polarity of a delivered pulse will be used in the demodulation. Prior to demodulation the two components of signal superposition (the underlying electrophysiological signal generated by the heart and field induced by the current burst sequence), will be separated. The best way to separate these signals is based on their frequency. For that purpose there is going to be a high-pass filter hardware block that will extract the induced field signals modulated by the torso inhomogeneities, and a low-pass filter that will extract the physiologic signal.

We are going to use a specially designed catheter able to deliver orthogonal (or any other configuration from which an orthogonal basis can be extracted) current pulses. The assumption made is that if the tip of the catheter was on the top of the dipole attributed to the cardiac dipole at the instant we want to ablate, then the distortion because of tissue inhomogeneities etc., would have the same effect as in the case of the cardiac generator, and the potentials that the tip would generate in the surface would be the same with the potentials recorded due to the cardiac dipole.

The process of guiding the tip of the catheter to the ablation site is summarized in the following steps:

Step 1. Find the appropriate time, through the use of the algorithm previously described, during the cardiac cycle at which the arrhythmia is highly localized. For this time instant we find the positional (x_p, y_p, z_p) parameters attributed to the equivalent cardiac dipole (p_x, p_y, p_z) .

Step 2. From the arbitrary position that the tip of the catheter currently holds pace and use the body surface recorded potentials to find the position of the tip

(x_c, y_c, z_c) .

Step 3. Deliver from the tip of the catheter current pulses, such that they simulate size and orientation of the cardiac dipole moment components (p_x, p_y, p_z) at the instant we want to ablate. This can be done by scaling appropriately the current in each of the orthogonal leads.

Step 4. Use the potentials obtained from the the cardiac dipole at the instant you want to ablate, to fit the two unknowns: (i) the direction and (ii) the step you want to make in order to move the tip of the catheter to get it on the top of the position of the cardiac dipole.

However, there is still one more problem to be solved; the tip of the catheter has an arbitrary direction. In other words the x-axis of the catheter will not be aligned with the x-axis of the main coordinate system. In order to solve this problem we are going to deliver sequential pulses from each of the orthogonal leads of the catheter and identify them. If for example, we deliver a pulse sequence from the catheter x-lead (on the catheter coordinate system), and we call this c_x , then, by applying the inverse algorithm we will obtain three solutions c_{xx}, c_{xy}, c_{xz} . Repeating the same procedure for each of the other orthogonal leads of the catheter c_y and c_z , and claiming the orthogonality relation between the catheter leads we are able to obtain the projections of c_x, c_y, c_z on the major axis.

This is different from delivering arbitrary current pulses and try to match the tip of the catheter to the cardiac dipole. The delivery of the p_x, p_y, p_z from the tip of the catheter may be done sequentially (and superimpose the potentials), so that if it's done fast enough, the catheter doesn't move.

There are three challenges guiding the ablation catheter to the ablation site. The first has to do with how close a representation to the dipole model is a current pulse delivered at the tip of the catheter, and similarly for the cardiac cycle. The second has to do with the effect that local tissue inhomogeneities (that lead to variations

in conductivity) may have in guiding the catheter to the site. The third has to do with how close can someone deliver current pulses from the tip of the catheter to approximate the cardiac dipole moment components. For the first one, we will assume that the physical model of a catheter delivering current pulses in a passive medium, will be a good approximation of the equivalent cardiac dipole when the arrhythmia is highly localized. The second one can be overcome by the simple notion, that the closer the catheter tip gets to the ablation site, the lesser such differences will have an effect. The third one will be an engineering issue and its precision and limitations will be one of the factors that will influence the accuracy of this procedure.

7.4.5 Spatial Information About the Heart and the Electrodes

Since any source of error in the forward problem will affect the inverse solution, it is necessary to minimize the effect of such factors as the spatial properties (position and dimensions) of the heart and the position of the measurement electrodes in the estimation of the equivalent dipole. The above difficulties could be overcome by use of Magnetic Resonance Imaging (MRI) anatomical information of a human thorax. This 3-dimensional representation of the thorax when viewed on the computer screen, firstly will allow the definition of the heart boundaries inside the thorax. Secondly, it will allow the operator to mark on the screen the position of the electrodes on the thorax and thus will make the coordinates of the electrodes immediately available. The variation in human thorax size may be overcome by making available different size thoraces and loading only the most appropriate one.

7.4.6 Impact on Differentiating Between Focal Versus Reentrant Arrhythmias

The differentiation of focal from reentrant arrhythmias may be based on the fact that if the entire circuit is mapped the reentrant arrhythmia will be characterized by a range of activation times that will equal the cycle length of the tachycardia and also by close spatial association between the arbitrary “early” and “late” sites. In contrast, a focal arrhythmia will be characterized by a total range of activation times that are usually shorter than the cycle length of the tachycardia and a well defined early activation site surrounded by later activation sites.

For focal arrhythmias, the earliest activation site is usually defined as the target site for ablation. Thus, following identification of a region with early activity, a high density map of this area can be acquired to precisely define the earliest activation site. This site is defined as earliest only when surrounded by later activated sites in all directions.

7.4.7 Ethical Aspects of the Proposed Research

The application of surface electrodes and recording of the electrocardiograms should be a risk-free procedure. This protocol has no additional significant risk above that of the clinical procedure the patient is undergoing as part of his/her clinical care.

The purpose of the study is to compare a new methodology in guiding cardiac electrophysiologists to the ablation site in the heart by using surface ECG signals. Our approach in identifying that site is too new to be used at present as a reliable method of guiding the ablation catheter. The primary benefit of patients in this study is the knowledge that they are contributing to the development of a new minimally invasive, fast and reliable means of guiding the ablation catheter to the ablation site.

7.4.8 Experimental Problems of Clinical Study

Among the experimental difficulties estimate to be encountered are the following: (i) Noise-reduction in individual electrodes, (ii) motion artifact from patient movement, (iii) obtaining anatomical information for each patient. Analysis will be done off-line and data acquisition is expected to be a smooth task.

During the first phase of the clinical study the system will be used only for ECG signal recording, while the analysis will be done off-line. Thus, it will not be possible to compare the coincidence of site that the algorithm identified to be ablated with the site that was chosen by the electrophysiologist to be ablated, should ablation not abolish the inducibility of the VT.

7.4.9 Problems in Defining an Absolute Reference Point for Activation Data Recorded During Ventricular Tachycardia

It is frequently difficult to determine the origin of ventricular tachycardia from surface ECG signals. This obvious empirical choice, of using the “onset” of the QRS complex, to determine where tachycardia arises from, although it has been widely subscribed to, assumes that local activation times can be identified (i.e. through early activation analysis), however it remains to be determined how global ventricular activation (that the recorded surface ECG signal represents) relates to local activation.

On the other hand, if we adhere to the viewpoint that tachycardia is present, then continuous electrical activity must be present somewhere. Using intracardiac electrograms to define the activity in any particular area as early or late is therefore clearly arbitrary, and is related to the point of view from which the observer wishes to view the reentrant loop. In this case, an attempt is made to record an area of local depolarization during ventricular tachycardia that precedes the onset of global

ventricular depolarization as evidenced by surface leads.

Alternatively, it is common that potentials are recorded, that span diastole between consecutive QRS complexes (Figure 5-7). In the theoretical case of a small, stable reentry circuit, presystolic (late diastolic) electrograms are also recorded from sites in the circuit near the “circuit exit” (Figure 2-5), where excitation fronts leave the circuit to propagate through the ventricles. At sites more proximal to the reentry path, depolarization occurs earlier in diastole. The most proximal sites in the circuit are activated shortly after the wave front has propagated out of the circuit, and electrograms occur during inscription of the QRS complex. A semantic problem then arises to whether these potentials should be considered late potentials from the previous cycle or very early potentials from the following cycle. However, in a theoretical case of reentry in a structurally normal ventricle, electrical activation that occurs after the end of the QRS complex and before the subsequent QRS onset arises only from the reentry circuit. While diastolic potentials are not easily detected in the surface ECG, intracardiac signals may provide clear evidence of their presence and timing. It may be that the inverse algorithm could be applied to identify the origin of these potentials in the heart [81].

7.4.10 Other Study Issues

The approach that we are pursuing involves determining the position of the localized area of the arrhythmia within the heart by comparing the body surface potential distribution generated by a current source applied to the catheter within the heart, with the potential distribution generated by the heart’s spontaneous electrical activity during the arrhythmia. In this approach both the catheter current source and the arrhythmogenic electrical source will be modeled as a moving dipole in a volume conductor. The advantage of our method lies in the fact that since the localization of the tip of the catheter will be achieved by use of the same inverse algorithm

used in the cardiac dipole localization, effects of such distortion as the effects of inhomogeneity and tissue conductivity, boundary effects as well as effects of realistic anatomic geometry will precisely cancel. However, we will not be able to verify this at the present phase of the project.



Lesvos Island - Sun-set (Edition: A&E Moliviatis)

Appendix A

Special Case

The question of the uniqueness of the inverse solution and the related problem of its sensitivity to the presence of noise are particularly difficult to analyze in the context of the dipole localization. For example because of the highly non-linear character of the χ^2 , one often finds more than one minimum in the optimization process. While one particular minimum may yield an approximation for the dipole parameters (that are possibly distorted because of model inaccuracies), the others may not have any significance with regard to the actual physiological generator. This can be the case even when the value of χ^2 obtained at these minima is relatively small. An example to the problem of convergence to unrealistic values is presented with the following case, using the Davison-Fletcher-Powell algorithm, where we have assumed the *true minimum* to be at:

$$(0.000000, 0.000000, 10.000000, 0.000000, 0.000000, 0.000000)$$

and the *starting vector* to be:

$$(0.000000, 0.000000, 15.000000, 1.404657, 0.186603, 4.751522)$$

The algorithm performed

$$Iterations : 439, \quad Func.eval : 473, \quad Deriv.eval : 439$$

and converged to the *solution vector*:

(122463.648438, 250500.437500, 389141.562500, -408.795441, 184.406891, 9.710435)

with χ^2/dof : 0.0663267 where, *dof* stands for degrees of freedom.

For the case above the potential for example at 5 of the 60 electrode sites because of the *true minimum* is :

(0.00419991137, -0.00404769601, -0.00415986078, -0.00419965386, -0.00423579989)

If we now take the *solution vector* and use it as a *true minimum* we obtain the potential at the same 5 sites we obtain:

(0.00329322764, -0.00402652938, -0.00309846294, -0.00328727486, -0.0035313305)

We statistically compared the values of the potentials generated by the *true minimum* and the *solution vector* (site by site for all 60 sites). Assuming non-normal distributions of the potentials we used the Wilcoxon rank-sum test to test for significant differences. We found that $Z=0.036808$ ($p=0.970638$), signifying the observation that the two potential distributions are not statistically different.

This example demonstrates that it is very possible for the optimization algorithms to converge to solutions that are physiologically unrealistic. Thus, use of constraints (i.e. spatial) on the accepted solutions will overcome such a problem.

Bibliography

- [1] Abildskov, J, M Burgess, R Lux and et al. Experimental evidence for regional cardiac influence in body surface isopotential maps of dogs. *Circ Res*, 38:386–391, 1976.
- [2] Acton, F. *Numerical Methods That Work*. Mathematical Association of America, Washington, 1990.
- [3] Ambroggi, LD, E Aime, C Ceriotti and et al. Mapping of ventricular repolarization. *Circulation*, 96:4314–4318, 1997.
- [4] Bard, Y. *Interpretation of the estimates*. Academic Press, Inc, New York, 1974.
- [5] Blanchard, S, W Smith, J RJ Damiano, D Molter, R Ideker and J Lowe. Four digital algorithms for activation detection from unipolar epicardial electrograms. *IEEE Trans on Biomed Eng*, 36:256–261, 1989.
- [6] Bogun, F, M Bahu, B Knight and et al. Comparison of effective target sites that demonstrate concealed entrainment in patients with coronary artery disease undergoing radiofrequency ablation of ventricular tachycardia. *Circulation*, 95:183–190, 1997.
- [7] Brent, R. *Algorithms for Minimization without Derivatives*. Rentice Hall, Englewood Cliffs, NJ, 1973.
- [8] Bubien, R, S Knotts-Dolson, V Plumb and G Kay. Effect of radiofrequency catheter ablation on health-related quality of life and activities of daily living in patients with recurrent arrhythmias. *Circulation*, 94:1585–1591, 1996.
- [9] Calkins, H, L Niklason, J Sousa, R el Atassi, J Langberg and F Morady. Radiation exposure during radiofrequency catheter ablation to accessory atrioventricular connections. *Circulation*, 84:2376–2382, 1991.
- [10] Calkins, H, E Prystowski, M Carlson, L Klein, J Saul and P Gillette. Temperature monitoring during radiofrequency catheter ablation procedures using closed loop control. *Circulation*, 90:1279–1286, 1994.
- [11] cardiac arrhythmia suppression trial (CAST) investigators, T. Preliminary report: effect of encainide and flecainide on mortality in a randomized trial of arrhythmia suppression after myocardial infarction. *N Engl J Med*, (321):406–412, 1989.

- [12] Cox, J. Patient selection criteria and results of surgery for refractory ischemic ventricular tachycardia. *Circulation*, 79(Suppl I):I163–I177, 1989.
- [13] Davison, W. Variable metric method for minimization. aec research and development report. *A.E.C. Research and Development Report, ANL-5900 (Rev)*, 1959.
- [14] de Bakker, J, F van Capelle, M Janse, N van Hemel, R Hauer, J Defauw, F Vermeulen and P de Wekker. Macroreentry in the infarcted human heart: mechanism of ventricular tachycardias with a focal activation pattern. *J Am Coll Cardiol.*, 18:1005–1014, 1991.
- [15] Eckstein, R. Coronary interarterial anastomoses in young pigs and mongrel dogs. *Circ Res*, 2:460, 1954.
- [16] Einthoven, W. The different forms of the human electrocardiogram and their signification. *Lancet*, pp. 853–861, 1912.
- [17] Fletcher, R and C Reeves. Function minimization by conjugate gradients. *Comput J*, 7:149, 1964.
- [18] Flowers, N and L Horan. *Body surface potential mapping*. WB Saunders, Philadelphia, 1995.
- [19] for the Electrophysiologic Study versus Electrocardiographic monitoring Investigators, JM. A comparison of electrophysiologic testing with holter monitoring to predict antiarrhythmic-drug efficacy for ventricular tachycardias. *N Engl J Med*, (329):445–458, 1993.
- [20] Franzone, P, L Guerri and B Taccardi. Potential distributions generated by point stimulation in a myocardial volume: Simulation studies in a model of anisotropic ventricular muscle. *J Cardiovasc Electrophysiol*, 4:438–458, 1993.
- [21] Gabor, D and C Nelson. Determination of the resultant dipole of the heart from measurements on the body surface. *J Appl Physics*, 25:413–416, 1954.
- [22] Gepstein, L, G Hayam and S Ben-Haim. Activation-repolarization coupling in the normal swine endocardium. *Circulation*, 96:4036–4043, 1997.
- [23] Geselowitz, D and H Ishiwatari. *A theoretical study of the effect of the intracavitary blood mass on the dipolarity of an equivalent heart generator*. North Holland Publishing Co, Amsterdam, Holland, 1965.
- [24] Gornick, C, S Stuart, B Pederson, J Hauck, J Budd and J Schweitzer. Validation of a new noncontact catheter system for electroanatomic mapping of left ventricular endocardium. *Circulation*, 99:829–835, 1999.
- [25] Greensite, F and G Huiskamp. An improved method for estimating epicardial potentials from the body surface. *IEEE Trans Biomed Eng*, 45(1):98–104, 1998.

- [26] Gulrajani, R, H Pham-Huy, R Nadem and et al. Application of the single moving dipole inverse solutions to the study of the wpw syndrome in man. *J Electrocardiol*, 17:271–288, 1984.
- [27] Gulrajani, R, F Roberge and P Savard. *The inverse problem of electrocardiography*. Pergamon, Oxford, England, 1989.
- [28] H Nakagawa, WJ. Use of a three-dimensional, nonfluoroscopic mapping system for catheter ablation of typical atrial flutter. *PACE*, 21:1279–1286, 1998.
- [29] Harrison, L, R Ideker, W Smith, G Klein, J Kasell, A Wallace and J Gallaher. The sock electrode array: A tool for determining global epicardial activation during unstable arrhythmias. *PACE*, 3:531–540, 1980.
- [30] He, B and R Cohen. Body surface laplacian ecg mapping. *IEEE Trans Biomed Eng*, 39:1179–1191, 1992.
- [31] He, B and R Cohen. Body surface laplacian mapping of cardiac electrical activity. *Am J Cardiol*, 70:1617–1620, 1992.
- [32] He, B, E Harasawa, T Alkasab and et al. A high resolution cardiac mapping system. In: *Proc of Ann Int Conf of IEEE Eng Med Biol Soc*, volume 14, pp. 812–814. 1992.
- [33] He, B, D Kirby, T Mullen and R Cohen. Body surface laplacian mapping of cardiac excitation in intact pigs. *PACE*, 16, Part I:1017–1026, 1993.
- [34] Ideker, R, J Bandura, R Larsen, J Cox, F Keller and D Brody. Localization of heart vectors produced by epicardial burns and ectopic stimuli. *Circ Res*, 36:105–112, 1975.
- [35] Janse, M and A Kleber. Electrophysiological changes and ventricular arrhythmias in the early phase of regional ischemia. *Circ Res*, 49:1069, 1981.
- [36] Janse, M and A Wit. Electrophysiological mechanisms of ventricular arrhythmias resulting from myocardial ischemia and infarction. *Physiol Rev*, 69:1049–1169, 1989.
- [37] Kalbfleisch, S, R el Atassi, H Calkins, J Langberg and F Morady. Safety, feasibility and cost of outpatient radiofrequency catheter ablation of accessory atrio-ventricular connections. *J Am Coll Cardiol*, 31:567–570, 1993.
- [38] Kaltenbrunner, W, R Cardinal, M Dubuc, M Shenasa, R Nadeau, G Tremblay, M Vermeulen, P Savard and P Page. Epicardial and endocardial mapping of ventricular tachycardia in patients with myocardial infarction: is the origin of the tachycardia always subendocardially localized? *Circulation*, 84:1058–1071, 1991.

- [39] Kim, Y, G Sosa-Suarez, T Trouton, S O’Nunain, S Osswald, B McGovern, J Ruskin and H Garan. Treatment of ventricular tachycardia by transcatheter radiofrequency ablation in patients with ischemic heart disease. *Circulation*, 89:1094–1102, 1994.
- [40] Klein, K, H Shih, F Hackett, D Zipes and W Miles. Radiofrequency catheter ablation of ventricular tachycardia in patients without structural heart disease. *Circulation*, 85:1666–1674, 1992.
- [41] Kottkamp, H, G Hindricks, G Breithardt and M Borggrefe. Three-dimensional electromagnetic catheter technology: Electroanatomical mapping of the right atrium and ablation of ectopic atrial tachycardia. *J Cardiovasc Electrophysiol*, 8:1332–1337, 1997.
- [42] Langberg, J, H Calkins, Y Kim and et al. Recurrence of conduction in accessory atrioventricular connections after initially successful radiofrequency catheter ablation. *J Am Coll Cardiol*, 19:1588–1592, 1992.
- [43] Langberg, J, M harvey, HCR el Atassi, S Kalbfleish and F Morady. Titration of power output during radiofrequency catheter ablation of atrioventricular nodal reentrant tachycardia. *Pacing Clin Electrophysiol*, 16:465–470, 1993.
- [44] Lee, M, F Morady and AK et al. Catheter modification of the atrioventricular junction with radiofrequency energy for control of atrioventricular nodal reentry tachycardia. *Circulation*, 83:827–835, 1991.
- [45] Ljung, L. *Asymptotic distribution of parameter estimates*. PTR Prentice Hall Information and System Sciences Series, Englewood Cliffs, NJ, 1987.
- [46] Macleod, R, M Gardner, R Miller and B Horacek. Application of an electrocardiographic inverse solution to localize ischemia during coronary angioplasty. *J Cardiovasc Electrophysiol*, 6:2–18, 1995.
- [47] Miller, J, M Kienzle, A Harken and M Josephson. Subendocardial resection for ventricular tachycardia: predictors of surgical success. *Circulation*, 70:624–631, 1984.
- [48] Miller, W and D Geselowitz. Simulation studies of the electrocardiogram i. the normal heart. *Circ Res*, 43:301–315, 1978.
- [49] Mirvis, D and M Hollrook. Body surface distributions of repolarization potentials after acute myocardial infarction. iii. dipole ranging in normal subjects and in patients with acute myocardial infarction. *J Electrocardiol*, 14:387–98, 1981.
- [50] Mitrani, R, L Biblo, M Carlson, K Gatzoylis, R Hentorn and A Waldo. Multiple monomorphic ventricular tachycardia configurations predict failure of antiarrhythmic drug therapy guided by electrophysiologic study. *J Am Coll Cardiol*, 22:1117–1122, 1993.

- [51] Morady, F, M Harvey, S Kalbfleisch, R El-Atassi, H Calkins and J Langberg. Radiofrequency catheter ablation of ventricular tachycardia in patients with coronary artery disease. *Circulation*, 87:363–372, 1993.
- [52] Morady, F, C Hasse, S Strickberger and et al. Long term follow-up after radiofrequency modification of the atrioventricular node in patients with atrial fibrillation. *J Am Coll Cardiol*, 29:113–121, 1997.
- [53] Nademanee, K and E Kosar. A nonfluoroscopic catheter-based mapping technique to ablate focal ventricular tachycardia. *PACE*, 21:1442–1447, 1998.
- [54] Nakagawa, H, K Beckman, J McClelland and et al. Radiofrequency catheter ablation of idiopathic left ventricular tachycardia guided by a purkinje potential. *Circulation*, 88:2607–2617, 1993.
- [55] Natale, A, L Breeding, G Tomassoni, K Rajkovich, M Richey, S Beheiry, K Martinez, L Cromwell, B Wides and F Leonelli. Ablation of right and left ectopic atrial tachycardias using a three-dimensional nonfluoroscopic mapping system. *Am J Cardiol*, 82:989–992, 1998.
- [56] Nath, S, J Whayne, S Kaul, N Goodman, A Jayaweera and D Haines. Effects of radiofrequency catheter ablation on regional myocardial blood flow: possible mechanism for late electrophysiological outcome. *Circulation*, 89:2667–2672, 1994.
- [57] Nelder, J and R Mead. A simplex method for function minimization. *Comput J*, 7:308–313, 1965.
- [58] Oster, H, B Taccardi, R Lux, P Ershler and Y Rudy. Noninvasive electrocardiographic imaging. reconstruction of epicardial potentials, electrograms and isochrones and localization of single and multiple electrocardiac events. *Circulation*, 96:1012–1024, 1997.
- [59] Oster, H, B Taccardi, RL Lux and et al. Noninvasive electrocardiographic imaging: Characterization of intramural myocardial activation. *Circulation*, 97:1496–1507, 1998.
- [60] Park, T, J Eichling, K Schectman, B Bromberg, J Smith and B Lindsay. Risk of radiation induced skin injuries from arrhythmia ablation procedures. *Pacing Clin Electrophysiol*, 19:1363–1369, 1996.
- [61] Paul, T, J Moak and CM et al. Epicardial mapping: How to measure local activation? *PACE*, 13:285, 1990.
- [62] Plonsey, R and D Fleming. McGraw-Hill, New York, 1969.
- [63] R, F and P MJD. A rapidly convergent descent method for minimization. *Comput J*, 6:163, 1963.

- [64] Rosenbaum, D, D Wilber, J Smith, D Du, J Ruskin and H Garan. Local activation variability during monomorphic ventricular tachycardia in the dog. *Cardiovas Res*, 26:237–243, 1992.
- [65] Rosner, B. *Percentage points of the chi-square distribution*. Wadsworth Publishing Company, Belmont, CA, 1995.
- [66] Rudy, Y and B Messinger-Rapport. The inverse solution in electrocardiography: solutions in terms of epicardial potentials. *Crit Rev Biomed Eng*, 16:215–268, 1988.
- [67] Rudy, Y and H Oster. The electrocardiographic inverse problem. *Crit Rev Biomed Eng*, 20(1,2):25–45, 1992.
- [68] Rudy, Y and R Plonsey. A comparison of volume conductor and source geometry effects on body surface and epicardial potentials. *Circ Res*, 46:283–293, 1980.
- [69] Savard, P, F Roberge, J Perry and R Nadeau. Representation of cardiac electrical activity by a moving dipole for normal and ectopic beats in the intact dog. *Circ Res*, 46:415–425, 1980.
- [70] Schilling, R, D Davies and N Peters. Characteristics of sinus rhythm electrograms at sites of ablation of ventricular tachycardia relative to all other sites: A non-contact mapping study of the entire left ventricle. *J Cardiovasc Electrophysiol*, 9:921–933, 1998.
- [71] Shah, D, P Jais, M Haissaguerre, S Chouairi, A Takahashi, M Hocini, S Garrigue and J Clementy. Three-dimensional mapping of the common atrial flutter circuit in the right atrium. *Circulation*, 96:3904–3912, 1997.
- [72] Shpun, S, L Gepstein, G Hayam and S Ben-Haim. Guidance of radiofrequency endocardial ablation with real-time three-dimensional magnetic navigation system. *Circulation*, 96:2016–2021, 1997.
- [73] Simmers, T, F Wiittkamp, R Hauer and ER de Medina. In vivo ventricular lesion growth in radiofrequency catheter ablation. *Pacing Clin Electrophysiol*, 17:523–531, 1994.
- [74] SippensGroenewegen, A, H Peeters, E Jessurun and et al. Body surface mapping during pacing at multiple sites in the human atrium. *Circulation*, 97:369–380, 1998.
- [75] Smith, J, E Clancy, C Valeri, J Ruskin and R Cohen. Electrical alternans and cardiac electrical instability. *Circulation*, 77:110–121, 1988.
- [76] Spach, M and R Barr. Analysis of ventricular activation and repolarization from intramural and epicardial potential distributions for ectopic beats in the intact dog. *Circ Res*, 37:830–843, 1975.

- [77] Spach, M, R Barr, C Lanning and et al. Origin of body surface qrs and t wave potentials from epicardial potential distributions in the intact chimpanzee. *Circulation*, 55:266–278, 1977.
- [78] Spach, M and WMI et al. Extracellular potentials related to intracellular action potentials related to intracellular action potentials during impulse conduction in anisotropic canine cardiac muscle. *Circ Res*, 45:188, 1979.
- [79] Stevenson, W. *Catheter mapping of ventricular tachycardia*. WB Saunders, Philadelphia, 1995.
- [80] Stevenson, W. Ventricular tachycardia after myocardial infarction. on arrhythmia surgery to catheter ablation. *J Cardiovasc Electrophysiol*, 6(Pt II):942–950, 1995.
- [81] Stevenson, W, E Delacretaz, P Friedman and K Ellison. Identification and ablation of macroreentrant ventricular tachycardia with the carto electroanatomical mapping system. *PACE*, 21:1448–1456, 1998.
- [82] Stevenson, W, P Friedman and L Ganz. Radiofrequency catheter ablation of ventricular tachycardia late after myocardial infarction. *J Cardiovasc Electrophysiol*, 8:1309–1319, 1997.
- [83] Stevenson, W, P Friedman, D Kocovic, P Sager, L Saxon and B Pavri. Radiofrequency catheter ablation of ventricular tachycardia after myocardial infarction. *Circulation*, 98:308–314, 1998.
- [84] Stevenson, W, P Friedman, D Kosovic, P Sager, L Saxon and B Pavri. Radiofrequency catheter ablation of ventricular tachycardia after myocardial infarction. *Circulation*, 98:308–314, 1998.
- [85] Stevenson, W, H Khan, P Sager and et al. Identification of reentry circuit sites during catheter mapping and radiofrequency ablation of ventricular tachycardia late after myocardial infarction. *Circulation*, 88:1647–1670, 1993.
- [86] Stevenson, W, J Weiss, I Weiner, D Woohlgelernter and L Yeatman. Localization of slow conduction in a ventricular tachycardia circuit: implications for catheter ablation. *Am Heart J*, 114:1253–1258, 1987.
- [87] Strickberger, S, K Man, E Daoud and et al. A prospective evaluation of catheter ablation of ventricular tachycardia as adjuvant therapy in patients with coronary artery disease and an implantable cardioverter-defibrillator. *Circulation*, 96:1525–1531, 1997.
- [88] Taccardi, B. Distribution of heart potentials on the thoracic surface of normal human subjects. *Circ Res*, 12:341, 1963.
- [89] Taccardi, B, E Macchi, R Lux, P Ershler, S Spaggiari, S Baruffi and Y Vyhmeister. Effect of myocardial fiber direction on epicardial potentials. *Circulation*, 90:3076–3090, 1994.

- [90] Tsunakawa, H, G Nishiyama, S Kanesaka and K Harumi. Application of dipole analysis for the diagnosis of myocardial infarction in the presence of left bundle branch block. *J Am Coll Cardiol*, 10:1015–21, 1987.
- [91] Waller, A. On the electromotive changes connected with the beat of the mammalian heart and of the human heart in particular. *Philos Trans R Soc*, B180:169, 1889.
- [92] Waspel, L, R Brodman, S Kim, J Matos, D Johnston, G Scavin and J Fisher. Activation mapping in patients with coronary artery disease with multiple ventricular tachycardia configurations: occurrence and therapeutic implications of widely separate apparent sites of origin. *J Am Coll Cardiol*, 5:1075–1086, 1985.
- [93] Wilber, D, M Davis, D Rosenbaum, J Ruskin and H Garan. Incidence and determinants of multiple morphologically distinct sustained ventricular tachycardias. *J Am Coll Cardiol*, 10:589–591, 1987.
- [94] Worleyand, S, R Ideker, J Mastrototaro, W Smith, J H Vidaillet, P Chen and J Lowe. A new sock electrode for recording epicardial activation from the human heart: One size fits all. *PACE*, 10:21–31, 1987.